CRUST AND UPPER-MANTLE IMAGING BY USING P AND S RECEIVER FUNCTIONS IN DIFFERENT TECTONIC REGIMES

by

Metin Kahraman

B.S. in Geophysical Engineering, Istanbul University, 2004

M.S. in Geophysics, Boğaziçi University, 2008

Submitted to the Kandilli Observatory and
Earthquake Research Institute in partial fulfillment of
the requirements for the degree of
Doctor of Philosophy

Graduate Program in Geophysics

Boğaziçi University

2015

CRUST AND UPPER-MANTLE IMAGING BY USING P AND S RECEIVER FUNCTIONS IN DIFFERENT TECTONIC REGIMES

APPROVED BY:

Prof. Dr. Niyazi Türkelli (Thesis Supervisor)	.....
Assist. Prof. Dr. A. Arda Özacar (METU)	.....
Assist. Prof. Dr. A. Özgün Konca	.....
Assist. Prof. Dr. Çağrı Diner	.....
Assist. Prof. Dr. Tuna Eken (ITU)	.....

DATE OF APPROVAL: 11.12.2015

This thesis dedicated to my huge family.

ACKNOWLEDGEMENTS

I would like to thank Prof. Dr. Niyazi Türkelli for his guidance, enlightening support and useful suggestions during my thesis. It was a unique experience to work and to involve national/international projects with him.

I would like to express my appreciation to Assist. Prof. Dr. A. Arda Özacar from Middle East Technical University for sharing his experience, knowledge, groundbreaking ideas and comments on receiver functions.

I would like to thank to Prof. Dr. Mehmet Ufuk Çağlayan and TAM/TETAM instructors from Computer Engineering, Boğaziçi University to give opportunity work in TAM/TETAM project. This thesis is supported by Turkish State Planning Organization (DPT) under the TAM project, number 2007K120610.

I would like to thank Prof. Dr. Gregory Houseman, Assoc. Prof. Dr. Sebastian Rost from School of Earth and Environment, University of Leeds and Dr. David Graham Cornwell from Department of Geology and Petroleum Geology, School of Geosciences, University of Aberdeen and researcher involved in FaultLab/DANA group for their useful comments and friendship. This thesis is partially supported by Boğaziçi University Research Fund under grant 6922.

I would like to thank Prof. Dr. Eric Sandvol from Department of Geological Sciences, University of Missouri for his instructive comments.

This thesis is partially supported by Boğaziçi University Research Fund (Grant No. 07T203).

Finally, and most importantly, I would like to acknowledge my family and my dear fiancée, Meryem. I would not complete my research without their support, encouragement, quiet patience and tolerance of my pessimistic moods.

ABSTRACT

CRUST AND UPPER-MANTLE IMAGING BY USING P AND S RECEIVER FUNCTIONS IN DIFFERENT TECTONIC REGIMES

P and S receiver functions (RF) are effective tools to solve crustal and upper-mantle velocity contrasts. In this respect, RFs are utilized to image three different tectonic regimes of Anatolia. Firstly, western segment of the North Anatolian Fault Zone (NAFZ) is inspected by data from a dense broadband network (Dense Array for North-Anatolia - DANA) of 71 seismic stations with a nominal station spacing of 7 km in the vicinity of the 1999 Izmit earthquake. High resolved 2-D cross-section images reveal previously unkown small-scale structures and fault geometries in the crust and upper-mantle. Secondly, N-S extension dominated Western Anatolia (WA) is observed by 47 permanent broad-band stations. Totally, 3563 high signals to noise ratio P wave RFs with cut-off frequency of ~1 Hz are obtained among 43146 teleseismic earthquakes. Crustal differences, sharp Moho changes and low velocity zones are defined by 2-D cross-sections in the region. Lastly, Isparta Angle (IA) is imaged by data from a temporary and permanent broad-band seismic network that is composed 42 seismic stations. 4501 P wave RFs are used to resolve upper crustal and Moho depths and 946 S wave RFs are operated to figure out lithospheric-asthenospheric boundary (LAB). Migrated P wave RFs cross-sections present Moho anomalies and African slab in the crust of IA. On the other hand, migrated S wave RFs cross-sections show variation of LAB boundary between ~50 to ~90 km depth range.

ÖZET

FARKLI TEKTONİK REJİMLERDE KABUK VE ÜST-MANTO YAPILARININ P VE S ALICI FONKSİYON YÖNTEMİ İLE GÖRÜNTÜLENMESİ

P ve S alıcı fonksiyonları (AF) kabuk ve üst-manto içerisindeki hız değişimlerini belirlemede kullanılan etkinbir araçtırlar. Bu bağlamda, Anadolu'nun 3 farklı tektonik rejimi AF' lar ile görüntülenmiştir. İlk çalışma bölegemiz, Kuzey Anadolu Fay Zonu' nun (KAFZ) batı kesimi, istasyon aralığı en fazla 7 km olan ve 1999 yılında meydana gelen İzmit depremi civarında konumlandırılan DANA ismindeki geçici seismik ağından toplanan veriler kullanılarak gözlemlenmiştir. Elde edilen yüksek çözünürlüklü profillerde, daha önce saptanamayan küçük ölçekteki süreksizlikler ve KAFZ' nun kabuk ve üst-manto içerisindeki geometrisi saptanmıştır. İkinci çalışma bölgemiz, Kuzey-Güney açılma rejiminin baskın olduğu Batı Anadolu (BA) 47 adet sabit istasyon ile gözlemlenmiştir. 3563 adet yüksek sinyal-gürültü oranına sahip ~1 Hz P dalgası AL' ı 43146 adet telesismik deprem arasından seçilmiştir. Kabuk değişimleri, Moho süreksizliğindeki ani değişimler ve düşük hız zonları iki boyutlu profiller boyunca görüntülenmiştir. Son çalışma bölgemizde Isparta Açısı (IA), toplamda 42 adet geçici ve kalıcı sismik istasyonların oluşturduğu sismik ağ ile görüntülenmiştir. 4501 adet P dalgası AF' ları kabuk ve Moho derinliklerini çözümlemede, 946 adet S dalgası AF' ları litosfer-astenosfer sınırını (LAS) belirlemede kullanılmıştır. P dalgası AF' u migrasyonu ile oluşturulan profiller IA altındaki kabuk içerisinde, Moho değişimlerini ve Afrika dalma-batma zonunu görüntülemiştir. Bununla birlikte, S dalgası AF' u migrasyonu ile LAS' nın ~50 ile ~90 km arası derinlikte değişim gösterdiği saptanmıştır.

TABLE OF CONTENTS

LIST OF FIGURES

LIST OF TABLES

LIST OF SYMBOLS

H	Thickness of the velocity discontinuity
κ	Vp/Vs ratio
p	Ray parameter
Ps	Converted P to S phase
Ppphs	Converted PpPhs phase
PsPhs+PpShs	Converted multiples PsPhs+PpShs phase
PsPhs	Converted multiples PsPhs phase
Vp	P wave velocity
Vs	S wave velocity
Sp	Converted S to P phase
ϕ	Back-azimuth Angle
θ	Incidence Angle

LIST OF ACRONYMS/ABBREVIATIONS

CCP	Common Convesion Point
DANA	Dense Array for Northern Anatolia
LAB	Lithosphere-Asthenosphere Boundary
LVZ	Low Velocity Zone
IA	Isparta Angle
MTRF	Multi Taper Frequency Domain Receiver Function
NA	Neigbourhood Algorithm
P-RFs	P Receiver Functions
RF	Receiver Function
S-RFs	S Receiver Functions
TDRF	Time Domain Receiver Function
WA	Western Anatolia

1. INTRODUCTION

Anatolia which is a part of Alpine-Himalayan orogenic belt, displays complex tectonic evolution. Past geological studies indicate that Anatolia was formed by discrete coalesced pieces of continental lithosphere amalgamated during the closure of the Paleotethys Ocean in the mid-Triassic and Neotethys Ocean in the late Cretaceous/Paleocene to Middle Miocene with suture zones marked by ophiolite sequences and accretionary complexes (Şengör & Yılmaz 1981; Şengör et al. 1985). Present day tectonic regime of Anatolia is mainly controlled by continent-continent collision in the east and ongoing northward subduction of African plate in the west. The collision of Arabian plate along the Bitlis suture (BS) has resulted in slab break-off around Late Miocene time and formation of East Anatolian Plateau. On the other hand, southward retreat and roll-back of subduction along the Aegean arc led to formation of Western Anatolian Extensional Province (WAEP) and a slab tear disconnecting Aegean and Cyprus Arcs (Biryol et al. 2011). The geodynamic forces related to slab pull and continental collision eventually led to westward tectonic escape of Anatolian plate along dextral North Anatolian Fault Zone (NAFZ) and sinistral East Anatolian Fault Zone (EAFZ) (Bozkurt 2001, Fig. 1.1).

The present crustal structure of these distinct tectonic domains holds the key to understand the style of deformation and geodynamic interactions between different tectonic processes. Especially, depth of Moho discontinuity is defined by the crustal thickness, thus effective isostatic forces and its topography / offset give important insight related to the deformation style in the lower crust and depth extent of major tectonic elements. Similarly, lithosphere-asthenosphere boundary (LAB) defines the lithospheric thickness revealing clues related to upper mantle rheology. In this respect receiver functions which are composed of converted phases sensitive to discontinuities rather than absolute seismic velocities, provides a unique opportunity to detect the spatial variations of mid-crustal, Moho and LAB discontinuities and average Vp/Vs ratio and presence of low velocity zones (LVZ) possibly linked to partial melt occurrences.

In this thesis, we imaged crustal and upper mantle structures beneath three different

deformation regimes in Turkey by using P and S receiver functions. The first region which is located along the western segment of the NAFZ, is selected to image deep structure of continental strike-slip fault zone acting as a transform plate boundary since the depth extent of such faults is still under much debate. The second region is located in Western Anatolia Extension Province (WAEP) which is characterized by young volcanism and active graben and horst systems overprinted on the exhumed Menderes metamorphic core complex. Our aim is to image the spatial geometry of crustal discontinuities beneath a core complex to shed light into exhumation mechanism and lower crustal rheology. The last region includes Isparta Angle (IA) which is characterized by relatively high topography and nappe emplacement from multiple directions. This Λ shape lineament separates the WAEP from Central Anatolian Province (CAP) and spatially correlates with the slab tear disconnecting Aegean and Cyprus Arcs. In this region, our main target is to identify crustal and lithospheric thicknesses to evaluate isostacy and reveal the characteristics of Moho and LAB discontinuities to understand possible effects of the slab tear on the style of deformation in the crust and lithosphere.

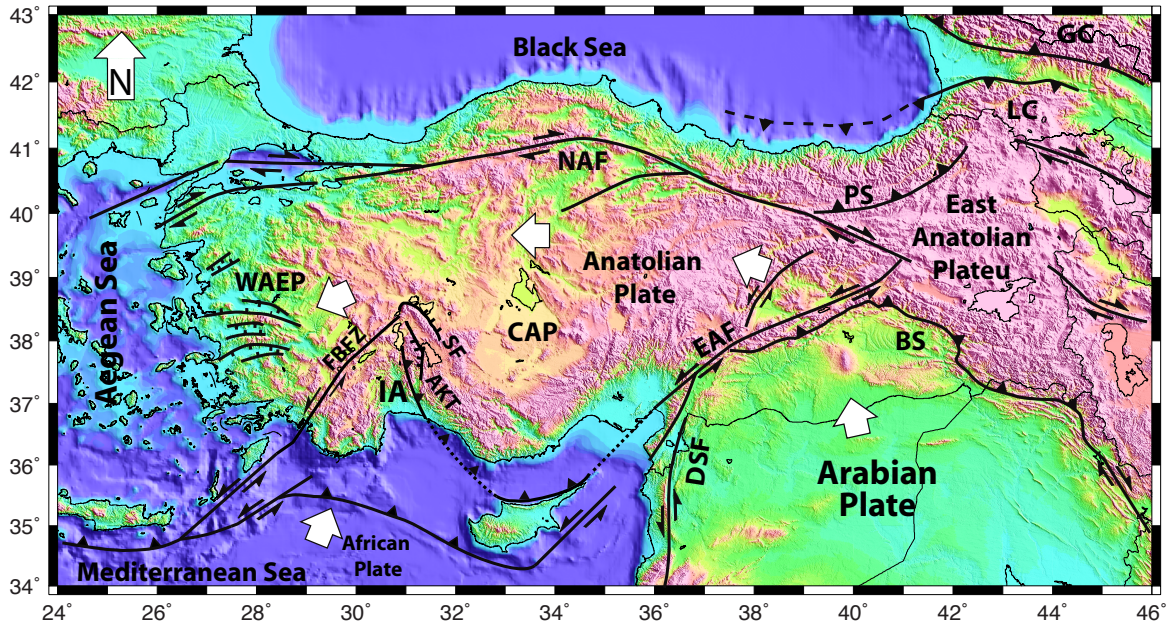

Figure 1.1. Tectonic map of Turkey. Arrows indicate the motion direction of plates and faults. CAP, Central Anatolian Province; IA, Isparta Angle; WAEP, Western Anatolia Extensional Province; AKT, Aksu-Kyrenia Thrust; NAF, North Anatolian Fault; EAF, East Anatolian Fault; DSF, Dead Sea Fault; FBFZ, Fethiye Burdur Fault Zone; SF,

Sultandağ Fault; BS, Bitlis Suture; PS, Pontide Suture; LC, Lesser Caucasus; GC, Greater Caucasus.

In Chapter 2, we present the basic methodology about the P and S receiver function method. The receiver function techniques that are used to calculate crustal thickness, Vp/Vs, crustal velocities and imaging methods are going to be explained detail in this chapter. In Chapter 3, we present the application of P receiver function method and related techniques to strike slip faulting dominated western segment of NAFZ where a dense temporary array (DANA) is deployed. In Chapter 4, we produced discontinuity images of the crust beneath the Menderes Massif located in WAEP using P receiver functions computed from seismic data recorded at permanent stations of national monitoring centers (KOERI and AFAD). In Chapter 5, both P and S receiver function methods are applied to image the entire lithosphere beneath IA which led to reliable crust and lithosphere thickness estimates in the area. In Chapter 6, we have summarized our main results obtained from these different tectonic settings.

2. RECEIVER FUNCTION METHOD

Receiver function (RF) method has been applied widely in the last decades for estimating the partial impulse response of the crust and the upper mantle velocity contrasts. The method has become extensively used due to its less computational time compared to other seismic waveform analysis tools such as a travel-time tomography or geophysical inversion methods. The early studies have introduced phase conversions in teleseismic body waves such as from P-to-S and S-to-P (Phinney, 1964 and Bath and Stefannson 1966). These converted phases were/have been employed to figured out seismic discontinuities beneath a seismic station. Ammon et al., (1991) have introduced the source equalization procedure that can be used to isolate the response of the crust and upper mantle using teleseismic P and S waves.

In a general sense, receiver functions rely on teleseismic earthquakes that sample the Earth along their travel paths. More specifically, teleseismic P and S waveforms are combination of convolved effects of earthquake source, ray path between source to receiver, structure beneath receiver and receiver (seismometer). The response of Earth structure beneath receiver, in other words, RF can be obtained by deconvolution methods that cancel the effects of earthquake source or ray path. RF waveforms involve P-to-S converted phases (Ps and reverberations) and/or S-to-P converted phases (Sp) that are associated with boundaries (Moho and LAB; Lithosphere Asthenosphere Boundary) beneath the recording site.

In the following sub-titles, we introduce first P Receiver Function (P-RFs) and S Receiver Function (S-RFs) method and the techniques of how to obtain them. Lastly, we present methods about modeling P and S RFs to get information about depth, Vp/Vs, Moho topography and crustal and upper mantle velocities.

2.1. P Receiver Function Method

P receiver functions (P-RFs) calculated from three component seismograms that include converted and reverberated phases, help us to reveal the relative response of

Earth's structure beneath the station. The underlying theory is; the steeply incident teleseismic P wave front (Fig. 2.1.a) will be converted to S wave when the incident P wave comes across relatively sharp velocity discontinuities in the crust and upper mantle. The expected arrival of converted P_S and crustal reverberations in horizontally layered medium, $P_P P_S$; P wave front reflected at the surface back to main velocity discontinuity then converted to S phase and arrives as a secondary arrival in RF waveform, $P_P S_S + P_S P_S$; combination of surface converted-reflected back of P wave front to main velocity discontinuity and again surface converted-reflected back of P_S phase to main velocity discontinuity as expected last arrival in RF waveform, show in Fig. (2.1.b) ideal supposed receiver function arrivals.

The relative amplitudes, arrival time, polarity and their frequency contents of the converted and reverberated phases (e.g. Fig. 2.1.b) depend on velocity contrast of layers. The arrival time of Ps phase is sensitive to the velocity, thickness and geometry (dipping or not) of the layer (Ammon et al., 1990), while its amplitude is dependent upon the magnitude of the S-velocity contrast at the boundary; the polarity indicates whether the impedance contrast is negative or positive.

The basic mathematical expression of the P wave RFs can be expressed as the spectral division of radial to vertical component (in other word, water level deconvolution in frequency domain, Langston, 1979). In order to satisfy this definition, synthetic seismograms can possibly be created as following linear filter theory (Lay and Wallace, 1995). In this theory, the components of seismogram can be written as the output from a sequence of linear filters such as on the signal from a seismic source, propagation through earth and recording at the station.

$$D_V(t) = I(t) * S(t) * E_V(t) \tag{2.1}$$

$$D_R(t) = I(t) * S(t) * E_R(t) \tag{2.2}$$

$$D_T(t) = I(t) * S(t) * E_T(t) \tag{2.3}$$

where, $*$; the convolution operator, $D_V(t)$, $D_R(t)$ and $D_T(t)$; vertical, radial and transverse components, $I(t)$; impulse response of the recording instrument, $S(t)$; seismic

source function, $E_V(t), E_R(t)$ and $E_T(t)$; the vertical radial and tangential impulse response of the earth structure, respectively.

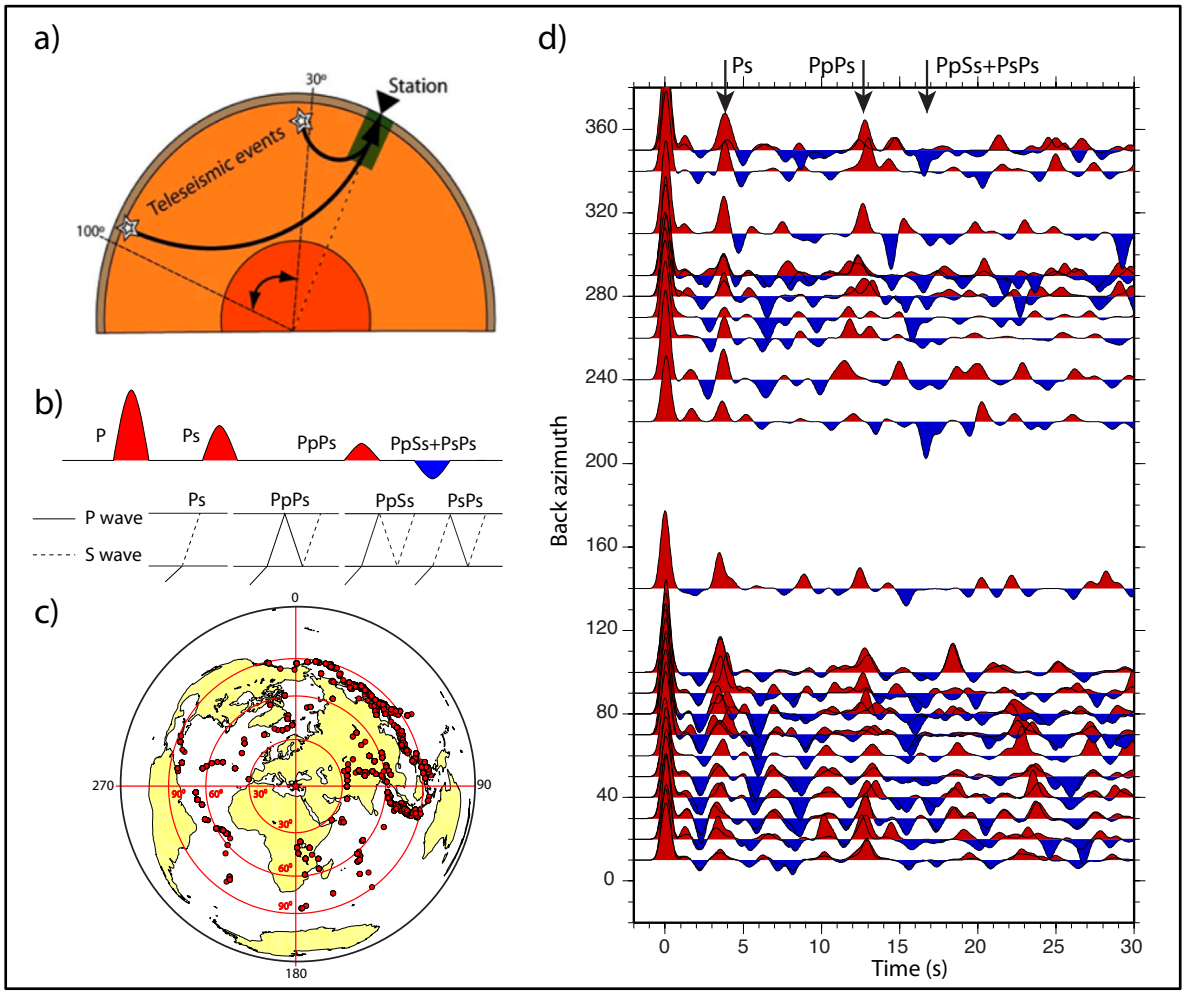

Figure 2.1. a) Travel path of a teleseismic earthquake. b) Ideally expected P-RFs waveform. c) Azimuth distribution of teleseismic events with respect to study center beginning from Jan. 2010 to Jan. 2011. d) Stacked P-RFs with respect to back azimuth value in each 10^0 (modified from Ammon et al., 1991).

An incoming teleseismic P wave at a boundary of contrast velocity layers transfers its energy to horizontal components by conversion at the boundary. The converted energy turns to SV wave on radial and SH wave on transverse components. The amount of converted energy depends on incidence angle of teleseismic P wave and magnitude of velocity contrast between layers. On the other hand, vertical component includes large amount of direct arrivals followed later by only minor arrivals due to crustal reverberations

and phase conversions. So that, the impulse response of vertical component written as a direct delta function in where vertical component defined as,

$$E_V(t) \approx \delta(t) \text{ and } D_V(t) \approx I(t) * S(t) \tag{2.4}$$

and obtained radial and transverse RFs in frequency domain would be,

$$E_R(\omega) = \frac{D_R(\omega)}{I(\omega)S(\omega)} \approx \frac{D_R(\omega)}{D_V(\omega)} \tag{2.5}$$

$$E_T(\omega) = \frac{D_T(\omega)}{I(\omega)S(\omega)} \approx \frac{D_T(\omega)}{D_V(\omega)} \tag{2.6}$$

The data preparation for P-RFs studies starts with the selecting teleseismic events that occur at epicentral distances ranging from 30^o to 95^o as Fig. (2.1.a). In order to reduce the azimuth dependence and obtain a consistent solution, a well azimuthal distribution of teleseismic event locations is needed. An example of ideal azimuthal distribution is given in Fig. (2.1.c). Next, rotation (will be explained following sections) to incoming ray direction is needed to turn Z-NS-EW components to Z-R-T to increase converted phase amplitudes in seismograms. The deconvolution process (will be explained in the following section) can be applied both in time or frequency domains to rotated teleseismic waveforms to obtain radial RFs and transverse RFs. Finally, the elimination of low signal to noise ratio P-RFs are performed by visual comparison of impulsive P arrival on teleseismic components and RFs components. As shown in (Fig. 2.2), a clear arrival of P wave, low noise level on the components of teleseismic events are examined between recorded components. Then, clear Ps and multiple arrivals in radial RFs and lowest energy in transverse components are selected taking into consideration of event's magnitude, distance and back-azimuth values.

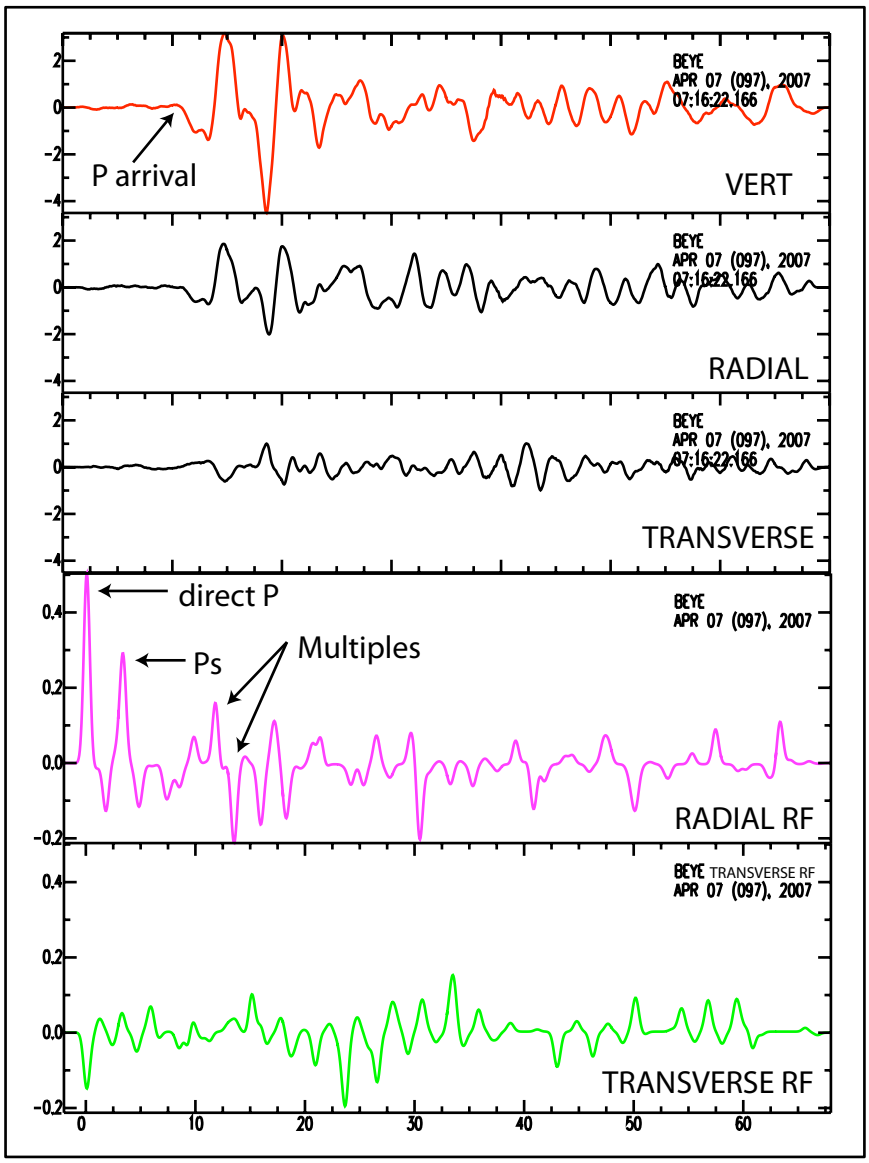

Figure 2.2. An example to comparison between components of a teleseismic event and receiver functions during selection at BEYE (located on Western Anatolia) station.

2.2. S Receiver Function Method

The production of S receiver functions (S-RFs) has a similar procedure to P-RFs method in terms of rotation and deconvolution. However, the main difference in S-RFs is that it utilizes teleseismic S waves and its conversion to S to P rather than teleseismic P wave and its P to S conversion. The basic theory is; teleseismic S phase (e.g. S, SKS or ScS) turns to S to P (Sp) wave on the boundary of a velocity contrast beneath a station (Fig. 2.3.a). The converted Sp phase arrives earlier than the direct S phase (e.g. Faber and

Müller, 1980; Bock, 1991; Farra and Vinnik, 2000; Li et al., 2004 ; Kumar et al., 2005) as shown in Fig (2.3.b).

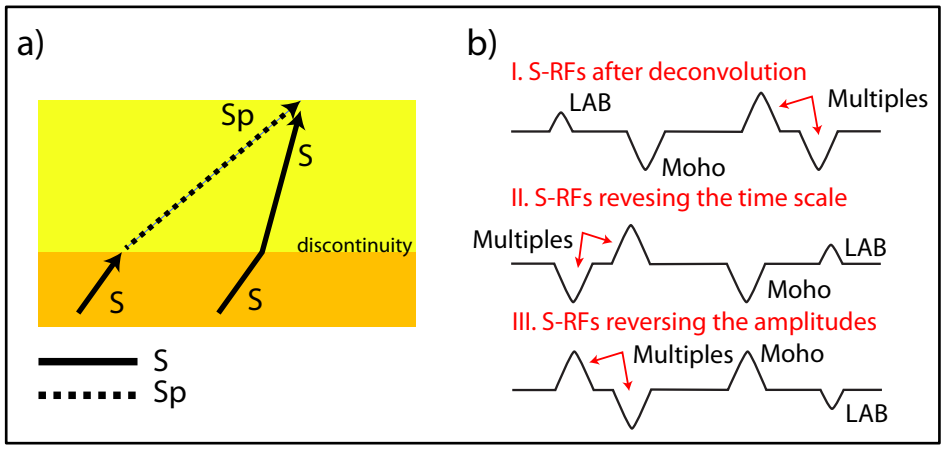

Figure 2.3. a) S receiver function definition. b) Ideally expected arrival phases (modified from Soudodi et al., 2006).

The main advantage of S-RFs with respect to P-RFs technique is; S-to-P converted phase travels faster than incident S wave, thus converted P wave energy preceding incoming S wave field which makes it free from its multiples those arrive shortly after the Sp and S phases. However, the converted Ps and multiple phases recorded after direct P wave arrival in P-RFs. Moho multiples could possibly present large amplitudes that contain significant energy as a reason of sharp velocity contrast and/or deep sedimentary basins in P-RFs waveform. This additional energy could mask arrivals from possible sub-Moho discontinuities such as the lithospheric–asthenospheric boundary (Farra & Vinnik 2000; Wilson & Aster 2005). Although Sp phases are not the first arrivals, even sometimes arrive within the P wave coda, Sp phases do not split along the way to the station in an anisotropic medium, thus the complication of the shear wave birefringence in the P-RFs caused by seismic anisotropy is avoided (Yuan et al., 2006).

Furthermore, S waves are mostly dominated by lower frequencies than P waves since high frequency S wave content affected by the attenuation in upper mantle. Thus, lower frequency content of S waves makes them to proper for studies deeper than the Moho depths such as lithospheric-asthenospheric depths.

Sp converted phases can be obtained by using different type of teleseismic wave fields such as S, SKS or ScS. However, there are certain epicentral distances and depth limitation depending on incoming S wave type since specific ray geometry is needed to observe Sp phases. Weber (1988) and Davis & Handson (1993) examined possible S wave ray paths that is assumed converted at LAB boundary by a Gaussian ray-tracing algorithm (Fig. 2.4.b) using global velocity model (ex. IASP91, Fig. 2.4.a). According to their examination, they stated that useful epicenter distances are 55^{o} to 85^{o} for S waves that converted at mantle discontinuities (Fig. 2.4.c). Sp phase does not exist at distances closer than 55^{o} due to over-critical incidence angle. In addition, S wave is over-lapping with the converted signals from SKS waves away from 85^{o} degree. It is also possible that significant amount of P wave energy created by deep focus earthquakes that occur at 300 – 600 km depth range (pPPP and sPPP) arrive within the same time window with S-to-P converted phase (Wilson et al., 2006).

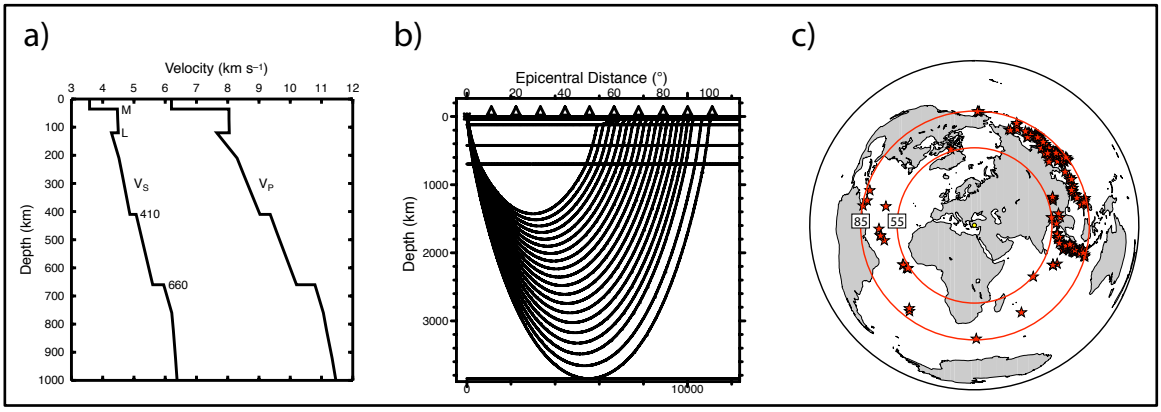

Figure 2.4. a) Global velocity model (IASP91). b) Epicentral distances of converted Sp phase. c) Azimuth distribution of teleseismic events that is going to been utilized in S-RFs study (a and b modified from Yuan et al., 2006).

The calculation of S-RFs begins with the selection of teleseismic events from the database considering the limitations stated above. Figure (2.4.c) shows an example of azimuthal distribution of events that are used in S-RFs study (A detailed process of data selection and proceedings for S-RFs will be explained in section 5.3). Z-NS-EW are rotated to L-Q-T components (will be explained in section 2.3). The rotation to ray based coordinate system is applied to all available teleseismic event waveforms. In order to

satisfy similar analogous between P and S RFs, the time axis of rotated L and Q components are flipped (Fig. 2.3.b phase II.) and amplitude axis is reversed. (Fig. 2.3.b phase III). Then, deconvolution (will be explained in sections 2.4.) of L to Q component is applied in time domain to produce the final S-RFs.

2.3. Rotation

In receiver function analysis, rotation is the first process to be applied to three-component recorded, Z-NS-EW, seismograms in order to enhance converted signal to noise ratio on the components. P RFs studies are mainly focused on components and conversions that would be taken into account in deconvolution process. Therefore, vertical component with mostly dominated P wave energy and horizontal components with radially polarized P to SV and transversally polarized P to SH phase conversions are needed. Since SV and SH conversions are best observed on radial (R) (P-SV) and transverse (T) (P-SH) components, teleseismic events are horizontally rotated around Z axis to incoming ray direction with respect to their back-azimuth value using equation (2.7), showed in Figure (2.5). For all P RFs studies done in this thesis, horizontally rotation of components NS-EW to R-T was applied then deconvolution procedure followed out.

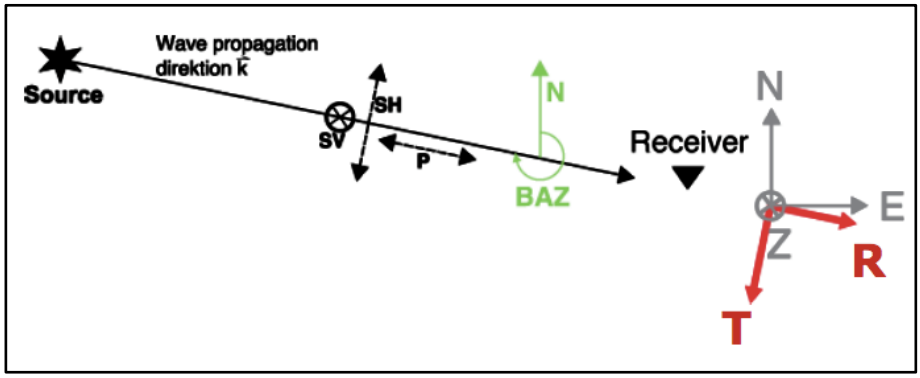

Figure 2.5. Z-NS-EW to Z-R-T rotation.

$$\begin{pmatrix} Z \\ R \\ T \end{pmatrix} = \begin{pmatrix} 1 & 0 & 0 \\ 0 & \cos(\phi) & \sin(\phi) \\ 0 & -\sin(\phi) & \cos(\phi) \end{pmatrix} \begin{pmatrix} Z \\ NS \\ EW \end{pmatrix} \tag{2.7}$$

On the other hand, a further rotation around transverse (T) axis is needed by an incident angle θ to transform the Z-R-T into the local ray coordinate system L-Q-T in S-RFs. This is because of S waves dominated on lower frequencies than P waves so, a better isolation of Sp phase is satisfied by this additional rotation. In this new coordinate system, P wave energy is concentrated on the L component, SV energy on the Q component, and SH energy on the T component Figure (2.6).

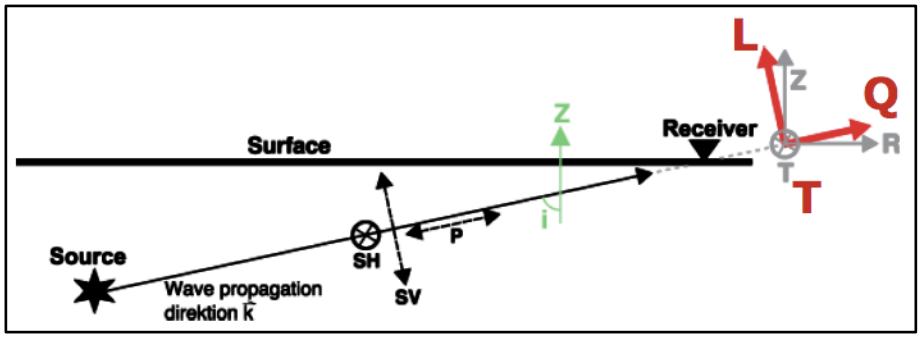

Figure 2.6. Z-R-T to L-Q-T rotation.

The key factor in ray based coordinate rotation is a correct estimation of the incidence angle of arriving S wave. Overestimation or underestimation of the incidence angle can result in some P wave energy on the Q rather than L component, which is shown also in equation (2.8).

$$\begin{pmatrix} L \\ Q \\ T \end{pmatrix} = \begin{pmatrix} \cos(\theta) & -\sin(\theta)\cos(\phi) & -\sin(\theta)\sin(\phi) \\ \sin(\theta) & -\cos(\theta)\cos(\phi) & \cos(\theta)\sin(\phi) \\ 0 & -\sin(\phi) & \cos(\phi) \end{pmatrix} \begin{pmatrix} Z \\ NS \\ EW \end{pmatrix} \tag{2.8}$$

A method proposed by Kennet (1991) was applied to all possible Z-R-T components in order to maximize converted Sp energy on L and SV energy on Q components. The free surface effect is removed from three component seismic recordings to recover the incident up going wave field. Slowness and azimuth of the current wave front must be specified as a function of time to progress the calculation. If the incident wave field is dominated by a single horizontal slowness $p = |\rho\perp|$ and further assuming that near-surface P, S velocities,

α, β are known, an approximate 1-D up going wave field separation can be used to isolate S modes can be written as equation (2.9). In this equation, P,V,H are estimates of the up going P, SV and SH component seismograms; u_r,u_t,u_z are the radial, transverse and vertical displacement seismograms; q_α,q_β,p vertical P, vertical S and horizontal components of slowness at the surface (Bostock, M. G., Treat. on Geophy, Vol1. Section 1.07.3, 2007).

$$\begin{pmatrix} P \\ V \\ H \end{pmatrix} = \begin{pmatrix} \frac{p\beta^2}{\alpha} & 0 & \frac{\beta^2 p^2 - 1/2}{\alpha q_\alpha} \\ \frac{1/2 - \beta^2 p^2}{\beta^2 q_\beta} & 0 & p\beta \\ 0 & 1/2 & 0 \end{pmatrix} \begin{pmatrix} u_r \\ u_t \\ u_z \end{pmatrix} \tag{2.9}$$

Kennet's (1991) free surface correction method can isolate P and SV energy on ray-oriented directions for proper P and S velocities. Before we choose proper surface Vp and Vs for an assumed slowness, we test a range of surface Vp values beginning from 2.5 km/s and gradually increasing 0.1 in each iteration up to 7.5 km/s with respect to corresponding Vs values for constant Vp/Vs = 1.73. The result (Fig. 2.7) indicates that dependency to surface velocity exist but the difference between all possible P and SV components for the tested event are no more than ~%5 or very similar. This result leads us to choose one of the surface velocities of global models where Vp = 6.2 km/s and Vs= 3.58km/s (IASP91).

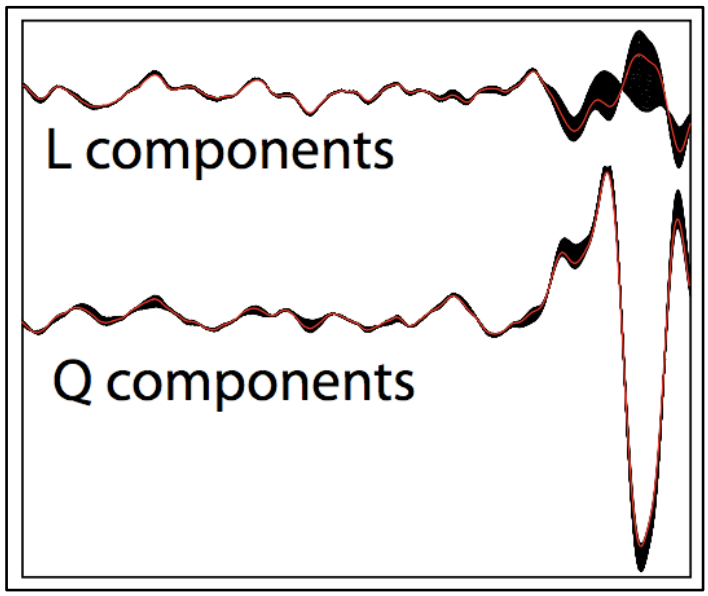

Figure 2.7. Comparison of L and Q components with varying alpha and beta values.

2.4. Deconvolution

The final step to produce the receiver functions is applying deconvolution in order to eliminate the effects of the seismic source, ray path from source to receiver and the recording instrument. The equalization procedure is basically the same for P and S RFs but the difference is to include the proper component and order into the deconvolution. For the P-RFs, vertical component (Z) is deconvolved from horizontal components (R and T) in to obtain Ps and multiples while, horizontal component (Q) is deconvolved from vertical component (L) to reveal Sp phase in S-RFs waveform.

Deconvolution procedure can be done in both time and frequency domains. An iterative approach between vertical and horizontal components is utilized in time domain deconvolution (Liggoria and Ammon, 1999). Frequency domain deconvolution is done by applying extended-time multi-taper frequency domain cross-correlation (Helffrich, 2006).

The basic aspect of iterative time domain approach is; a least square minimization of the difference between the observed horizontal seismogram and a predicted signal, which is generated by the convolution of an iteratively updated spike train with the vertical component seismogram (Liggoria and Ammon, 1999). In order to perform this method,

first, cross-correlation needs to be done between vertical and radial component to estimate the lag of the first and largest spike in the receiver function. Then the result is convolved with the vertical component seismogram and subtracted from radial component seismogram. The result will again be cross-correlated with the vertical component. Therefore, the misfit between the correlated receiver function and radial component will be reduced in each iteration. Iterative approach will continue to estimate other spike lags and amplitudes until the misfit and additional spikes become unimportant (Liggoria and Ammon, 1999).

The idea of multi-taper spectral correlation (MTSC) method is based on distinguishing between "coherent" and "incoherent" scattering in three component records from single events (Park and Levin 2000). This property make MTSC superior to other deconvolution techniques in terms of producing stable, high signal to noise RFs. It should be performed various stacking assumptions such as, stacks of events in defined azimuth range, stack of many events in a singe station or stack of a single events in many stations to produce 'coherent' and elinemate 'incoherent' signals in other time and frequency methods (Gurrola *et al.,* 1995; Searcy *et al.,* 1996; Bostock and Sacchi, 1997; Dueker and Sheehan, 1997; Levin and Park, 1997a).

MTSC estimates uncertainties for frequency domain multi-taper correlated (MTC) RFs (Park and Levin 2000). This allows analysis of RF weight that is estimated from different seismic events by their relative uncertainties, rather than resorting to an un-weighted stack. Thompson (1982) and Park et al., (1987) argued that spectral leakage is best satisfied with the multiple-taper spectrum estimators. Therefore, MTC RFs are resistant to the bias associated with the majority of incoming P waves. The disadvantage of this deconvolution is that only the first 10 s of the RFs contain a usable signal since RFs amplitude decay at longer lags due to short analysis window (about 60 s). The short time window makes multi-taper RFs useless to involve imaging crustal and upper mantle depths via migration (e.g. Dueker and Sheehan, 1997).

Helffrich (2006) modified the multi-taper RF deconvolution method so that it preserves their amplitudes for arbitrarily long times. The modified frequency deconvolution is called Extended-Time Multi-Taper cross-correlated RFs (ETMTRF). The

deconvolution method uses overlap-and-sum technique for estimating stationary signal spectra in long time series (Press et al., 1992). The difference compare to other overlap-and-sum spectral estimations, it mainly preserves phase information. In order to do this, full length RF waveform is windowed by a sequence of short multiple tapers. Then, individual Fourier Transformed (FT) windowed signals are summed into frequency domain representation. So, the summation of each sub-window protects its phase lags.

Helffrich (2006) stated that windowing by three 2.5π prolate tapers with 10 s duration worked well for 20 Hz sampled data. Each taper window individually segments the data. Three different tapered versions of the data are obtained. Next, FT of each tapered data version is calculated and all the three version of FT data is summed. After that, the standard methods for forming multi-taper spectral estimates (Thompson, 1982; Park et al., 1987) lead to a receiver function estimate $H_R(f)$ by calculating the cross-correlation of the radial (R) component with the vertical (Z) component FT. Noise estimation is made by power of pre-arrival Z component for a particular frequency weighting.

$$H_R(f) = \frac{\sum_{k=1}^{K} (Y_Z^{(k)}(f)) * Y_R^{(k)}(f)}{S_0(f) + \sum_{k=1}^{K} (Y_Z^{(k)}(f)) * Y_Z^{(k)}(f)} \tag{2.10}$$

Here $Y_R^{(k)}(f)$ are the *k*th of *K* Slepian-tapered FTs of the R or Z component signal, $S_0(f)$ is the spectrum estimate of the pre-event noise on the vertical component, and $*$ presents complex conjugation. Applying a $\cos^2$ frequency-domain taper implements a high frequency cutoff to the receiver function. Along with the multiple windows, this leads to normalization factors for the spectra that read,

$$\frac{1}{N_{win}} \times \frac{N_{ft}}{N_{fc}} \times \frac{2}{N_{ft}} \tag{2.11}$$

where the first term is multi-window, N_{win} is the number of windows contributing to the sum, N_{ft} is the number of points in the FT and N_{fc} is the number of nonzero points in the

$\cos^2$ taper. Because the overlap is the same in every $Y_{R,Z}^{(k)}(f)$, no explicit correction is needed for it. The result is a RF as long as the original analysis segments.

Both deconvolution techniques, TDRF and ETMTRF, were applied to show effect of different deconvolution methods on the results in Chapter 3. The following Fig. (2.8) presents the comparison of two deconvolution methods on stacked regions of section 3.5 DANA array. The results indicate that both radial and transverse components presented a limited amount of inconsistency mostly on main converted and multiple amplitudes (both radial and transverse) but there is a good agreement in the arrival time of converted and multiple phases. Time and frequency domain deconvolution methods have success to isolate SV energy on radial and SH on transverse components.

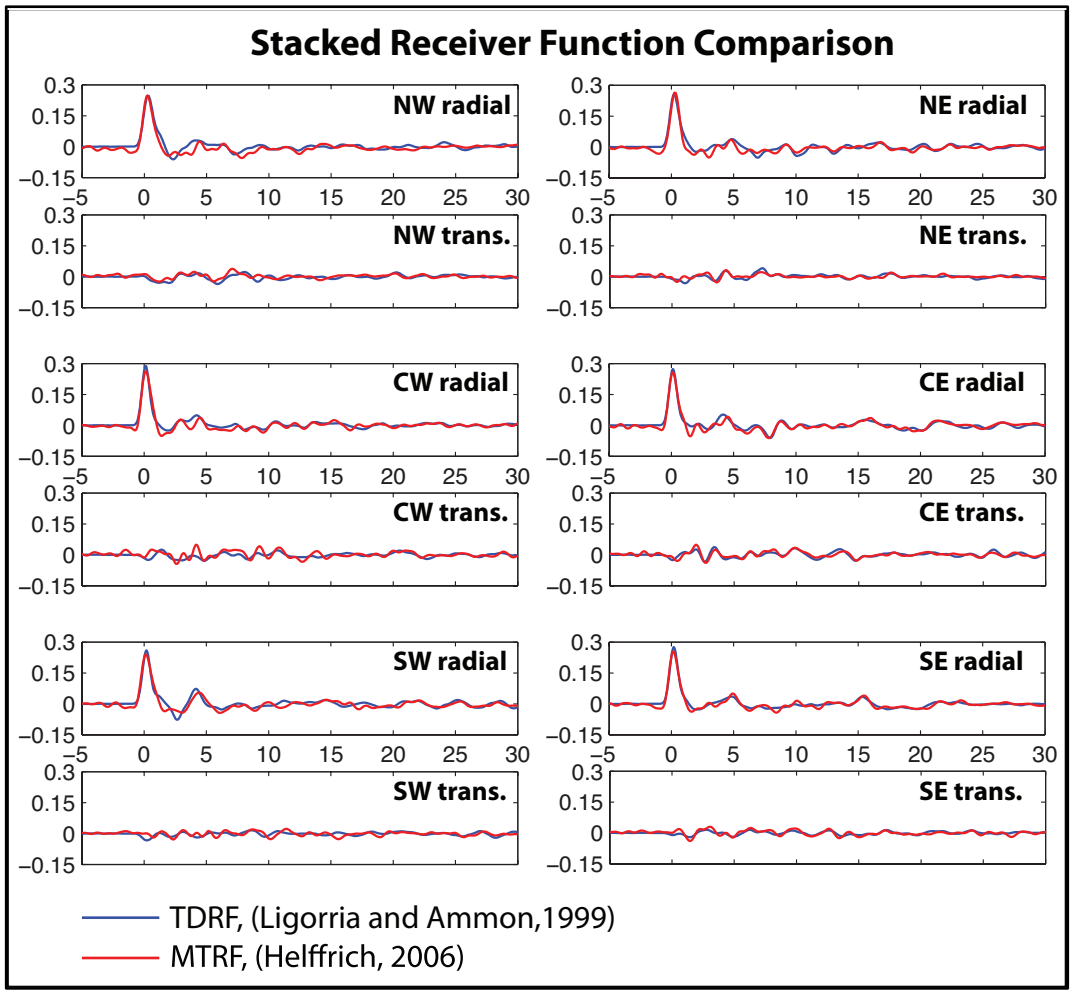

Figure 2.8. TDRF and ETMTRF comparison.

On Fig. (2.8), it was observed that both deconvolution methods work equally well. So, we only choose to apply ETMTRF (in other words MTRF) method in section 3.6. Rest of the receiver function analysis in both P and S ones are completed with TDRF.

2.5. H-K Analysis

The depth of the Moho and corresponding Vp/Vs can be used to characterize the overall structure of a crust and can be often be related to geology and tectonic evaluation of the region. The RFs, especially, P-RFs, are advantageous compared to other methods such as reflection method, since the recorded waves on these active source methods usually travel more than 100 km laterally within the crust. So they became more sensitive to lateral velocity variations rather than the Moho depths.

In order to find an efficient way to calculate crustal thickness, the time separation between direct P and P_S can be used for a given average crustal velocities. In this respect following formula can be used to estimate,

$$H = \frac{t_{Ps}}{\sqrt{\frac{1}{V_S^{\,2}} - p^2} - \sqrt{\frac{1}{V_P^{\,2}} - p^2}} \qquad 2.12$$

in which p is the ray parameter of the incident wave, V_P and V_S are average crustal velocities, H is the thickness of the crust, t_{Ps} is the time separation between P and P_S.

However, calculation of crustal thickness using only the time difference between direct and converted phase would not produce reliable results since there will be significant trade-off between depth and corresponding velocity in $H-\kappa$ domain as shown in Fig (2.9). In order to minimize this fluctuation, depth solutions of crustal multiples are added to $H-\kappa$ domain. The depth related with $P_P P_S$ and $P_P S_S + P_S P_S$ phases can be formulized as,

$$H = \frac{t_{PpPs}}{\sqrt{\frac{1}{V_S^{\,2}} - p^2} + \sqrt{\frac{1}{V_P^{\,2}} - p^2}} \qquad 2.13$$

$$H = \frac{t_{PpSs+PsPs}}{2\sqrt{\frac{1}{V_S^{\,2}} - p^2}} \qquad 2.14$$

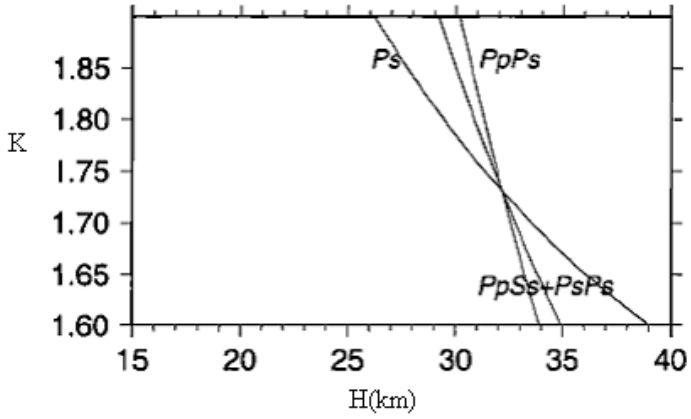

Figure 2.9. Presentation of calculated $H-\kappa$ value at the intersection of converted and multiple phases (modified from Zhu and Kanamori 2000).

It is not generally easy to identify converted P_S phases and other multiples $P_P P_S$ and $P_P S_S + P_S P_S$ due to background noise, scattering from crustal heterogeneities or P to S conversions from other velocity discontinuities. In order to increase signal to noise ratio, stacking multiple events on the time domain is helpful.

Therefore, Zhu and Kanamori, (2000), have developed an $H-\kappa$ stacking technique that sums the amplitudes of receiver functions at the predicted arrival times of P_S, $P_P P_S$ and $P_P S_S + P_S P_S$ for different crustal thicknesses H and κ. This transforms the time domain receiver functions directly into the depth and V_P/V_S domain without the need of identifying converted phases and multiples and to pick their arrival times with assuming a starting average P wave velocity model. $H-\kappa$ stacking can be defined as

$$s(H-\kappa)=\sum_{j} w_1 rf_j(t_1)+w_2 rf_j(t_2)-w_3 rf_j(t_3) \tag{2.15}$$

where H is the thickness κ is the V_P/V_S ratio, $rf_j(t)$ are the receiver functions, with j ranging from 1 to the total numbers of waveforms. t_1 ,t_2 and t_3 are the predicted P_S, $P_P P_S$ and $P_P S_S + P_S P_S$ arrival times corresponding to crustal thickness H and V_P/V_S ratio (κ) as given in the 3.13 – 3.15, w_i are weighting factors and total of them will be equal to one.

$$\sum w_i = 1 \tag{2.16}$$

Among these weighting factors, the highest one (w_1) will belong to the delay time of P_S , since almost 60 – 70 % since P_S is converted from the Moho and it is the most clearly observed receiver function recording. In addition to this, the weighting factor of $P_P P_S$ (w_2) will have 20 – 30 % and the weighting factor of last multiple (w_3) which is $P_P S_S + P_S P_S$ will been affected 0 – 10 % the calculation.

The best estimation of H and κ are found where there phases are stacked coherently. An example is shown in figure 2.9. The different weighting factors were applied the same receiver functions.

An advantage of this of method is that the differential arrival times of converted phases and multiples are less affected by lateral velocity variations since the conversion point of P to S is close to the station. In addition to this, using of differential times in the calculations, crustal P velocity is not as strong as converted S velocity.

On the other hand, the disadvantage of this method is that we assume a planar, homogeneous Moho discontinuity and no lateral variation in our calculations. However, if Moho is dipping, the V_P/V_S will be affected in the basis of longer travel times for multiples traveling up-dip with respect to those generated at a horizontal interface (Ligorria, 2000). Conversely, multiples traveling down-dip will travel shorter distances. This will lead the variation for V_P/V_S and depth. Another disadvantage is that the

presence of gradational Moho discontinuity instead of sharp, well defined Moho discontinuity (Julia, 2004). This condition is the reason of the energy from the boundary interaction phases that spread in time so that the corresponding pulses decrease in amplitude and increase in width (Cassidy, 1992; Liggoria, 2000). In addition to this, $H-\kappa$ stacking method has a difficulty in intra-crustal discontinuities. Converted phases and multiples from intra-crustal discontinuities could interfere with the real Moho Ps converted phase, which will be resulted in time shift of the P_S peak. The variation in P_S time will lead to unrealistic thickness and V_P/V_S ratios.

2.6. Receiver Function Inversion with Neighbourhood Algorithm

Geophysical inverse problems are mainly addressed by using linear inverse theory (Menke 1989; Tarantola 1987; Parker 1994), which involves the calculation of partial derivatives of the data with respect to a single model parameters. This kind of approach leads the geophysical inverse subjects to formulate as an optimization in a finite dimensional model space. In this respect, the geophysical subjects such as seismic velocity, absolute seismic velocities or any kind of physical property of the Earth are identified by a combination of elements that creates model space in inversion process. The inversion algorithm endeavor to produce better fit to observed data until a treshold misfit value reached in each iteration. The efficiency of inverted input model, in other words, how good your proposed model solve the subjected problem is evaluated in terms of data misfit between forward solution of produced data from inversion and observed data.

However, the linear inverse theory is not capable of produce relevant solutions for non-linear problems since the theory does not run independently from initial starting model (Ammon et al., 1990). Other than the dependency to initial model, it is not generally started the solution of non-linear problems by enough elements in the proposed model that does not decrease misfit range as a final result. In addition to this, it is possible begin to process with variety of different starting models that can produce a range of optimal models and fit the observed data. It is still an unknown problem whether there is another starting model that can produce a better data fit or there is a linear relation between starting model and data fit. There is no any sophisticated approach to produce a unique solution except beginning to inversion process a reliable starting model in linear inversion methods.

In order to solve the dependency issue and propose a new approach to produce a unique solution with inversion, derivative-free 'direct search' methods are considered as an alternative way. Derivative-free methods are theoretically described by searching the unique solution among all possible inputs that are defined randomly within the limits of model space. This is different than 'classical' inversion which follows single model input, run and compare data misfit of produced model with real data. Sambridge (1999) suggested a new algorithm that presents an efficient way to use derivative-free method that is called 'Neighbourhood Algorithm (NA)'. NA makes a random sampling in model space and suggests most trustable regions among those sampled areas according to the value of data misfit. Then, another dense sampling is applied to the areas that the low misfit is produced compare to other regions. So, the procedure continues until expected misfit threshold is reached in each re-sampling of trustable regions where the unique solution is finally produced. Sambridge (1999) defines these trustable regions by Voronoi cells in a model space. Voronoi cells are improved and created by taking reference from their neighbourhood Voronoi misfit value in each iteration. The advantage of NA is connected to that previous reference misfit value which leads to behave as guidance to focused areas that unique solution can be figured out from whole model space.

Sambridge (1999) defines NA in four steps;

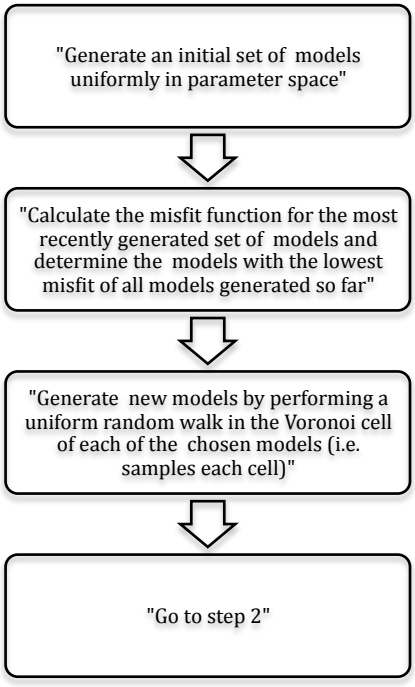

An example of NA is given by Sambridge (1999) and it can be illustrated as Fig. (2.10). Sambridge (1999) defines his model space in 2-D with limited corner values. The NA run and creates 10 random points in the model space and then Voronoi cells are drawn (Fig. 2.10.a, n_s = 10). Next, NA continues to iterate for 10 times and produce 10 new Voronoi cells inside the first produced Voronoi cells. The algorithm begins to decrease perturbing area in model space and focus the regions that produce best models (Fig. 2.10.b, n_s = 100). Lastly, the best Voronoi cells are defined by 10 more iteration combining all promising Voronoi cell in model space (Fig. 2.10.c, n_s = 1000). Black areas in Fig. (2.10.d) are the most promising regions that have potential produce best models in model space.

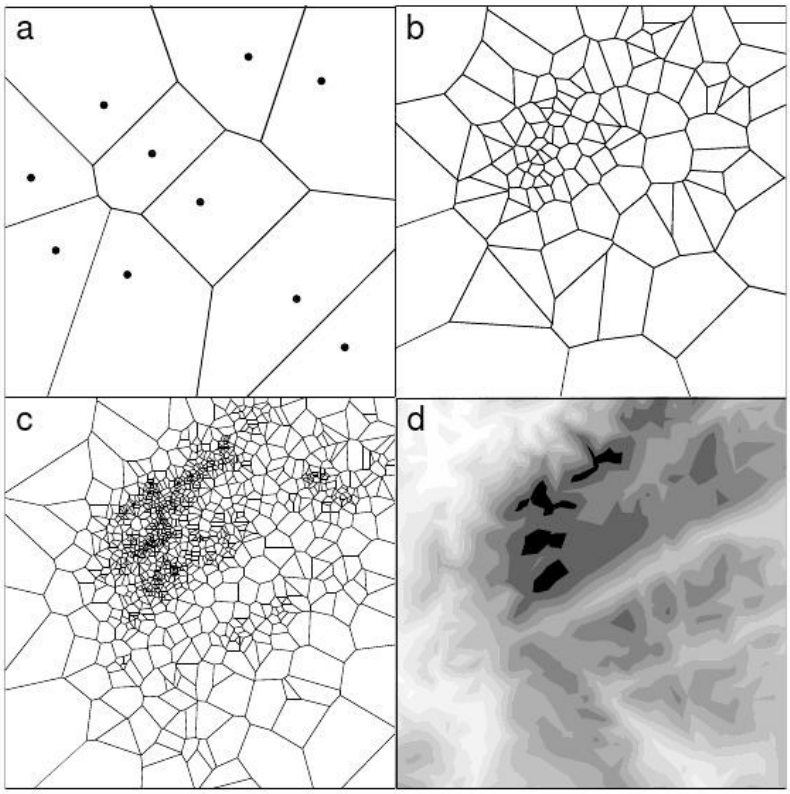

Figure 2.10. Presentation of Voronoi cells in model space with NA (modified from Sambridge 1999a).

The concept of NA and Voronoi cell creation present a logic parameter search in limited model space. The crucial points in this concept are generation of new models inside

of Voronoi cells and decision of Voronoi cell area in model space. The one easy way to determine Voroni cell intersections is suggested by the Sambridge (1999) which is called 'a brute force approach'. According to this method, model space axis can be decomposed into n_a points and the distances of all model samples can be calculated for each of n_a points. The intersections are defined by a line between to closets points in n_a grid that belongs to different Voronoi cells. The drawback of this simple approach is that time consumption to calculate distances between model samples and grid points increase with the number of dimensions and number of models.

Instead of decomposing model space axis, more sophisticated 'refined approach' is proposed by Sambridge (1999). The exact intersection point between two Voronoi cells can be defined by using this approach. The approach suggest that 2-D space is defined and Voronoi cells are created as result of sampled models as in Fig. (2.11), k'th Voronoi cell (v_k) can be defined as being one among all Voronoi cells. The intersection point between k 'th and j'th cells can be determined by x_j which defines a equal distance from both v_k and v_j Voronoi cells as in Fig. (2.11);

$$\left\| v_k - x_j \right\| = \left\| v_j - x_j \right\| \tag{2.17}$$

perpendicular distance in model space in i'th dimension can be written as,

$$d_k^2 + \left(v_{k,i} - x_{j,i} \right) = d_j^2 + \left(v_{j,i} - x_{j,i} \right) \tag{2.18}$$

the perpendicular distance between Voronoi cells, v_k and v_j is defined by d_k^2 and d_j^2 in dimension i. This expression can be solved to find the exact intersection point $x_{i,j}$

$$x_{i,j} = \frac{1}{2}\left[v_{k,i} + v_{j,i} + \frac{\left(d_k^2 - d_j^2 \right)}{\left(v_{k,i} - v_{j,i} \right)} \right] \tag{2.19}$$

The perpendicular distance calculation needs to be done for all Voroni cells that are

located around Voronoi cell v_k.

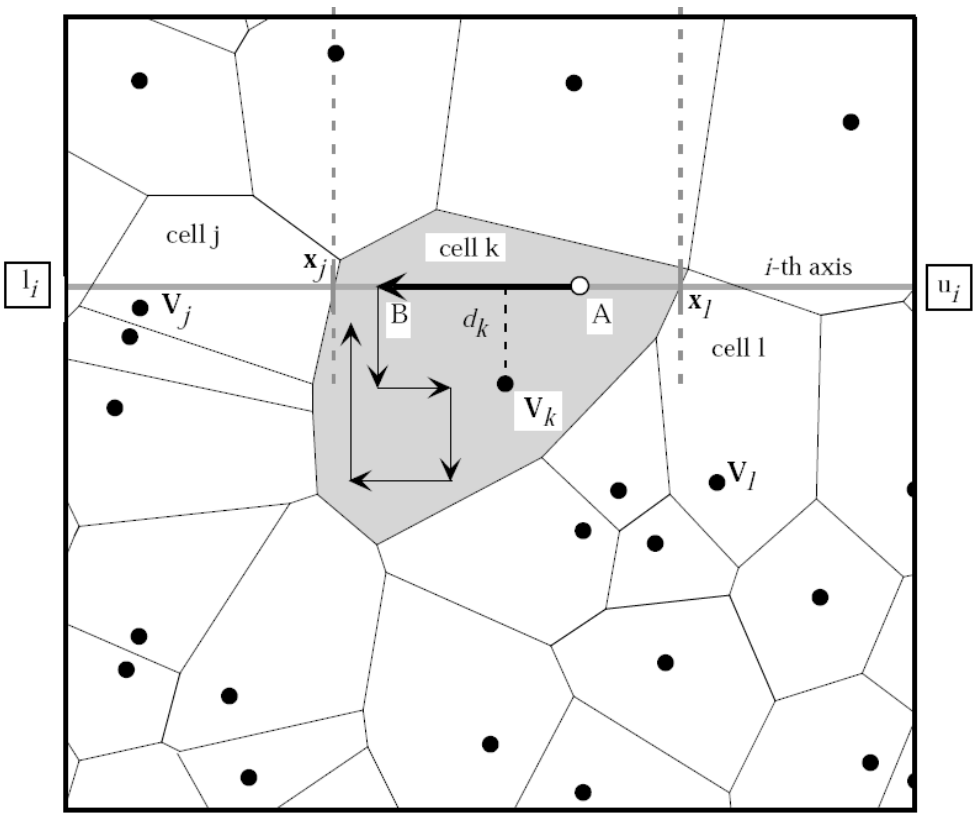

Figure 2.11. Re-sampling of Voronoi cells (modified from Sambridge 1999a).

The refined approach of Sambridge (1999) is faster then the discretized model space axis (the first simple way to determine boundaries of Voronoi cells) since refined approach of Sambridge (1999) does not need to calculate the distance two times for each point of the grid. The time to create each independent sample is then

$$T_{NA} = T_{FM} + \lambda_2 n_p d \tag{2.20}$$

where λ is constant of proportionality, n_p is the amount of models and d is dimensions in model space at the time (Sambridge, 1999).

The overall advantages of NA could be summarized in a two significant properties. The first one is that NA creates automatically input models both in different size and shape by taking reference of previous model misfit. This is superior to single implemented

models into a inversion algorithm since the boundaries of automatically created models are defined with respect to each other. The second one is that the NA uses rank of a misfit function in which created models depend on their relative fit to data. This is useful in seismic waveform inversion since it is easier to answer which model fits better by comparing their ranks. Otherwise, it requires additional statistical methods that need both time and knowledge. So, rank based approach eliminates statistical calculations but rather gives importance to weigh of previous sample during the search for the best-fit model.

2.7. Receiver Function Migration

2.7.1 Common Conversion Point (CCP) Migration

RF stacking is a significant approach to extract energy produced by discontinuities on converted and/or reverberated phase content in final RF waveforms which can be masked by high seismic noise observed on individual RF waveforms as a reason of scattering from surface basins or non-planar interfaces or even undesirable receiver geometries. The stacking can be improved by summing amplitudes of RF waveforms that are obtained from closely spaced stations since RF waveforms are converted from the same common velocity discontinuity and their piercing points are overlapping at subjected velocity contrast such as Moho or LAB. Therefore, phase contents (Ps, Sp and multiple arrivels) from Common Conversion Piercing-Points (CCP) becomes dominant with respect to noise level in RF waveforms.

CCP algorithm consists of two steps, back-projection and stacking. The amplitude of RF is back-projected to the conversion point using a background 1-D velocity model assuming the amplitude of RF arrivals are generated by single P to S conversion along ray path. The location and distribution of piercing point depths are revealed as the result of back-projection. Piercing points of RFs are geographically binned at the conversion depth. All amplitudes in the same bin are stacked and scaled to produce a structural image. The amplitude variance between bins present the velocity contrasts and/or velocity discontinuities in subjected crustal volume (Zhu et al., 2006).

Ideally, the horizontal resolution of CCP image can be defined by piercing point

distance between incoming arrivals from opposite directions for instance teleseismic arrivals from east and west directions. So, combining all piercing points from all directions defines a zone on the surface of subjected velocity discontinuity. This zone is called Fresnel zone and its width on the surface of velocity discontinuity is related to the depth of the velocity contrast (z) and the wavelength of teleseismic wave (λ), which can be formulated as $\sqrt{\lambda z}$ (Zhu et al., 2006). Fresnel zone width varies from few kilometers to ~10 km for upper crust and Moho, respectively, for ~1 RFs (Zhu et al., 2006). On the other hand, P and V_p/V_s perturbations in the crust affect the vertical resolution of CCP image. Zhu et al., (2006) calculated a 3% perturbations in P and V_p/V_s may create ~1 to ~2 km depth difference in CCP image.

In order to produce reliable CCP profiles, lateral heterogeneity and move out corrections should be carried out on stacked CCP profiles since 1-D reference model does not include any velocity changes adjacent regions and timing of Ps or Sp arrival time may create difference depending on source and receiver types. Dueker and Sheehan (1997 and 1998) implemented 3-D tomographic velocity results in their calculations to account for lateral heterogeneity differences. In this thesis, interpolated V_P/V_S values are defined corresponding bins in the study areas. So, more reliable V_S is obtained by variable V_P/V_S and constant V_P for each bin cell to handle lateral heterogeneities.

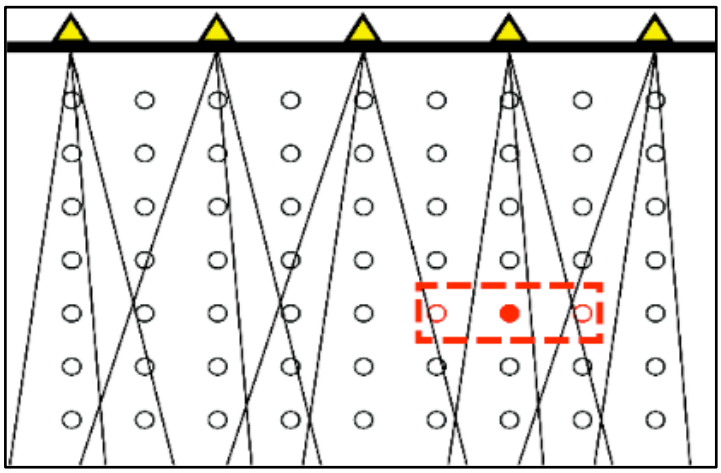

Figure 2.12. CCP migration sketch.

On the other hand, the move out corrections can be predicted accurately by assuming a one dimensional reference model $V_S(z)$ and a constant velocity ratio $R_V = V_P/V_S$.

Gurrola et al., (1994) suggest the converted S wave time at a depth D relative to P wave arrival for a given $V_S(z)$ and $R_V = V_P/V_S$ in a flat Earth,

$$\Delta T_{PS}\left(D,V_S(z),R_V\right) = \int_D^0 \frac{1}{V_S(z)} - \frac{1}{R_V V_S(z)}\,dz \tag{2.21}$$

Generalizing the above normal incidence equation to an arbitrary incoming P wave angel of incidence produces (Gurrola et al., 1994),

$$\Delta T_{PS}\left(p,V_s(z),R_V\right) = \int_D^0 \sqrt{1 - p^2 V_s^{\,2}(z)} - \sqrt{R_V^{-2} - p^2 V_s^{\,2}(z)}\,dz \tag{2.22}$$

where p is the ray parameter of the direct P wave. The results indicate that even considerable velocity change of layers in velocity model creates less than 1 s time difference in move-out curve. This implies that move-out curves almost independent from velocity models. In addition to this, the difference between real and assumed ray parameter of teleseismic wave from 60^o distance and at 660 km discontinuity is only 0.001 s/km. However, magnitude of move-out corrections has dependency both the depth to an interface and the ray parameter of the incoming wave. These can create strong time difference effect on converted phases.

2.7.2. Kirchhoff Migration

Kirchhoff migration is defined in reflection seismology as a removing effects that are sourced from dipping layers and moving the dipping layers to their true locations in the subsurface. In order to that, minimizaton of diffractions that are created from adjacent reflectors and incoming ray paths should be removed. So that, subsurface features such as fault planes or velocity contrasts can be clearly imaged (Yılmaz, 1987).

Other than the reflection seismology, a similar approach can be used to migrate RFs

but this time both direct (P or S) or converted (Ps or Sp) and reverberated multiple phases are moved to their true subsurface position to produce images of the velocity discontinuity structure of subjected Earth volume via teleseismic earhtquakes. In this section, RF are migrated in Kirchhoff style which is stated by Wilson and Aster (2005). Kirchhoff migration defines grid points in a subjected Earth volume and each of those points behave like secondary source due to scattering of incident teleseismic wave at those defined points (Yılmaz, 1987; Dellinger et al., 2000). Ray tracing is used to back-project to each individual RFs to their possible scatters. This calculation are done for each individual RFs and station pairs. In order to image location of scatters, Yılmaz's (1987) Kirchhoff integral is operated to sum and scale the amplitude of RFs from the modeled grid of possible scatter points. The Kirchhoff integral can be written as follow (Wilson and Aster 2005),

$$u_{out}(x,z) = \frac{1}{2\pi} \int S_{tr} \frac{\cos\theta}{vr} \frac{\partial}{\partial t} u_{in}\left(x_{in}, z=0, t\right) dx \tag{2.23}$$

where, v is the rms velocity at the imaging point (x,z), r is the distance between the input $(x_{in}, z=0)$ and the output (x,z) imaging points, and t is the sum of source to imaging and imaging to receiver point. S_{tr} is a scaling factor. $\cos\theta$ is an obliquity factor sourced from recording geometry. The dependence on $\frac{1}{vr}$ is the spherical spreading term and time derivative gives the phase shift required by Huygens' principle.

However, Kirchhoff migration integral can produce artifacts during the process of RF back projection due to randomly distributed points in model space or irregular distribution velocity discontinuities. In order to eliminate these artifacts, regularization needs to be done for produced migrated data that presents subsurface velocity structure (Duquet et al., 2000; Nemeth et al., 1999). So, Kirchhoff style migrated data can be presented by linear operator G and subjected discontinuity is m and recorded data is d,

$$d = Gm \tag{2.24}$$

equation (2.24) can be solved for subjected velocity discontinuity, m, (Nemeth et al., 1999),

$$m = G^T d \tag{2.25}$$

equation (2.25) needs to be regularized to have high resolved subsurface images,

$$m = G^{-g} d \tag{2.26}$$

Kirchhoff style migration is defined as an inverse problem in equation (2.26). So, minimizing of artifacts can be done by minimizing the objective function,

$$\mathrm{P}(m) = \|Gm - d\|^2 + a\|Cm\|^2 \tag{2.27}$$

in equation (2.27), $P(m)$ presents data misfit function, $\|Gm - d\|^2$ stands for the regularization term, C is the matrix used to minimize desired model properties and a is a weights constant for regularization.

The overall, regularization can be defined as smoothing factor that provides an ideal fit between migrated data and magnitude of smoothing. According to regularization, dense sampled areas experience less smoothing while the areas sampled by less data have high smoothing magnitude to provide possible observable regions in the migrated Earth volume.

3. CRUSTAL-SCALE SHEAR ZONES AND HETEROGENEOUS STRUCTURE BENEATH THE NORTH ANATOLIAN FAULT ZONE, TURKEY, REVEALED BY A HIGH-DENSITY SEISMOMETER (DANA) ARRAY

3.1. Introduction

Major continental strike-slip faults, such as the North Anatolian fault Zone (NAFZ) in Turkey or the San Andreas Fault in the USA, are key elements in our understanding of plate tectonics. Such faults are clearly defined at the surface but considerable uncertainty surrounds their structure in the mid to lower crust and upper mantle, and specifically how deformation is focused in shear zones that are presumed to extend beneath seismically active fault planes (e.g., Handy et al., 2007; Platt and Behr, 2011). An understanding of such fault systems (e.g., Pollitz et al., 2001) requires characterisation of the structure and physical properties of the crust and upper mantle to constrain the rheological parameters that determine how stress is redistributed during the earthquake cycle (e.g., Hearn et al., 2009). Localized zones of relatively high or low viscosity can have an important impact on this cycle (Yamasaki et al., 2014).

A detailed characterisation of the 3-D geological structure of a large continental strike-slip fault zone is therefore necessary to show the key structures that have evolved during the active period of the fault and how they will behave during future earthquake cycles. Modeling of geodetic deformation has provided some constraints on the physical variation of creep parameters (e.g., Bürgmann and Dresen, 2008; Hearn et al., 2009; Kenner and Segall, 2003; Wright et al., 2013), however, seismic imaging is the only method that can provide direct insights into the structure of the crust and the variation of elastic properties within it, albeit at length scales that are limited by the seismic wavelength. For instance, variations in Moho topography have been used to argue for both diffuse deformation within the crust (Wilson et al. 2004) and focused fault structure in the upper mantle (e.g., Wittlinger et al., 2004). Such arguments require careful control on the velocity variation within the entire crustal section (Schulte-Pelkum and Ben-Zion, 2012).

In this study, we use teleseismic receiver functions (RFs) to characterise crust and upper mantle structure across part of the NAFZ using seismological data recorded by a rectangular array with a station interval of ~7 km that was deployed for 18 months. The NAFZ is a 1500 km-long right-lateral transform fault that separates a westward moving Anatolia from a relatively stationary Eurasian plate (Fig. 3.1.). Subduction along the Hellenic trench and collision of the Arabian and Eurasian plates results in a general westward movement of Anatolia at rates of 20-30 mm/yr relative to Eurasia (e.g. Barka, 1992; Barka, 1996; McClusky et al., 2000; Reilinger et al., 2006), with strain focused on the NAFZ. Numerous major earthquakes have occurred during the last century (e.g. Barka, 1999); most recently in 1999 with epicentres at Izmit and Düzce (e.g. Barka et al., 2002; Fig. 1). We installed a dense seismic network (DANA - Dense Array for Northern Anatolia) of temporary seismic stations across the NAFZ in the region of the 1999 Izmit rupture in order to create images of NAFZ crustal structure with exceptional horizontal.

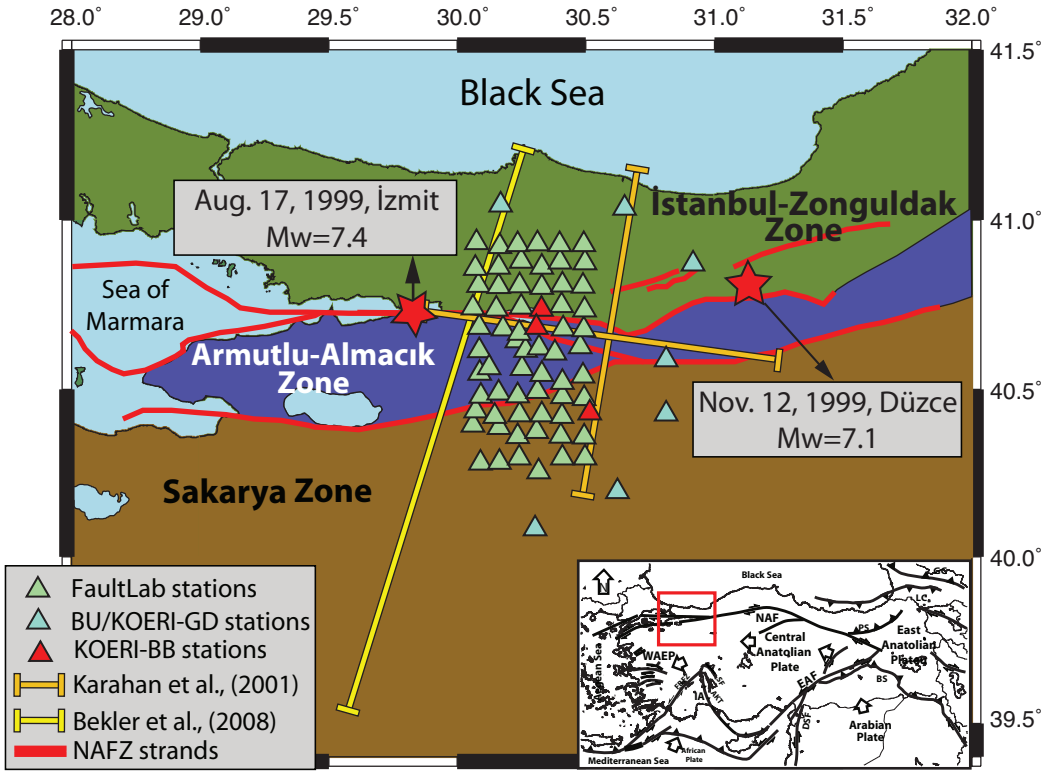

Figure 3.1. Locations of seismological stations for the DANA array (green triangles) and previous seismic refraction experiments (as indicated in the legend), segments of the North Anatolian Fault zone (red) and major tectonic terranes (IZ: Istanbul-Zonguldak zone; AA:

Almatlu-Almacik zone; and SZ: Sakarya zone). The inset map shows the regional tectonic setting.

3.2. Geological Overview

The western NAFZ bisects a complex assembly of heterogeneous zones of differing crustal affinity, namely the continental fragments of the Istanbul-Zonguldak Zone (IZ) and the Sakarya Zone (SZ) (Fig. 3.1.) that form part of what is commonly referred to as the Pontides (e.g. Okay and Tüysüz, 1999). The IZ has a late Precambrian crystalline basement (Chen *et al.*, 2002; Yiğitbaş *et al.*, 2004; Ustaömer *et al.*, 2005) that is unconformably overlain by a continuous Ordovician-Carboniferous sedimentary succession (Görür *et al*., 1997; Dean *et al.*, 2000). Carboniferous convergent deformation was followed by a Triassic marine transgression as the IZ formed part of the Laurasia passive continental margin (Okay, 2008) before Late Cretaceous back-arc spreading created the western Black Sea basin by rifting the present-day IZ southwards (Okay et al., 1994). The Intra-Pontide Ocean gradually closed by north-dipping subduction during Late Cretaceous-Early Eocene times (Okay and Tüysüz, 1999) and the present-day boundary between the IZ and SZ is marked by the Intra-Pontide suture, a 400 km long east-west trending collisional suture that is now reactivated as the present-day trace of the NAFZ (e.g. Okay and Tüysüz, 1999; Sengor and Yilmaz, 1981; Okay, 2008). To the south, the basement of the SZ continental fragment consists of widespread subduction-accretion complexes of Triassic age (Şengor and Yilmaz, 1981; Okay and Tüysüz, 1999). A Jurassic-Eocene sequence of clastic sedimentary, carbonate and volcanic rocks unconformably rests upon the high-grade metamorphic basement (Okay *et al*., 1996; Pickett and Robinson, 1996; Okay and Tüysüz, 1999).

West of about 30.65°E, the NAFZ splits into northern (NNAF) and southern (SNAF) strands with ~16 and ~9 mm/yr slip, respectively (e.g. Stein *et al.*, 1997). The Armutlu-Almacik crustal block (AA) lies between the NAFZ strands and is comprised of SZ pre-Jurassic basement (typically Triassic subduction/accretion units), SZ Jurassic-Eocene sedimentary sequences, a Cretaceous-Palaeocene accretionary complex and metamorphic rocks of unknown age and origin (possibly IZ; Sengor and Yilmaz, 1981; Okay and Tüysüz, 1999; Okay, 2008). The Sakarya River, offset in a right-lateral sense by the

NAFZ, has incised the SZ and AA and has played a prominent role in erosion and deposition of sub-aerial clastic sediments that fill Neogene-Quaternary pull-apart basins near Adapazarı and Düzce (Barka and Gülen, 1988).

The complex accretion history that predates the development of the NAFZ leads us to expect a complex crustal structure in this region, but identifying contrasts in structure from one crustal block to another may reveal the cumulative impact of fault displacements and distributed shear across the fault zone.

3.3. Previous Geophysical Studies

Previous RF studies (Zor et al., 2006; Vanacore et al., 2013) east of the Marmara Sea (Fig. 3.1.) determined crustal thickness in the study region to increase from west (29-32 km) to east (34-35 km), with an average crustal V_P/V_S of ~1.75 (Vanacore et al., 2013). Two seismic refraction experiments that spanned the NAFZ (Fig. 3.1.) reported similar crustal thicknesses of 32±2 km in the west (Bekler et al., 2008) and ~38 km (Karahan, et al., 2001) in the east of our study region, both sampling the AA, SZ and IZ blocks. Bekler et al. (2008) interpreted an upper crustal layer (V_P=5.6-6.1 km/s) extending to ~5 km and lower crustal velocities of V_P=6.7-7.2 km/s, above a low velocity (V_P=7.6 km/s) upper mantle on the western line. On the eastern line, Karahan et al. (2001) found similar crustal velocities (though the upper layer extends to ~12 km depth) and mantle velocities of ~8.1 km/s. These investigations also identified possible crustal seismic discontinuities at depths of ~17 km and ~24 km.

The crust of the IZ and AA appears to have relatively high velocity and low attenuation based on local earthquake tomography (Koulakov et al., 2010). Further along the NAFZ to the east (at 35°E, 41°N), local earthquake tomography detected high-velocities (V_P=6.2-6.5 km/s at depths of 10 to 20 km) and large lateral variations in V_P/V_S ratios (1.72-1.80) in the mid-crust which are thought to be representative of varying lithology and fluid content in the basement (Yolsal-Çevikbilen et al., 2012).

Body wave tomography based upon simultaneous full waveform inversion of

regional and teleseismic waves (Fichtner et al., 2013) and surface waves (Salaün et al., 2012) shows relatively fast velocities (δV_P=+2-3 %; δV_S=+3-4 %) within the IZ lithosphere to depths of at least 60 km (Fichtner et al., 2013) and possibly to 100-150 km. These high velocities appear to abruptly terminate at the surface location of the southern branch of the NAFZ (Berk Biryol et al., 2011). Relatively slow upper mantle velocities (δV_S=-3-4 %) underlie the SZ to the south of the NAFZ and a shallow asthenosphere is thought to cause a broad region of low ($\delta V_S \leq$-2 % or V_S<4.2 km/s) velocity beneath almost the full length of the NAFZ deeper than 80-100 km (Salaün et al., 2012; Fichtner et al., 2013).

Magnetotelluric (MT) data also show first order differences in the conductivity structure of the crust from south to north across the NAFZ (Tank et al., 2005). A highly resistive (>1000 Ωm) crustal basement in the IZ to the north and a moderately resistive crustal basement (>500 Ωm) in the SZ to the south flank a conductive (30-50 Ωm) region within the AA block that extends between depths of ~10 km to ~50 km, apparently into the upper mantle. This lower crustal conductive zone is interpreted as resulting from fluids created by metamorphic dehydration and/or partial melt in the upper mantle beneath the NAFZ (Tank et al., 2005).

3.4. Receiver Function Data and Calculation

The Dense Array for North Anatolia (DANA; Fig. 3.1.), with a nominal inter-station spacing of 7 km and covering a region of 70 by 35 km along 6 north-south lines and 11 east-west lines (Fig 3.1.), was operational from May 2012 until October 2013. An additional 7 stations formed a semi-circle of radius ~60 km around the rectangular array on its eastern side (Fig. 3.1.). Three permanent stations of Boğaziçi University - Kandilli Observatory and Earthquake Research Institute/National Earthquake Monitoring Center (BU-KOERI/NEMC) contributed to the rectangular array. Using data recorded by DANA, we computed RFs from records of teleseismic earthquakes identified from the National Earthquake Information Center (NEIC) catalogue, with m_b>5.5, angular distances of 30° to 90° (Fig. 3.2.a). RFs with maximum frequency of 1.2 Hz were estimated using two different techniques for comparison and since the subsequent analysis methods we

employed required different input RF types: time domain iterative deconvolution (Ligorria and Ammon, 1999) (TDRFs) and extended-time multi-taper frequency domain cross-correlation (Helffrich, 2006) (MTRFs). The former technique was used for *H-κ* stacking and depth migration analyses, whereas the latter was preferred for the RF inversion. A 2-way 2-pole high pass filter was applied to all RFs to suppress noise with frequencies less than 0.1 Hz. Calculated RFs were visually inspected and accepted if there is an absence of pre-signal noise (MTRFs only) on the radial and transverse RF, transverse RFs show less (or comparable) amplitudes than radial RFs, the direct P-arrival is visible and close to predicted arrival time and there is no evidence of large amplitude oscillatory noise (i.e. "ringing") throughout each RF. This resulted in post quality control TDRF and MTRF datasets consisting of 1363 and 2479 earthquake-station pairs, respectively. Figure (3.2.) shows event locations, station stacks for all events used during RF analyses and RF stacks for the 6 array sub-sections defined in Figure (3.3). The majority of recorded events occurred in an arc from north to east of the DANA array and few events sample the remainder of back-azimuthal directions (Fig. 3.2.a). Such an event distribution limits the application of the dataset to RF azimuthal (i.e. anisotropic or dipping layer) studies and instead, we focus our study on defining the complexity in the isotropic crustal structure in this region.

The dense station spacing and event distribution provides excellent sampling of the crustal structure (Fig. 3.3.). RF piercing point locations at a depth of 35 km were calculated using the IASP91 Earth model (Kennett and Engdahl, 1991) and RF stacks (Fig. 3.2.c) were created by binning RFs by piercing point (Fig. 3.3.), correcting for time moveout (to an angular distance of 65° using IASP91) and linearly stacking in six sub-regions. The sub-regions were chosen to examine first order variations in the crust defined by where the NAFZ dissects the three main crustal terranes: SW and SE stacks sample SZ crust to the south of the southern NAFZ branch; CW and CE stacks sample the central AA block defined by the NAFZ branches; and NW and NE stacks sample IZ crust north of the northern NAFZ branch.

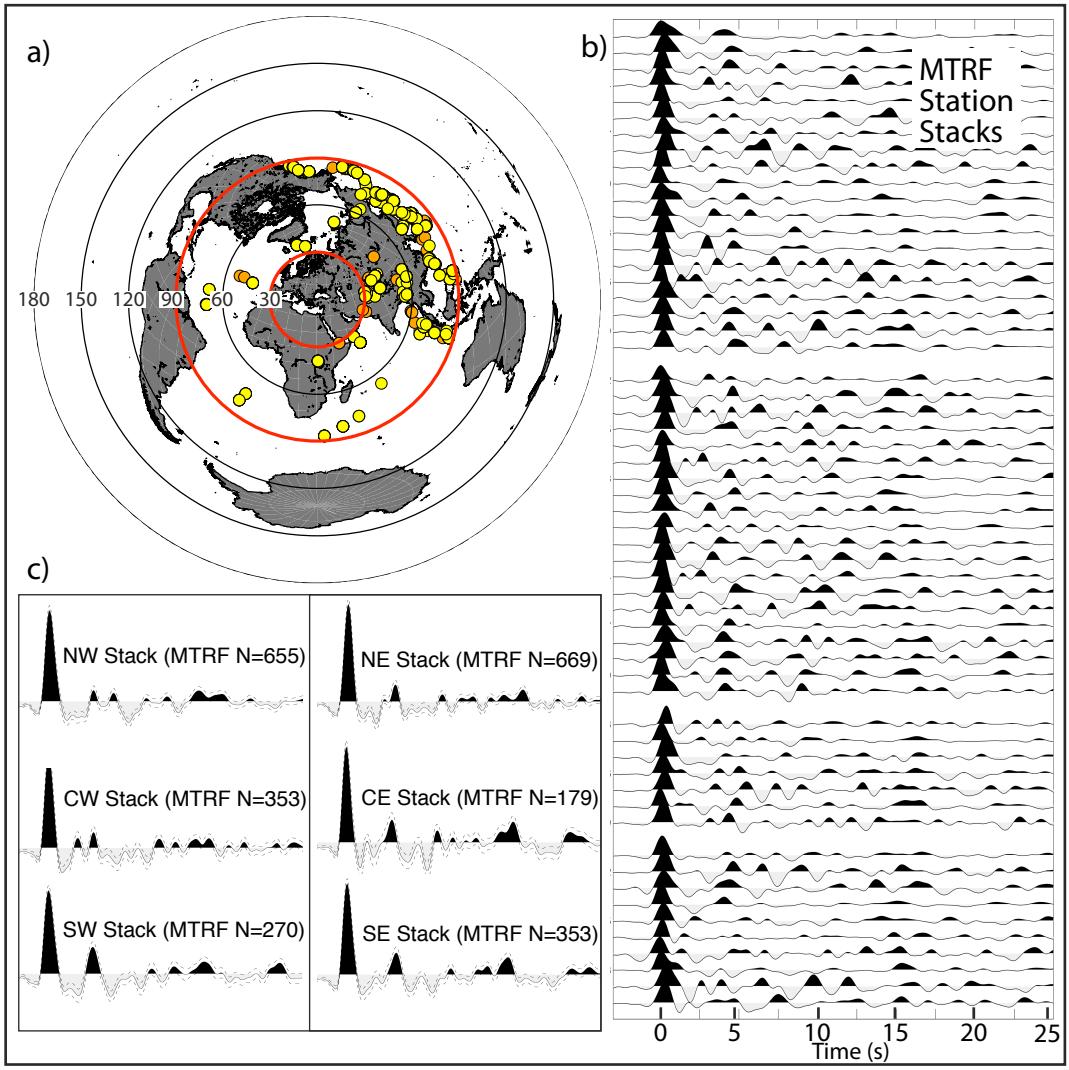

Figure 3.2. Earthquake locations and representative receiver function stacks. a) Locations of mb>5.5 earthquakes occurring during the deployment of the Dense Array for Northern Anatolia (DANA). Earthquakes situated within the red annulus that marks an epicentral distance range of 30-90° were used for receiver function estimation. Yellow and orange circles denote events recorded by the temporary DANA network and permanent stations since 2009, respectively. b) Selected extended multi-taper receiver functions (MTRF) stacked by station for the DANA seismological network. c) Regional MTRF stacks for the six groups of receivers identified in Figure 3 selected receiver functions.

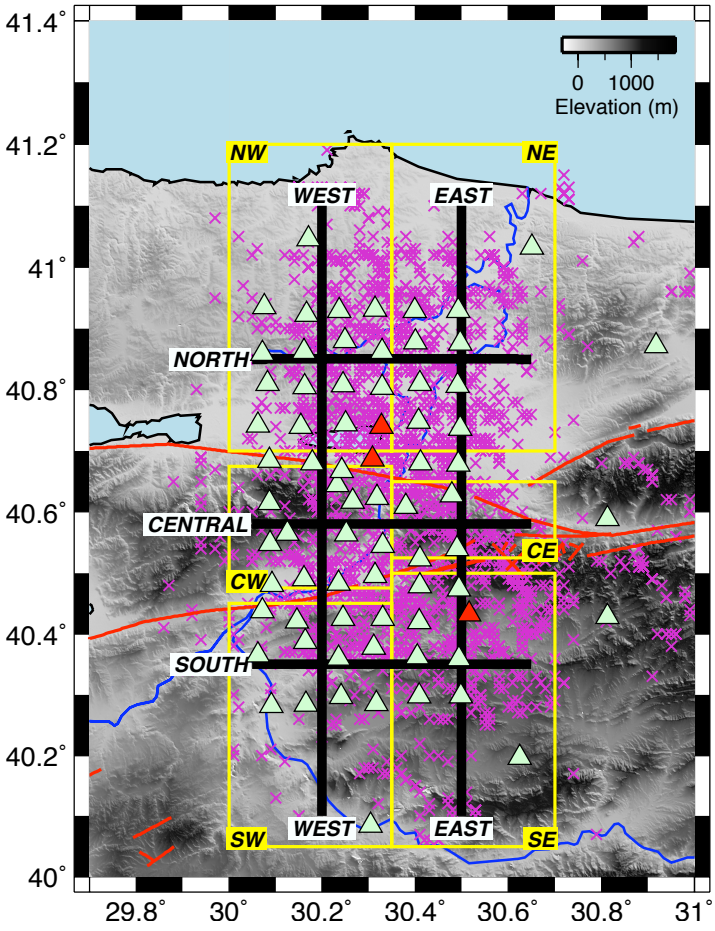

Figure 3.3. Topographical map of the study region with calculated piercing point locations of P-S receiver function conversions at 35 km depth (using the IASP91 Earth velocity model of Kennett and Engdahl (1991)) using selected receiver functions (purple crosses). The major surface north Anatolian fault (NAF) traces are marked in red with the Black Sea in the north and Sea of Marmara to the west (shaded light blue). Labelled yellow rectangles denote the six regions used to construct receiver function stacks shown in Figure (3.2) and labelled thick black lines show the locations of migrated receiver function profiles shown in Figure (3.6).

3.5. H-κ Stacking Method and Results

H-κ stacking (Zhu and Kanamori, 2000) was performed using stacks of between 97 and 285 TDRFs with frequencies of up to 1.2 Hz from each of the six regions outlined in Figure 3. The technique produces estimates of crustal thickness (H) and average crustal V_P/V_S (κ) by stacking TDRF amplitudes at the predicted times of the Moho P-S

conversion and its multiples for different values of H and κ. An average crustal P wave velocity of 6.2 km/s was assumed, based on P wave velocity models derived from the nearby (Fig. 3.1) seismic refraction experiments of Karahan et al. (2001) and Bekler et al. (2008).

The six regional H-κ stacks (Fig. 3.4) show minor variations in crustal thickness. We find H = 35 ± 2 km with average crustal V_P/V_S of 1.73 ± 0.05 for the SW stack (consisting of 111 TDRFs), in contrast to 34 ± 1 km and 1.85 ± 0.05 for the SE stack (171 TDRFs). Both regions show clear stacking maxima in the H-κ space, allowing precise determination of the crustal properties and good agreement between predicted traveltimes for Moho converted and reverberated energy.

The H-κ stack for the CE region (108 TDRFs) also shows a clear maximum, with a slightly greater crustal thickness of 37 ± 1 km but reduced average crustal V_P/V_S of 1.70 ± 0.04, whereas the CW stack (97 TDRFs) does not show a clear single maximum. We interpret the Moho from the maximum at H = 37 ± 1 km and VP/VS = 1.69 ± 0.04 but note a second maximum occurs at H~32 km and a V_P/V_S of 1.82.

To the north of the northern NAFZ branch we find H = 39 ± 1 km and average crustal VP/VS of 1.73 ± 0.04 for the NW stack (236 TDRFs) and H = 37 ± 1 km and average crustal VP/VS of 1.73 ± 0.05 for the NE stack (285 TDRFs). A clear single maximum is observed in the NE H-κ stack whereas another double maxima result is obtained for the NW region, with the secondary maximum at H = 30 km and V_P/V_S = 1.83. We also find a maximum in the NW stack corresponding to a phase conversion at 55-60 km that is absent in all other regional TDRF stacks indicating sub-crustal structure.

Overall, the H-κ stacking analysis demonstrates that the crustal thickness increases from south (34-35 km) to north (37-39 km) and the crust in the eastern half of the DANA region is 1-2 km thicker than in the west. Estimates of average crustal V_P/V_S are typically ~1.70, except for an anomalous result of 1.85 in the SE cluster. We used these first-order constraints on the velocity structure of the crust to migrate TDRFs.

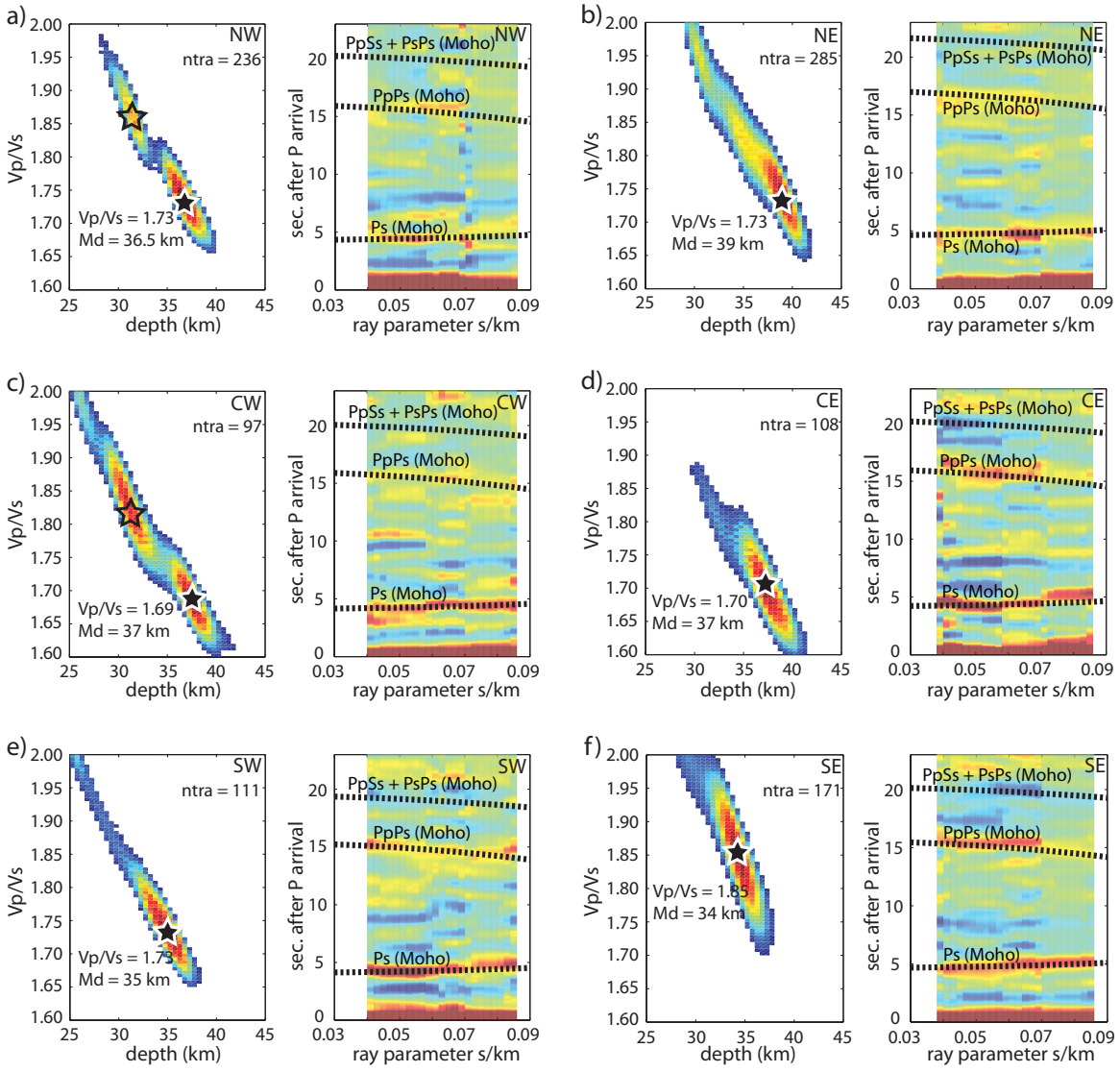

Figure 3.4. Move-out corrected time domain receiver function stacks for the six sub-regions indicated in Fig. 3.3). For each stack (a-f), semblance is plotted in H (crustal thickness) and κ (whole crust V_P/V_S) space alongside raw receiver functions binned by ray parameter. Crustal thickness and V_P/V_S that produce maximum semblance of each stack and corresponding receiver function phases (Ps, PpPs and PpSs+PsPs) are marked by a black star in H-κ space and plotted onto the binned receiver functions. Secondary maxima are shown with an open star.

3.6. Neighbourhood Algorithm Inversion Method and Results

We inverted the six regional MTRF stacks for Earth velocity structure using the neighbourhood algorithm of Sambridge (1999). The inversion scheme attempts to find the velocity model that gives the best fit between the synthetic RF generated from the model and the actual stack (e.g. Bannister et al., 2007). For each inversion, a seven layer parameter space (with search limits defined in Table 3.1) based upon the velocity model of Bekler et al. (2008) was searched using 10001 iterations with 13 initial samples and 13 Voronoi cells resampled at each iteration (see Sambridge, 1999 for details), giving a total of 130026 models tested.

The inversion results for the six regional stacks are shown in Fig. (3.5) and Table (3.2). All inversion results for the six regional stacks show a good fit (with chi-squared misfit 0.063-0.074) to the observed MTRF stacks. We find evidence across the study region for a thin (<1.5 km) low velocity (V_S=1.8-2.3 km/s, V_P/V_S=1.72-1.96) layer at the surface underlain by a rapid transition to typical upper crustal (3.3-3.5 km/s) S wave velocities and V_P/V_S ratios of 1.68-1.81 below depths of 2.2-5.9 km. All regions show mid-crustal S wave velocities of 3.5-3.7 km/s (V_P/V_S=1.72-1.81), which may extend to Moho depths in the NW, SW and SE regions.

In the CW, CE and NE regions, however, a 10-13 km thick, relatively high velocity (V_S=3.9-4.2 km/s; V_P/V_S=1.67-1.74) lower crust is found, corresponding to a weakly positive conversion observed in the migrated TDRF images (Fig. 3.6). The Moho discontinuity is determined at depths between 33 and 39 km for the NW, NE, CW and CE regions with more gradational velocity increase (albeit less than 4 km thick) may exist at the Moho beneath the SW and SE regions (Moho depths: NW=36.8 km; NE=38.7km; CW=36.7 km; CE=36.6 km; SW=32.6-35.6 km; SE=34.7-38.6 km). Uppermost mantle velocities were consistent in all inversion results at V_S=4.4-4.5 km/s and V_P/V_S=1.70-1.75.

In summary, the inversion results show clear evidence for a thicker crust beneath the AA block and eastern IZ crustal terranes (36-39 km) compared to the SZ terrane (33-39

km), in generally good agreement with the H-κ stacking results. Velocities in the lower crust are generally greater beneath the AA and IZ terranes (though not for the western IZ). Mantle velocities are typically lower than the global average.

Table 3.1. Details of the neighbourhood algorithm parameter space searched for the non-linear inversion for S-wave velocity structure (VP, VS, QP and QS denote P- and S-wave velocity and seismic quality, respectively).

Layer	*Min. thickness (km)*	*Max. thickness (km)*	*Min. V_S top (km/s)*	*Max. V_S top (km/s)*	*Min. V_S base (km/s)*	*Max. V_S base (km/s)*	*Min. V_P/V_S*	*Max. V_P/V_S*	*Q_P*	*Q_S*
1	0	5	1.75	2.50	1.75	2.50	1.67	2.00	300	150
2	0.5	5	2.50	3.30	2.50	3.30	1.67	1.82	1450	600
3	0	15	3.30	3.50	3.30	3.50	1.67	1.82	1450	600
4	0	15	3.40	3.60	3.40	3.60	1.67	1.82	1450	600
5	0	15	3.50	3.70	3.50	3.70	1.67	1.82	1450	600
6	0	15	3.90	4.20	3.90	4.20	1.67	1.82	1450	600
7	5	30	4.45	4.70	4.45	4.70	1.70	1.75	1450	600

Table 3.2. Best-fitting receiver function (RF) neighbourhood algorithm inversion results. Final velocity and thickness parameters are shown for each of the seven layers for each of the six regional RF stacks (VP and VS denote P- and S-wave velocity, respectively) (Figs. 2 and 3). Northwest and northeast stacks sample Istanbul-Zonguldak Zone (IZ) crust, central west and central east stacks sample Armutlu-Almacik (AA) block crust whereas south west and south east stacks sample Sakarya Zone (SZ) crust.

	North-West RF Stack (NW)				**North-East RF Stack (NE)**			
Layer	*Thickness (Depth) (km)*	*V_S top (km/s)*	*V_S base (km/s)*	*V_P/V_S*	*Thickness (Depth) (km)*	*V_S top (km/s)*	*V_S base (km/s)*	*V_P/V_S*
1	1.2 (1.2)	1.77	1.91	1.72	0.8 (0.8)	1.76	2.21	1.96
2	2.4 (3.5)	2.82	3.22	1.68	1.2 (2.0)	2.66	3.14	1.68
3	9.0 (12.5)	3.48	3.47	1.74	1.8 (3.8)	3.32	3.41	1.68
4	9.3 (21.8)	3.60	3.44	1.72	9.7 (13.6)	3.56	3.49	1.82
5	14.9 (36.8)	3.53	3.67	1.74	14.1 (27.6)	3.59	3.65	1.76
6	14.3 (51.1)	3.91	4.19	1.82	11.1 (38.7)	3.92	4.13	1.74
7	23.6 (74.7)	4.46	4.45	1.74	16.0 (54.7)	4.46	4.46	1.75
	Central-West RF Stack (CW)				**Central-East RF Stack (CE)**			
Layer	*Thickness (Depth) (km)*	*V_S top (km/s)*	*V_S base (km/s)*	*V_P/V_S*	*Thickness (Depth) (km)*	*V_S top (km/s)*	*V_S base (km/s)*	*V_P/V_S*
1	1.2 (1.2)	2.25	1.88	1.89	1.3 (1.3)	2.46	2.06	1.73
2	1.1 (2.2)	3.12	3.13	1.76	0.7 (2.0)	3.03	2.90	1.81
3	3.7 (5.9)	3.44	3.36	1.81	2.1 (4.2)	3.34	3.44	1.77
4	4.1 (10.0)	3.60	3.56	1.73	13.6 (17.8)	3.60	3.58	1.81
5	14.2 (24.2)	3.59	3.70	1.80	9.3 (27.1)	3.51	3.64	1.73

6	12.5 (36.7)	3.91	4.19	1.72	9.6 (36.6)	3.91	4.10	1.67
7	12.7 (49.4)	4.46	4.45	1.70	8.2 (44.8)	4.46	4.51	1.74
	South-West RF Stack (SW)				**South East RF Stack (SE)**			
Layer	*Thickness (Depth) (km)*	*V_S top (km/s)*	*V_S base (km/s)*	*V_P/V_S*	*Thickness (Depth) (km)*	*V_S top (km/s)*	*V_S base (km/s)*	*V_P/V_S*
1	1.4 (1.4)	2.28	1.97	1.87	1.1 (1.1)	1.95	2.33	1.74
2	2.2 (3.7)	2.98	3.24	1.78	1.1 (2.2)	2.96	2.89	1.76
3	6.6 (10.3)	3.41	3.50	1.68	12.7 (15.0)	3.33	3.45	1.81
4	14.9 (25.2)	3.52	3.50	1.81	8.0 (23.0)	3.58	3.45	1.76
5	7.4 (32.6)	3.53	3.68	1.81	11.7 (34.7)	3.50	3.68	1.80
6	3.0 (35.6)	4.11	4.08	1.73	3.9 (38.6)	4.16	4.20	1.82
7	26.6 (62.2)	4.45	4.52	1.71	7.5 (46.2)	4.46	4.46	1.70

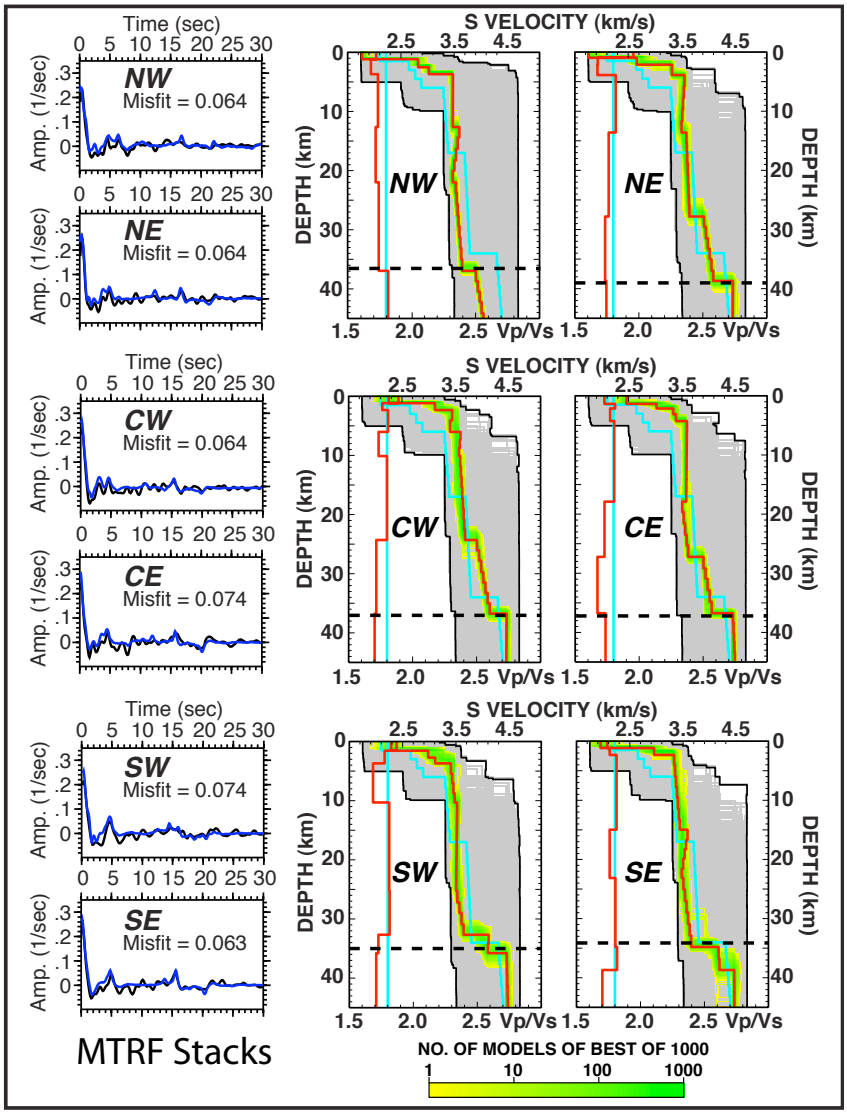

Figure 3.5. Neighbourhood algorithm (Sambridge, 1999a) inversion results for the six regional extended multi-taper receiver function (MTRF) stacks shown in Figure 3. The observed (black) and synthetic (blue) receiver function waveforms for each stack are

compared in the panels to the left with chi-squared misfit values. Corresponding seven layer models are shown in the panels to the right, with the best one thousand (yellow to green lines) models from 10001 iterations (grey lines). The S-wave velocity and V_P/V_S values of the best overall model for each stack (red lines) are displayed alongside a reference velocity model (blue lines) from a nearby seismic refraction experiment (Bekler et al., 2008). Horizontal black dashed lines denote the relevant H-κ stacking depth result for each regional stack (Fig. 3.4). See text for inversion details.

3.7. Receiver Function Depth Migration

3.7.1. Method

We created migrated depth images of discontinuities beneath the DANA array by binning TDRFs according to their piercing points at 35 km depth (e.g. Dueker and Sheehan, 1997). In order to construct representative 2-D profiles we used a bin width of 15 km (similar to the estimated first Fresnel zone width at 35 km) perpendicular to the profile and 7.5 km along profile and linearly stack TDRFs within each bin. We utilized a laterally varying velocity model defined by our MTRF inversion results (Table 3.2) to perform the migration (profiles migrated with H-κ stacking velocity results are shown in Supplementary Figure 3 for comparison). We present two south-north and three west-east profiles through the sub-surface volume sampled by the DANA array (Fig. 3.6). The western profile is located in an area with clear separation of the southern and northern strands of the NAFZ, while the eastern profile samples the area close to the fault splay east of Lake Sapanca (Fig. 3.3). The three east-west profiles sample the three major tectonic blocks in the study area (SZ, AA and IZ, respectively).

3.7.2. Results: Western Profile

Substantial lateral changes in the crust and upper mantle are evident along the ~100 km long western profile (Fig. 3.5.a). On the southern section of the profile the deconvolved P arrival aligns well with zero time, giving support to the choice of velocity model. As the northern branch of the NAFZ is crossed the P arrivals are offset from zero time near the surface location of the NNAF (Figs. 3.2 and 3.5.a), most likely due to low velocity material

filling a <15 km wide regional basin. Further to the north, the upper crust of the IZ is characterised by strongly negative amplitudes, possibly denoting a low velocity layer.

The central section (at distances of -10 to 15 km) of the western profile (Fig. 3.6.a) samples the AA block and pronounced negative TDRF amplitudes may indicate the top of a low-velocity layer in the mid-crust (~17 km depth). This feature is confined to the central section of the profile, as defined by the surface locations of the fault branches, and is underlain by a positive conversion (at ~25 km depth) that most likely signifies an increase in velocity and/or density in the lower crust. Strongly negative amplitudes characterize most of the remainder of the western profile lower crust (particularly at distances of -40 to -30 km and 20 to 35 km and depths of 22-28 km) with the major exception occurring adjacent to the SNAF (at distances of -25 to -15 km), where TDRF amplitudes appear dimmed throughout the entire crust.

The Moho can be clearly identified along the majority of the western profile at depths of ~32-34 km but its P-to-S conversion amplitude decreases from south to north (Fig 6a). An increase in lower crustal velocity as SNAF is approached from the southern end of the profile may explain the observed amplitude decrease (over a horizontal distance of ~45 km). The Moho is deepest (~34 km) beneath the AA block then, moving northwards, its P-to-S conversion has a low and decreasing amplitude beneath the IZ block. The Moho can be traced to the end of the profile at a depth of ~32-33 km, despite its weak signal.

Deeper (sub-Moho) structures are clearly defined beneath the IZ block (distance 10 to 40 km) and are characterized by high TDRF amplitudes, both positive (at 45-50 km depth) and negative (60-70 km depth). These features commence and are shallowest within 5 km of the surface location of NNAF and deepen northwards to the end of the western profile. Sub-Moho conversions beneath the AA and SZ parts of the western profile are only weakly evident (Fig. 3.6.a).

In general, both fault strands are clearly evident in the western section, coinciding with major changes in crustal and upper mantle structure. We observe localized relatively low amplitudes associated with both fault strands; notably migrated TDRFs within ~15 km

of the SNAF (Fig. 3.6.a, distance -25 to -10 km) have relatively low amplitudes and are relatively featureless compared to the higher amplitude signatures from the crust elsewhere beneath the section. The most likely explanation for the low amplitude signals is attenuation and/or scattering of the recorded RF amplitudes due to near-surface (or near-station) heterogeneity and/or deformation caused by faulting in the brittle upper crust.

3.7.3. Results: Eastern Profile

In contrast to the western profile, the crustal structure along the eastern profile (Fig. 3.6.b) appears to be generally less complex with lower migrated TDRF amplitudes. The main evidence for near surface low velocity layers is found in the area north of the NNAF (north of 5 km distance) along this profile. In the AA (-15 to 0 km) and SZ (south of -25 km), we detect low migrated TDRF amplitude conversion, similar to those observed in the SZ of the western profile. Strongly negative amplitudes (at 10-13 km depth) occupy the ~15 km south of the surface location of the SNAF (distance -25 to -10 km) and (at 5-10 km depth) and 15-20 km north of the NNAF.

The most striking feature of the eastern profile (Fig. 6b) is a positive lower crustal conversion (at 25-28 km depth) that extends laterally for ~50 km (distance -25 to 20 km). It lies beneath a weak negative conversion at 18-23 km depth and appears to be the same discontinuity that can be identified on the western profile, corresponding to a region of increased velocity and/or density in the lower crust. However, instead of being confined to the AA crust, on the eastern profile it appears to extend from ~15 km south of the SNAF to ~20 km north of the NNAF. Moderate-strong negative amplitudes, perhaps indicative of a low velocity layer, characterize the lower crust to the north of this feature (25 to 45 km distance). To the south of it, migrated TDRF amplitudes are weak throughout the entire SZ (-40 to -30 km distance).

The Moho dips to the south; with depths of 37-38 km, 36-37 km and 32-34 km beneath the southern (SZ), central (AA) and northern (IZ) sections of this profile, respectively. As in the western profile, Moho P-to-S conversion amplitudes decrease from south to north. Sub-Moho signals are weakly positive and negative in the far north (north of distance 35 km), dipping northwards at depths of 45-50 and 50-55 km, respectively (Fig.

3.6.b).

3.7.4. Results: Southern Profile

The three ~50 km long west-east profiles (Figs. 3.6.c-e) all display clear evidence for lateral variations in crustal structure. The southern profile (Fig. 6c) samples the SZ crust and, in general, it appears less complex than the central and northern profiles described below. We do not find clear evidence for a near-surface low velocity layer but detect a moderately negative upper crustal conversion (10-15 km depth) in the eastern part of the profile (0 to 25 km distance).

High amplitude negative phases in the west of the southern profile (-20 to -5 km distance) may indicate the presence of a low velocity lower crust whereas positive conversions at a depth of ~30 km in the east of the profile probably correspond to the top of the high velocity and/or high density lower crust as observed in the southern part of the eastern profile (Fig. 3.6.b).

The Moho varies from ~32 km in the west of the southern profile (-20 to -10 km distance) to 36-38 km in the central and eastern sections (-5 to 25 km distance). It is characterized by strong P-to-S conversion amplitudes that decrease slightly in the central 10 km of the profile (Fig. 3.6.c). There is little evidence for sub-crustal heterogeneity beneath the southern profile.

3.7.5. Results: Central Profile

The central west-east profile (Fig. 3.6.d) samples the AA block. There is no clear evidence for a substantial near-surface low-velocity layer along this profile. The mid-crust is dominated by high amplitude negative conversions that rise from a depth of ~17 km in the western part (-20 to 0 km distance) to ~13 km in the centre (distance -10 to 0 km) of the central profile. Further east (5 to 20 km distance), the mid-lower crust displays weakly negative P-S conversions at 18 to 22 km depth (5 to 30 km distance).

A distinctive feature of this central profile is the positive amplitudes that define the top of a variable thickness lower crustal layer at depths of ~27, ~22 and ~26 km in the

western, central and eastern sections of the profile, respectively (Fig. 3.6.d, dashed red line). Combined with a varying Moho depth, this relatively high velocity and/or high density layer has a thickness of 6-13 km.

The Moho is predominantly at a depth of 31-33 km along the central profile, but deepens to ~35 km beneath central parts (distance -10 to 5 km). There is no clear evidence for sub-Moho arrivals along the central profile from the migrated TDRFs.

3.7.6. Results: Northern Profile

The northern profile highlights variations in the IZ (Fig. 3.6.e). In the western and central sections (-20 to 0 km distance), TDRF P arrivals are offset from zero time (as observed in the IZ section of the western profile discussed in section 3.7.2), indicative of a substantial (>2 km thick) near-surface low velocity layer. The majority of the upper and lower crust along the northern profile displays an absence of strong P-S converted energy, with near-neutral amplitudes present in all but the easternmost TDRF migrated stack (at 15 km distance).

A weak Moho P-to-S conversion may be present at a depth of ~33 km above the large amplitude positive and negative conversions at 45-50 and ~65 km (west of -10 km) respectively, also identified in the northern parts of the eastern and western profiles (Figs. 6a and 6b). These conversions appear to extend eastwards albeit with greatly reduced amplitudes. The Moho can be clearly identified at a depth of ~32 km in the centre of the profile (-10 km) and deepens eastwards to ~35 km.

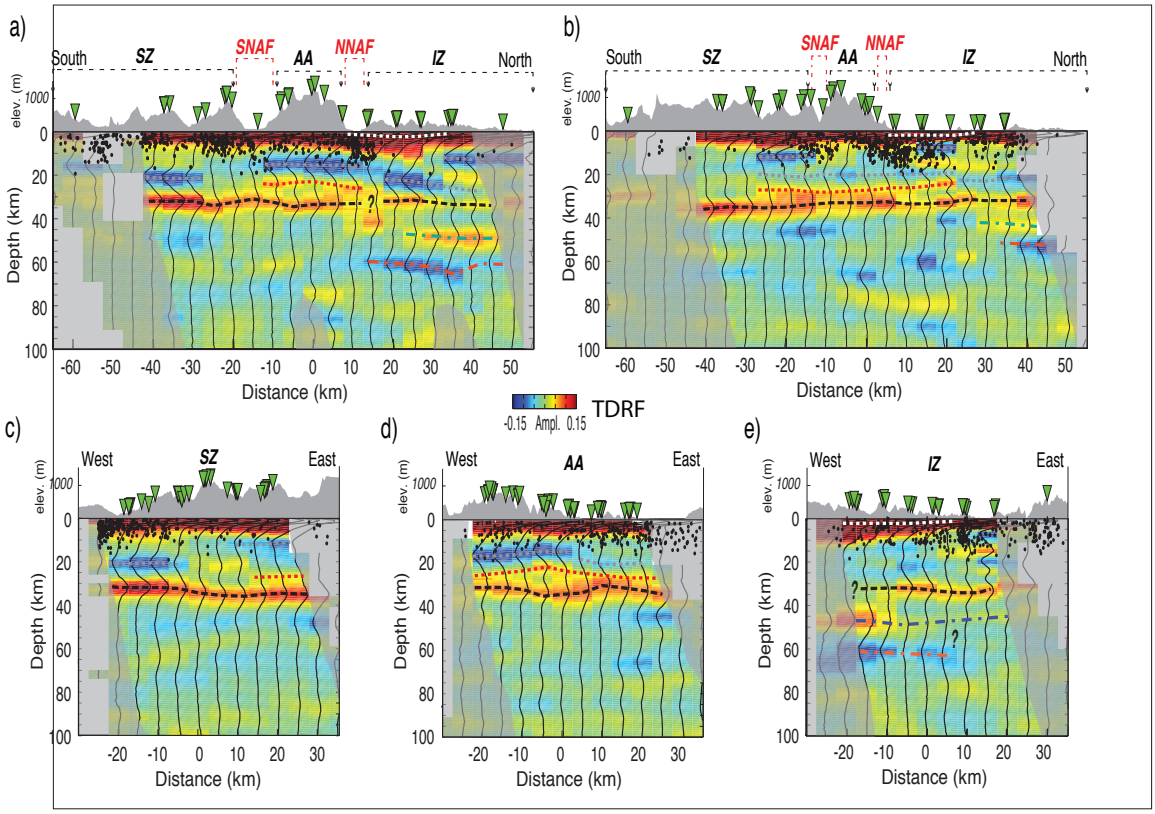

Figure 3.6. Representative south-north and west-east amplitude profiles (the locations of which are shown in Figure 3.3) of 1.2 Hz time domain receiver functions (TDRF) migrated to 35 km (using the inversion results in Table 3.2) with topography and seismicity within ~10 km of the profile (black filled circles) (Poyraz Altuncu et al., 2015). Inverted green triangles denote stations that contribute receiver functions to the migrated image and areas with less than 20 receiver functions are shown in grey. The interpreted Moho (black dashed line), lower crustal positive P-S conversion (red dotted line), near surface P-S conversion (white dotted line) and upper mantle positive amplitudes (blue dash-dot line) are labelled, along with prominent regions of crustal (grey dotted line) and upper mantle (orange dash-dot line) amplitudes. Major crustal terranes (SZ: Sakarya Zone; AA: Armutlu-Almacik Zone; and IZ: Istanbul-Zonguldak Zone) and the locations of the southern (SNAF) and northern (NNAF) branches of the north Anatolian fault are labelled. a) western south-north profile; b) eastern south-north profile; c) southern west-east profile; d) central west-east profile; and e) northern west-east profile.

3.8. Discussion

The short station separation (~7 km) of the DANA array has enabled us to detect strong variations in crustal structure and properties despite the relatively small footprint of this study compared to similar seismological studies. H-κ analysis and neighbourhood algorithm inversion results indicate structural changes both in north-south (across the surface expression of the faults) and east-west directions. The Moho can be detected in most regions and shows measurable variations in depth and velocity contrast on scale lengths of 5 to 10 km. Our high resolution migrated RF images (Fig. 3.6) detail a heterogeneous crust and upper mantle, with the main structural changes correlated to the surface expression of the NNAF and SNAF strands.

3.8.1. The northern fault strand (NNAF)

The northern branch of the North Anatolian Fault Zone (NNAF) was the locus of the disastrous 1999 Izmit earthquake. The migrated RF images show truncations of crustal P-S converted phases in the AA and IZ terranes to the south and north of the NNAF, respectively, and a disturbed Moho conversion is observed over a fault-perpendicular width of <10 km. Local earthquakes recorded during the DANA deployment (Altuncu Poyraz et al., 2015) show that dense seismicity occurred in in the top 15 km vertically above these truncations and, together with the main and aftershock seismicity of the 1999 event (Feigl et al., 2002), indicates that shear on the NNAF in the lower crust occurs aseismically. Truncations of upper mantle lateral features vertically beneath the surface expression of the NNAF (Figs. 3.6.a and 3.6.b) allows tracing of the NNAF to depths of at least 50 km, however, RF migration bin widths of 7 km perpendicular and 15 km parallel to the NNAF limit our ability to discriminate between a fault or shear-zone with widths of less than 7 km. Nonetheless, the western profile (Fig. 3.6.a) shows clear and direct evidence for a narrow zone of shear beneath the NNAF that passes through the entire crust and into the lithospheric mantle with a width of 7-10 km, similar to the width of the most seismically active region in the upper crust (Fig. 3.6a; Altuncu Poyraz et al., 2015), and is likely to be near vertical (dipping 80-90°) (Fig. 3.6.a and 3.7).

Along the eastern profile, truncated structures throughout the entire crust can also be

identified. In contrast to the western profile, these truncations are displaced northwards from surface trace of the NNAF by ~5 km in the upper crust, ~15 km in the mid-lower crust and 25-30 km in the upper mantle (Fig. 3.6.b). In addition, a decrease in the depth and amplitude of the Moho occurs along this profile at ~15 km from the NNAF (Fig. 3.6.b), perhaps related to a change in (lower) crustal velocity properties. The upper mantle structure observed beneath the IZ is similar to that truncated by the NNAF on the western profile but these structures are not continuous and are situated at the limits of our resolution (Fig. 3.6.b). The local seismicity along this profile (Altuncu Poyraz et al., 2015) is more diffuse, probably indicating a wider zone of upper crustal deformation than in the west. This diffuse seismicity, northward offsets of truncations of upper and lower crustal features relative to the surface expression of the NNAF, coherent lower crustal positive amplitudes directly beneath the NNAF and absence of upper mantle terminations together provide evidence that the NNAF at this longitude passes through the crust as a 15-25 km wide zone of deformation. Another plausible model is that a narrow (7-10 km wide) NNAF dips northward at ~65°, if the truncation of crustal and upper mantle converted phases are traced with depth (Fig. 3.6.b and 3.7).

3.8.2. The southern fault strand (SNAF)

Evidence that the SNAF cuts through most of the crust on the western profile is provided by AA block mid- and lower crustal structures truncated directly beneath the topographic low that marks the surface location of the SNAF (Fig. 3.6.a). However, laterally continuous Moho conversions may indicate that the SNAF does not pass into the upper mantle beneath this area. A ~6 km wide region of relatively deep (<20 km) seismicity (Altuncu Poyraz et al., 2015) may show a narrow sub-vertical fault zone extending into the mid-crust. Alternatively, a ~15 km wide region of anomalously low RF amplitudes and a cluster of events at shallower depths (<13 km) south of the SNAF topographic low may signify a wider (<15 km) deformation zone within the crust (Fig. 3.6.a).

Clear upper crustal converted phase polarity changes on the eastern profile coincide with the depth extent (<18 km) and location of locally high rates of seismicity centred below the ‘V’ shaped valley that hosts the SNAF (Fig. 3.6.b). Deeper in the mid-lower

crust, however, negative (at ~20 km depth) and positive (at ~27 km depth) P-S conversions are continuous from ~15 km south of the surface expression of the SNAF to ~20 km north of the NNAF.

If the ~15 km southward offset in the truncations of these deep crustal phase conversions is attributed to a continuous linear shear zone from the SNAF surface expression then a dip of ~65° southwards could be inferred (Fig. 3.6.b). On the other hand, weaker Moho P-S conversions beneath the SNAF-related seismicity (at -25 to -5 km distance), in contrast to a sharp Moho further south, may be evidence for a (sub-) vertical zone of diffuse shear whose width increases with depth beneath the SNAF (Fig. 3.6.b).

3.8.3. East-west structural variation of terranes and fault zone

The observed contrast in properties between IZ and SZ terranes was anticipated since the Intra-Pontide suture marks the boundary between crustal blocks of different provenance (e.g. Okay and Tüysüz, 1999). We also demonstrate previously unknown east-west variations in crust and upper mantle structure within each of the IZ and SZ terranes that are of similar magnitude to variations observed across the NAFZ.

We find evidence for a major crust and upper mantle boundary separating east and west parts of the IZ beneath the DANA array (Fig. 3.6.e), a concept which may be supported by a markedly different sedimentary deposition record in the west and east of the study region (e.g. Okay et al., 1996). A southwest to northeast trajectory separating these two regions would bound, if continued towards the Black Sea, the northern edge of the exposed pre-Cambrian basement of the IZ (Yiğitbaş et al., 2004) and the near-linear southern Black Sea coastline near Zonguldak (Fig. 3.1).

Comparing crustal thickness of the western and eastern IZ, the NA inversion finds the east slightly thinner; the H-κ algorithm finds the opposite, but also finds a secondary maximum for the NW region. These differences may be attributed to greater velocities in the lower crust of the NE region (Fig. 3.6). The sub-Moho structure at depths of 40-60 km beneath the IZ in our study region could be the signature of remnant under-thrust oceanic or continental crust from the closure of an Intra-Pontide ocean (e.g. Robertson and

Ustaömer, 2004). It could also represent crust thickened by an older tectonic event, such as thrusting and subduction related to the closure of the Tethys (e.g. Şengör and Yilmaz, 1981).

In comparison, the SZ crust and upper mantle are less complex and might be considered the stable block within the region, as the most recent deformation to affect the SZ was the Early Jurassic Cimmeride Orogeny (e.g. Pickett and Robinson, 1996). Our constrained crustal thickness estimates of 33-37 km (H-κ), 31-38 km (migrated RF images) and 36-39 km (inversion) are broadly consistent with each other and with previous seismic refraction experiments (32±2 km, Bekler et al., 2008 and ~38 km, Karahan, et al., 2001) but slightly deeper than previous estimates of 29-35 km using RFs (Zor et al., 2006; Vanacore et al., 2013). However, a first order change in crustal RF signature indicates a variation in bulk crustal properties west-east and the possibility of two different crustal terranes comprising the SZ within the study region.

An apparent change in dip of both SNAF and NNAF fault strands, from near vertical to ~65° over an east-west distance of only 25 km, is intriguing (Figs. 3.6.a, 3.6.b and 3.7) and further work is required to debate whether it may be a natural consequence of the two surface fault strands converging or that the NAFZ has re-activated a more complex pre-existing lithospheric suture than previously thought (e.g. Zor et al., 2006).

3.8.4. Inferences for crustal rheology

We infer low velocities in the mid-crust in the AA block at depths of 15-23 km in the west and 19-27 km in the east of our study area (Fig. 6d) that coincide with a creeping layer at 20-25 km that was modelled using post-seismic deformation after the 1999 Izmit earthquake (Hearn et al., 2009). We therefore infer that this lower velocity layer could represent a weak layer in the mid-crust that undergoes viscous creep following a seismic event.

The lower crust of the AA zone has a high velocity that has been previously been interpreted elsewhere as mafic granulite or a layer containing solidified magmatic intrusions (e.g. Cornwell et al., 2010). Lower crustal magmatic intrusions are less

commonly described in large scale continental strike slip settings, although northern parts of the onshore San Andreas fault exhibits a high velocity lower crust that has been interpreted as mafic intrusions (e.g. Henstock et al., 1997).

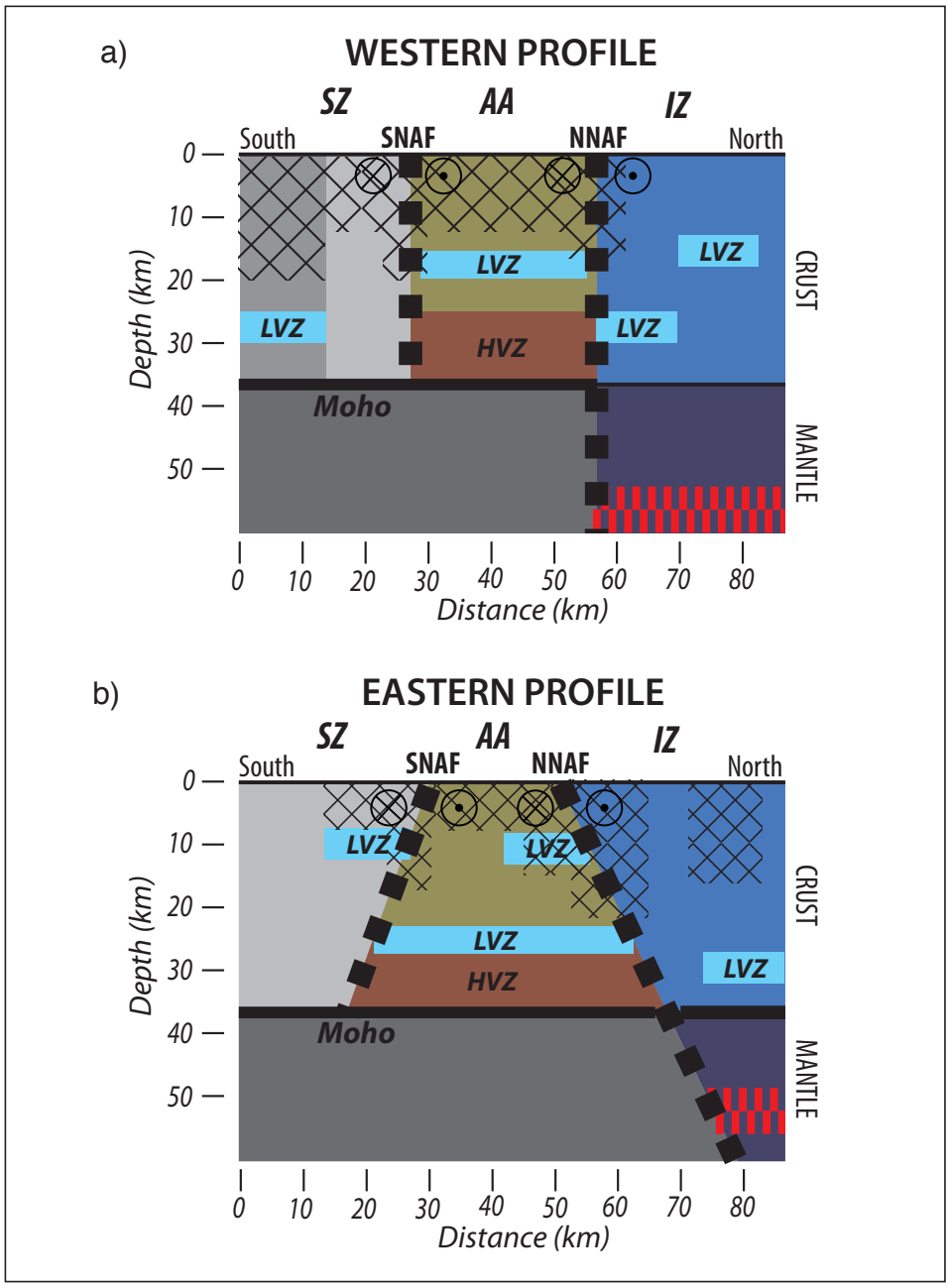

Figure 3.7 – South-north block diagrams to illustrate the variations in crustal structure and interpreted North Anatolian Fault zone structure in the eastern (a) and western (b) parts of the study region. Sakarya Zone (SZ) crust displays two distinct structures (light and mid-grey) in the western profile whilst its upper mantle (dark grey) is featureless and may also

underlie the Armutlu-Almacik (AA) crust (green). The Istanbul-Zonguldak Zone (IZ) crust (blue) and upper mantle (purple) are separated by a weak Moho in the west and the locations of upper mantle structures are highlighted (red hatching). The NNAF and SNAF (thick black dashed lines) are interpreted to be sub-vertical on the western profile and to dip at ~65° to the north and south respectively, on the eastern profile. Low velocity (LVZ) and high velocity (HVZ) zones are also shown as candidate locations for decoupling within the crust, together with regions of notable seismicity (Poyraz Altuncu et al., 2015) (black hatching).

3.9. Conclusion

The high resolution imaging afforded by the dense station distribution of the DANA array allows unprecedented insight into the fine scale structure of a continental strike slip fault, detecting lateral changes in crustal structure over less than 10 km. Based on the structures detected in this study the two fault branches (NNAF and SNAF) of the North Anatolian Fault Zone appear to trace the locations of crustal-scale shear zones developed during the long history of displacement events. Truncation of crustal and upper mantle features in the RFs allows the depth extent of fault strands (or the narrow shear zones that extend down beneath them) to be determined. Beneath the NNAF in the west we can trace the fault zone structure into the upper mantle to a depth of at least 50 km, while the structure beneath the SNAF is more diffuse, perhaps consistent with the observed lesser longer-term strain rate on the southern strand. In western parts of our study area both fault zones seem to dip steeply. Only 25 km further east we infer a significantly shallower dip of both NNAF and SNAF. The NNAF in the lower crust could be as narrow as 7 to 10 km, while the SNAF is probably more diffuse and we do not see clear evidence that it cuts the Moho.

Furthermore, we have shown that lithologic variations exist in the upper, mid and lower crust over distances of less than 10 km and in the upper mantle over distances of less than 20 km. A simple interpretation of these variations is that they arise from the juxtaposition of crustal blocks from different provenances, but localisation of viscous strain can also produce the observed variations in density and depth of seismicity on and around the NAFZ. The identification of differences in dip, depth extent and (possibly)

width of the two NAFZ branches along strike in the study region could indicate that greater strain localization has occurred on the northern strand of the NAFZ. The mid-crustal layer has an anomalously low velocity and could represent a low viscosity region required to explain post-seismic slip following the Izmit earthquake in 1999 (Hearn et al., 2009).

4. IMAGING CRUSTAL STRUCTURE FROM RECEVIER FUNCTION ANALYSIS IN WESTERN TURKEY

4.1. Introduction

Deformation of crust and upper-mantle structures is shaped by under the effect of sited local and regional forces. In this respect, evaluation of crust and upper-mantle structures present variations in different tectonic domains such as subduction, compression or extension zones. Crust is, essentially, stretched in where the extension forces are dominant. The stretched crust gets thinner depending on magnitude of extension and may lead to a creation of a Metamorphic Core Complexes (MCC), which deep seated metamorphic rocks are exhumed to surface. There are couple of regions around the world can be observed this kind of unique structures; Basin and Range in USA, Western Anatolia (WA) in Turkey are some examples.

WA is under the effect of N-S continental extension activity since, at least, latest Oligocene-Early Miocene (Bozkurt and Sözbilir, 2004) with evidenced current GPS observation ranging between 30 – 110 mm/year (Jackson and McKenzie, 1988; McClusky et al., 2000; Nyst and Thatcher, 2004). The cause of extension is modeled with different theories such as tectonic escape (e.g. Dewey & Şengör 1979; Şengör 1979, 1987; Şengör et al. 1985; Görür et al. 1995) or orogenic collapse (e.g. Dewey 1988). Recently, it is stated that back-arc spreading is more relevant to explain the cause of extension. According to this model, convergence between African and Eurasia along the Hellenic and Cyprus trenches is resulted with subduction in N-NE direction beneath Aegean (the back arc) and the Anatolia. Subducting slab geometry is possibly responsible to create the roll back process along Hellenic trench. The roll back is embedded major source of the extension in WA (McKenzie 1978; Le Pichon and Angelier 1979 and Meulenkamp et al. 1988).

There are two different structural phases that are created as a result of N-S extension in WA. Firstly, MCC accumulation (currently NE-SW trending) which rapid exhumation of deep-burial metamorphic rocks and associated granites takes place in the footwall of

presently low-angle ductile-brittle normal faults and accompanied by Miocene red clastics deposition in the hanging wall of the detachment faults. Secondly, modern phase of rift evaluation is occurred by late stretching of crust and a consequent graben formation along Plio-Quaternary high-angle normal faults. These normal faults are E-W oriented that shapes BM, KM and GG with high seismicity (Bozkurt 2001, Bozkurt and Mitwede 2005).

Even though surface observations and proposed evaluation theories (including lower crustal flow) about MCC, there are considerable uncertainties beneath MCC and surroundings in the scale of upper to lower crust and upper mantle. More specifically; one of the suspicions is how underlying crust was affected and behaved during and/or after the exhumation. Additionally, the region is composed of many terranes related to extension and these terranes are shaped by normal faults. However, there is no knowledge about how these faults affect the crust or depth extent of faults. Moreover, there are evidenced thermal hot spots within MCC (Serpen et al., 2009), but there are still skeptical questions about existence of Low Velocity Zones (LVZ) in terms of depth, shape and location beneath MCC (or WA).

Here, receiver function technique which is a robust crustal and upper mantle imaging methodology is applied to teleseismic P wave arrivals recorded by randomly distributed broad-band seismic network (Fig. 4.1). The network samples almost the whole WA and surroundings. Entire region is examined by H-κ analysis to reveal first order depth – Vp/Vs relation then, CCP cross-sections are created along N-S (3), E-W (3) and diagonal (2). The further interpretation and an updated crustal model are made in the vision of new imaged crustal and upper mantle structures.

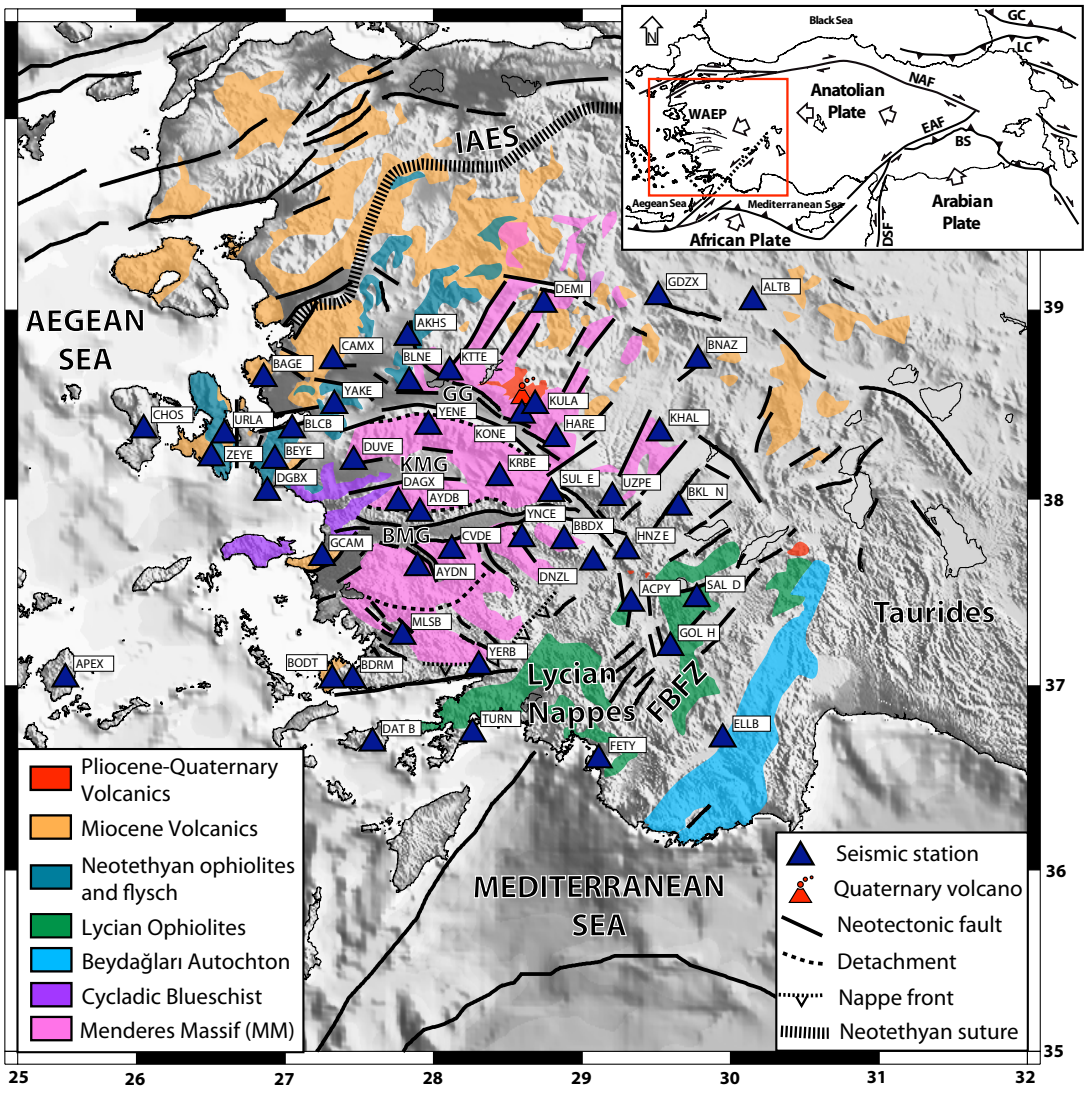

Figure 4.1. Western Anatolia topographic map showing location of seismic stations (dark-blue triangles) with defined geologic units on in set legend and major grabens (GG: Gediz Graben; KMG: Küçük Menderes Graben; BMG: Büyük Menderes Graben). The inset map shows regional plate boundaries (EAF: East Anatolian Fault; FBFZ: Fethiye Burdur Fault Zone; NAF: North Anatolian Fault) and motion of regional plates respect to Eurasia (McClusky et al., 2003) (BS: Bitlis Suture; WAEP: Western Anatolia Extensional Province).

4.2. Geological Overview

Continent-continent collision across the Neotethys in Early Tertiary leads the

amalgamation of several continental fragments such as Istanbul, Sakarya zones and the Anatolia-Tauride block, in western Turkey. All of these continental fragments have distinctive stratigraphy, structural and metamorphic features which are bounded by major suture zones, namely the Intra-Pontite Suture, Izmir Ankara Eskisehir Suture and Inner-Tauride Suture (Okay and Tüysüz 1999). Among these suture zones, Izmir-Ankara-Eskisehir Suture separates the Anatolia-Tauride block in the south. The Anatolia-Tauride block is consist of several tectonic units and forms WA.

Bornova flysch zone (Neotethyan ophiolites and flysch) is located at the northwest of the WA. It is formed by rapid foundering and destruction of Anatolia-Tauride block in Masstrichtian – Early Paleocene (Okay and Altıner, 2007). The zone consists of Maasttrichtian-Lower Paleocene graywacke-shale with block of Mesozoic limestone, mafic, volcanic rock radiolarian chart and serpentines (Okay and Altıner 2007 and references there in). The Cycladic blueschists are sited west of the WA. The unit composes of an olistostomal unit in which eclogite and eclogitic metagabro and presents HP-LT assemblages. They are also surrounded by serpentinities and garnet micaschist (Rimmele 2006).

Lycian napes and Beydağları autochron cover the southeastern corner of WA. The Lycian napes overthrust the metasedimentary sequence of the Menderes Massif in Mid-Eocene (de Graciansky 1972; Okay, 1989). They consist of Lycian Trust Sheets at the bottom with Upper Palaesoic to Cenozoic sediments and the thick Lycian Melange unit. On the top, the Lycian Peridotite Trust Sheet is formed by serpentinized peridotites with a metamorphic sole (Çelik and Delaloye 2003). Beydağları autochron is a unit of carbonates accumulation from the Triassic to the early Miocene, which indicates a part of Mesozoic Tethyan platform. They are also over thrust in the northwest with Lycian napes (Sarı, 2009).

The center of WA is mostly covered by the Menderes Massif. The Massif is a crustal-scale metamorphic culmination with its long axis trending NE-SW (Bozkurt and Oberhansli 2001). It presents one of the largest MCC which deep crustal rocks exhumed and deformed at the surface. Stratigraphy of the massif indicates that an augen gneissic in the core which is most prominent wide spread lithology (Bozkurt and Oberhansli 2001), a

schist cover and a marble cover (Joviet et al., 2012).

Evaluation of the Menderes Massif is occurred in two stages. Firstly, deep buried metamorphic rocks and associated granites were rapidly exhumed. The rapid exhumation helped to create low angle ductile brittle normal faults in the footwall. Secondly, graben formation along Plio-Quaternary high angle normal faults were formed by stretching of crust (Bozkur and Sozbilir., 2004; Bozkurt and Mittwede., 2005). It is, also, very well known fact that the Menderes Massif is dissected by E-W trending grabens such as Gediz, Buyuk and Kucuk menderes granbes which are the most prominent neotectonic creatures in the region (Bozkurt and Oberhansli 2001).

The region has experienced different phase of volcanic activity, which was begun since Late Eocene. The first phase was occurred in Late Eocene and Middle Miocene. The location of this first phase was along the north and south of western segments of IAES, in other words, north and northwest of WA. The activity produced mantle derived magmas that were influenced by crustal melts sources with varying calc-alkaline to high-K calc-alkaline up to shoshonites (Innocetti et al., 2005; Pe-Pier and Piper, 2006, 2007). The second phase began in the Late Miocene and continued up to Early Pliocene. The second phase was dominated at central and southwestern corner of WA. Products in this phase are included mildly alkaline rocks with sodic or potassic affinity which was an indication of increasing crustal component through the time (Joviet et al., 2012). The last phase was occurred between the Pliocene to Quaternary where Afyon, Kula and Isparta-Golcuk were the main eruption centers. The last phase produced basalts, basatines, and phonotephrides with potassic and ultra potassic compositions that were affected by asthenospheric mantle-derived melts (Dilek and Altunkaynak, 2009; Joviet et al., 2012).

4.3. Previous Geophysical Studies

Crustal investigations in WA and surroundings have begun by studies of Markis (1975) and Markis and Vess (1977) using seismic reflection and gravity data. They calculated 22 – 32 km Moho depth beneath the Aegean and 40 – 50 km thick crust for WA. They suggest that the thick crust values beneath WA belong to the crust values before the extension. Similar results are also supported by P and S receiver function investigations of

Li et. al., (2003) and Sodoudi et al., (2006). They found crustal thickness of 20 – 22 km on southern Aegean and relatively thicker crust on the northern Aegean that was 25 – 28 km.

Although the most of current studies support findings of early works on Aegean and Hellenides, it is not relevant for WA. P receiver function studies (e.g. Zhu et al., 2006; Vanacore et al., 2013; Karabulut et al., 2013) show that depth (H) is ranging between 23 – 31.5 km and Vp/Vs (κ) 1.75 – 2.25 with a trend of crustal thinning from East to West. N-S oriented cross-sections imply no visible interfaces mid to lower crust. The studies suggest that the lower crust in WA is three times more viscous than that in the Basin and Range, which is located above flat elevated Moho topography beneath central and southern Menderes Massif. Crustal scale shear wave velocities from receiver function inversions (e.g. Saunders et al., 1998; Tezel et al., 2010) indicate 3.0 – 3.5 km/s ~15 km thick upper crust, 3.5 – 3.7 km/s ~12 km thick lower crust and ~4.5 km/s sub-Moho shear velocities with absence of high frequency regional Sn phase. The absence of Sn phase implies a zone of significant shear wave attenuation immediately below the Moho.

Local tomographic investigations; specifically from upper to lower crust (e.g. Akyol et al., 2006), show low P velocities for a continental crust which varies between ~4.73 to ~6.00 km/s from surface to 15 km depth and ~6.25 km/s down to 20 km. The reasons of low velocities are related to high temperatures, fluids at high pore pressure or partial melt presence located within the crust. Regional studies present the effect of MCC by disappearance of love group velocities at periods greater than 25 s (e.g. Cambaz and Karabulut 2010) and high Pn velocities (~ 8.1 km/s), which are related to large scale crustal extension (Mutlu and Karabulut 2011) in MCC. The results of thin crust together with the low seismic wave velocities suggest the idea that very thin to absent mantle lid, where seismic waves propagation is actually sampling asthenospheric rather than lithospheric mantle (Akyol et al., 2006) and extension is not uniform in WA and Aegean.

Mantle structure beneath Anatolia was revealed by finite frequency P wave travel time tomography (Biryol et al., 2011). He presented low P velocities beneath the Menderes Massif $\delta Vp = -1.4$ % and marginally higher P velocity perturbation south/southwest of the Massif has $\delta Vp = +1.7$ % observed to depths from 60 to 280 km. Similar characteristic of upper-mantle is supported by surface wave tomography (e.g. Salaün et al., 2012) which

indicate slow absolute shear wave anomalies ranging between ~4.0 - ~4.3 km/s within the same area. According to their hypothesis, low velocity perturbations beneath the Massif are possibly resulted from a tear between subducting Aegean and Cyprus slab, which take place almost entire width of WA. WA also coincides with a location of hot upwelling asthenosphere in surface. On the other hand, high velocities in south of the region are defined as down going slab boundary beneath the Aegean (Biryol et al., 2011).

4.4. Receiver Function Data and Computation

WA is covered non-uniformly spaced (distances are varying 10 km up to 55 km) broad-band instruments which are run by Boğaziçi University Kandilli Observatory and Earthquake Research Institute/National Earthquake Monitoring Center (BU-KOERI/NEMC), Disaster and Emergency Management Presidency of Turkey, Earthquake Research Department, (DEMP/ERD), IRIS-GEOFON (Fig. 4.1) and in addition to all; ACPY and SALD stations from temporary Isparta Passive Network. 916 teleseismic earthquakes; origin times identified from the National Earthquake Information Center (NEIC) catalog, with magnitudes $\geq$ 5.5 and epicentral distances between 30° to 95° (Fig. 4.2.a), are separated from continuous data recorded by totally 47 broad band stations between time range of January 2006 - January 2011. All recordings are re-sampled to 20 samples per second to have unique data set since the permanent and temporary networks have different sampling rate on recorded waveforms, The direct P wave arrivals on traces are picked with suppressing noise level applying 0.1 – 5 Hz band pass filter. Then, Z, N-S and E-W components are windowed 40 s before and 120 s after taking direct P wave arrival as a reference. In order to maximize P to S (Ps) energy on horizontal components, N-S and E-W components are rotated to incoming wave front. Radial and transverse components are obtained as a result of this rotation.

Iterative time domain deconvolution (Ligorria and Ammon, 1999) with 1.2 Hz cut off frequency by width of 2.5 Gaussian type low pass filter are applied to rotated horizontal and vertical components. Horizontal components are placed as nominator while vertical ones are placed as denominator. The deconvolution is completed with abundance of radial and transverse RFs including both high and low signal to noise ratio waveforms. Decision of high quality receiver functions leads us to make variance reduction at least 70% and/or

higher as a basic selection criteria and then, clear Ps converted and multiple phases are visually inspected and separated for each station. 3563 high quality RFs are chosen to utilize in H-κ and CCP analysis Fig. (4.2.a). In order to increase the signal to noise ratio and to observe coherence of Ps converted and multiple phases at stations, back-azimuth bin plot (Fig. 4.2.b) is made up for each station. RFs bins are created and averaged in every 10° increment begin from 0° up to 360°. BEYE (Fig. 4.2.b) and the other most stations indicate strong Ps Moho converted phase around, 3.2 s that is followed by PpPs multiple at 11.4 s. There are not strong second multiple phases (PpSs+PsPs) on RFs waveforms, but weighting factor at H-κ stacking calculations (Fig. 4.2.c) is incorporated to deal with smeared multiple phase arrivals.

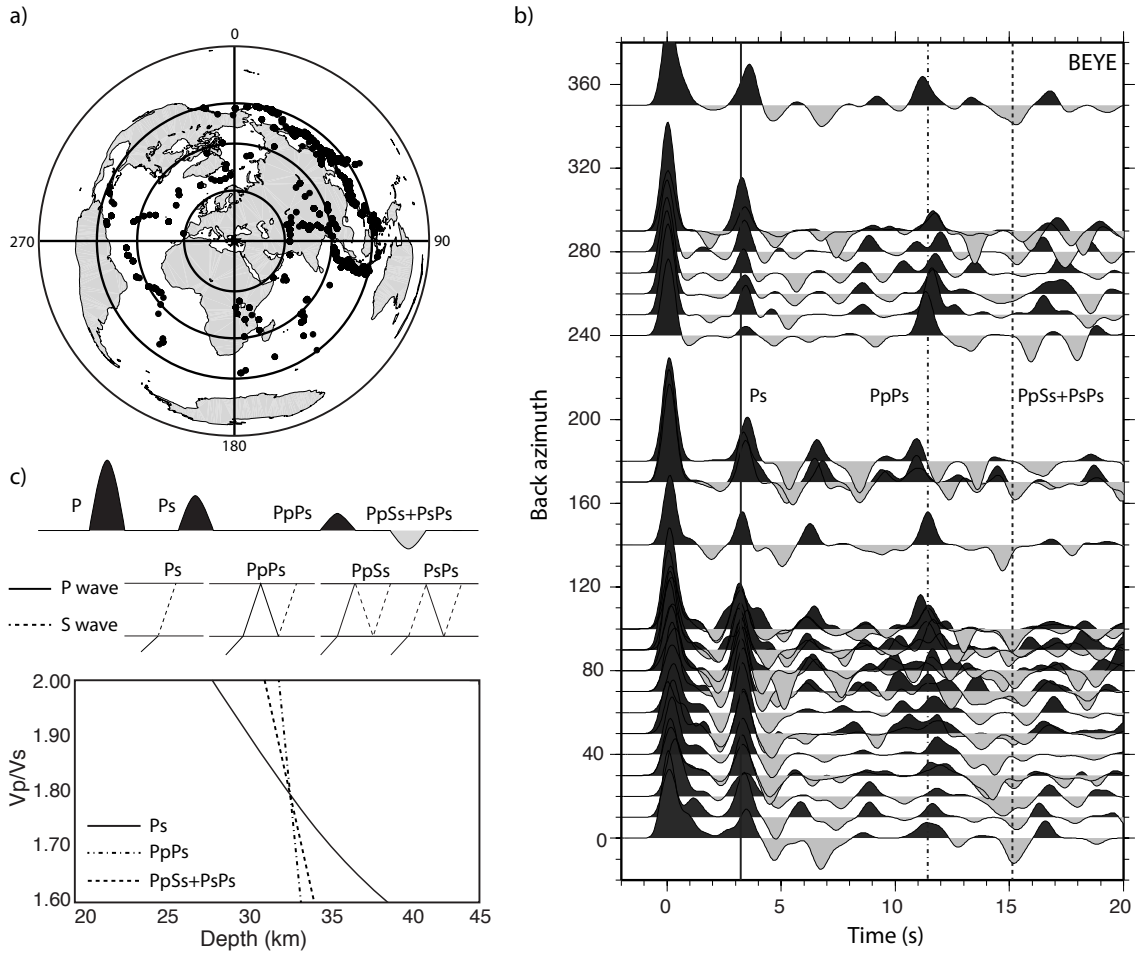

Figure 4.2. Teleseismic earthquake locations, back-azimuth stack of receiver functions and basics of H-κ stacking. a) Azimuthal distribution and location of teleseismic earthquakes (black circles) occurred time period of 2006 to 2011 which have mb ≥ 5.5 and 30^{o} and 95^{o}

epicentral distances. b) Stack of radial receiver functions at BEYE station with respect to back-azimuth and defined Ps, PpPs and PpSs+PsPs arrivals. c) Synthetic radial receiver function with expected phases and sketched homogeneous two layer model placed on the top and middle respectively. Maximum summed amplitude location on H-κ (depth and Vp/Vs) domain with interaction of Ps and crustal multiples located at the bottom (Zhu and Kanamori, 2000).

4.5. Results

4.5.1. H-κ Stacking Results

Station YENE (Fig. 4.3.a) and KULA (Fig. 4.3.b) sample two different locations of Menderes massif (MM) with number of 70 and 179 high quality RFs sequentially. YENE is located on the southern edge of the Gediz Graben (GG) and KULA is located in northern edge of GG where the place is location of Quaternary volcanism (Fig. 4.1). The consistent result of these stations indicates that ~30 km Moho depth with low Vp/Vs ratios 1.65 and 1.73 for YENE and KULA respectively. Both stations have clear Ps and multiple arrivals that are supported by move-out plots (Fig. 4.3.a and 4.3.b).

ZEYE is located on western edge of MM upon Neotethyan ophiolites and flysch zone. The station presents respectively shallower Moho ~25.5 km and higher Vp/Vs ~1.87 with number of 47 RFs (Fig. 4.3.c). Another remarkably different result is indicated by UZPE, which is located in eastern end of the MM (Fig. 4.3.d). The calculated crustal thickness, a stack of 53 RFs, is ~28 km. The thickness value is compatible with rest of the stations above central MM. But compare to rest; UZPE has one of the highest ~1.96 Vp/Vs ratio in the region.

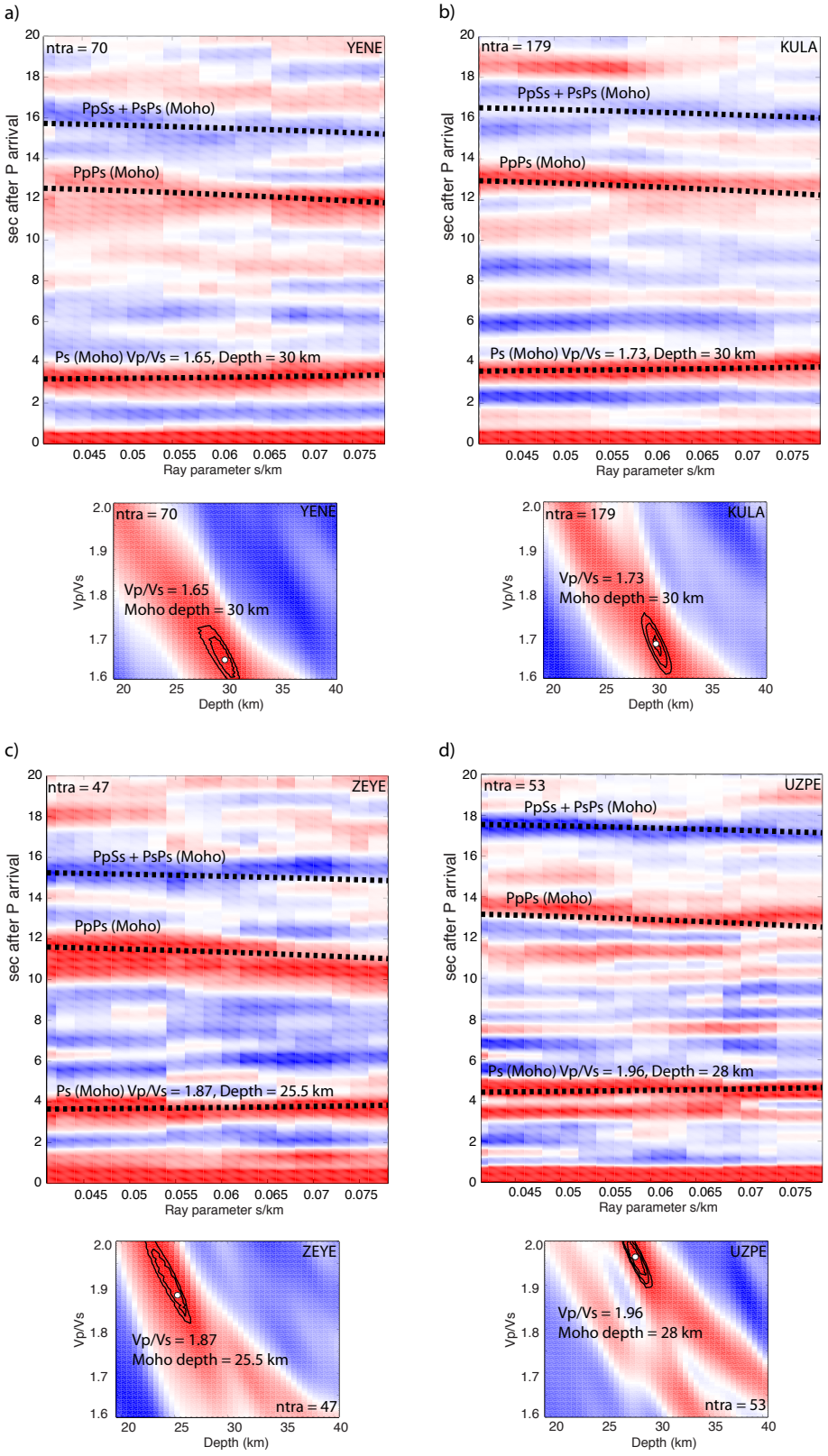

Figure 4.3. Example stations in the order of within MM (a-b), west of MM (c) and east of MM (d). Receiver functions stacked and move-out corrected with respect to ray parameter

and time. Additionally, predicted arrival time of Ps, PpPs and PpSs+PsPs phases marked for all example stations (a-d) at the top. Calculated H-κ solutions with showing maximum amplitude location (white-circle) are at the bottom.

The overall results of H-κ stacking analysis on each station in WA (Fig. 4.4.a and 4.4.b), the region can be interpreted as mainly three sections. To begin from the east of MM, Moho depth is ~33-35 km beneath the north of eastern section. The crustal thickness has significant increase in south ~39 km where the region bordered by FBFZ. However, passing FBFZ through to southeast beneath Beydağlari Autochton, Moho has respectively shallower values ~33 km. Additionally, variations in Vp/Vs are calculated from north to south in the eastern section. Vp/Vs values are comparably low between ~1.60 – ~1.80 in the north but the values suddenly increase to ~1.80 – ~2.00 towards the south where section stays between the MM and Lycian Nappes. To continue to south, Vp/Vs gets low to ~1.75 in Lycian Nappes and to south-east, there is a small amount of increase in Vp/Vs up to ~1.85 beneath Beydağlari Autochton.

The center section of WA presents crustal thickness between 29-32 km and ~1.60 - ~1.80 Vp/Vs. The H-κ stacking results are mostly compatible with each other in central section except one location where two stations, AYDB and DAGX, stay between ridge of the northern edge of Buyuk Menderes Graben and southern edge of Kucuk Menderes Graben, respectively. Although stations are so close to each other and coherent crustal thickness value, Vp/Vs values are low beneath DAGX (~1.67) and high beneath AYDB (~1.91). The western section indicates thinner Moho results that vary between 25 – 28 km. Vp/Vs values are low at the western end of MM ~1.60 - ~1.75, but higher to further west >~1.80 along NE-SW oriented stations (Fig. 4.4.b).

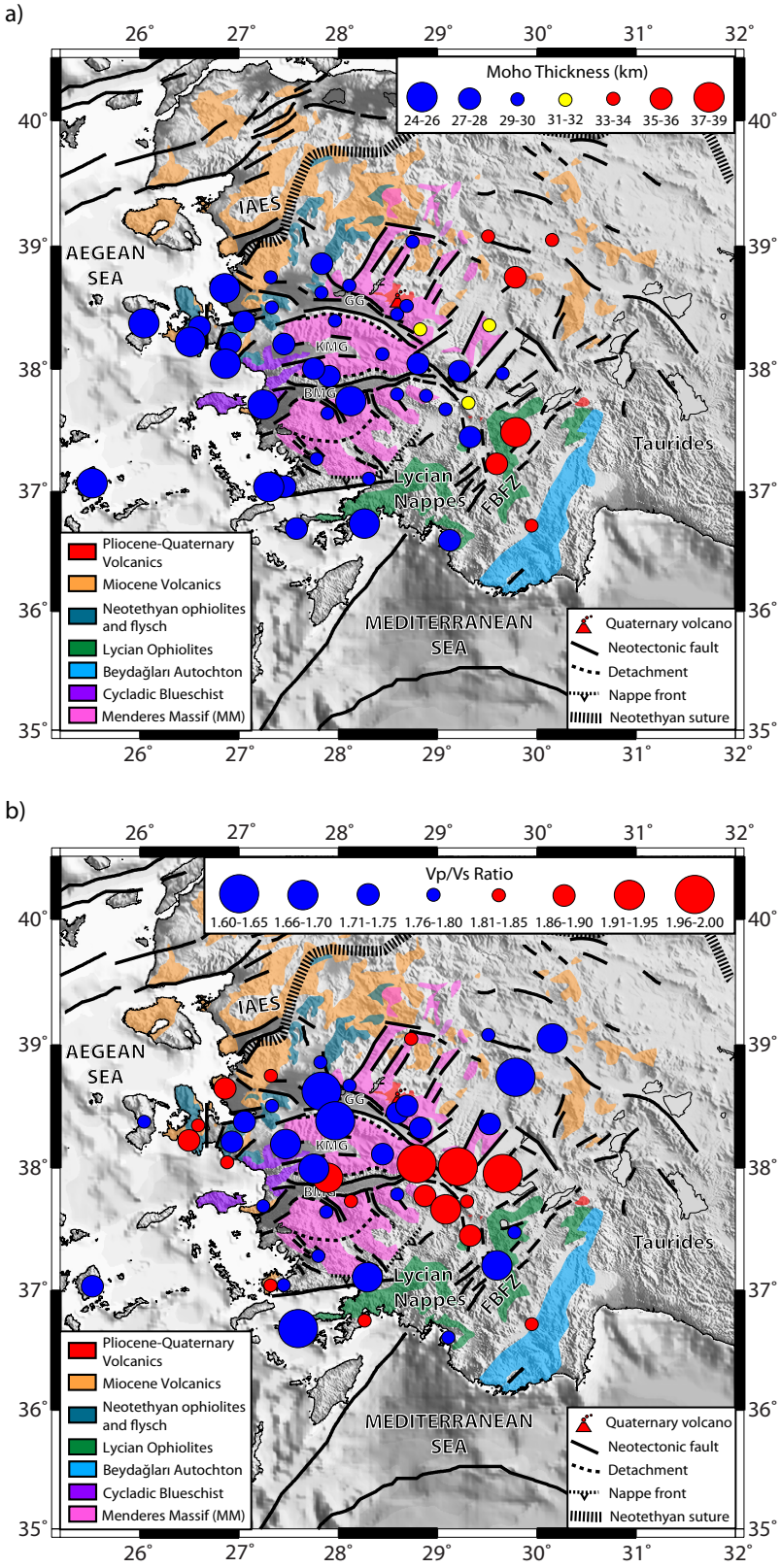

Figure 4.4. Moho depth variation and Vp/Vs change on topographic map of western Anatolia. a) Moho depth is defined with different size of circles; red means thicker and

blue means thinner crust. b) Average crustal Vp/Vs is showed, low Vp/Vs are blue and higher Vp/Vs are red circles.

4.5.2. Common Conversion (CCP) Stacking Results

4.5.2.1 CCP Specifications on Western Anatolia

Common conversion point (CCP) stacking (Dueker and Sheehan, 1997, 1998) is applied to build spatial images of discontinuities beneath WA along 2-D cross sections. The method creates geographical bins of Moho pierce converted Ps and its multiple phases and then, stacks them in each bin width with given bin interval and bin radius. In this chapter, Moho pierce depth is calculated by an average of H-κ analysis results that is 29 km (section 4.5.1). CCP profiles are created by each 10 km with 20 km bin radius for 360x400 km rectangle shaped WA.

Constant and laterally changing Vp/Vs are utilized to calculate true depths of discontinuities along cross sections since depth of velocity contrasts is significantly sensitive to Vp/Vs rather than Vp (Zandt et al, 1995). Zhu and Kanamori (2000) propose that a 0.1 change in Vp/Vs creates 4 km difference in depth while 0.1 km/s change in Vp outcomes only with 0.5 km change in depth. The first attempt to utilize “correct” Vp/Vs has begun with making a dense grid (5x10 km) of linear Vp/Vs interpolation by taking into account of H-κ analysis results for each stations. The reason of a dense grid cells is to provide corresponding Vp/Vs for each geographical bin location. CCP images are produced by using interpolated Vp/Vs values (e.g. Fig. 4.5.d) and corresponding Vp/Vs values are plotted (e.g. red line in Fig. 4.5.e). However, interpolated Vp/Vs values do not completely satisfy true depths of discontinuities in relation with isostatic equilibrium, especially, at the edges of WA where the distance between the stations are high and number of stations are few. So the second attempt to find out “correct” Vp/Vs are performed by producing Ps and PpPs CCP stacks for 1.78 constant Vp/Vs (as a result of average H-κ analysis for each stations). Preliminary depths of discontinuities are defined by Ps and PpPs phases with using the constant Vp/Vs (Fig. 4.5.a and 4.5.b). The depth of clearly identified Ps and PpPs phases is picked with respect to bin distances along each CCP cross-sections (e.g. black stars on Fig. 4.5.a and 4.5.b). By taking into account of

constant ray parameter (0.06), Vp/Vs (1.78) and Vp (6.2 km/s) in the following formulas,

$$a_1 = \sqrt{\left(\frac{1}{V_P}\right)^2 - (rp)^2} \tag{4.1}$$

$$a_2 = \sqrt{\left(\frac{V_P / V_S(const.)}{V_P}\right)^2 - (rp)^2} \tag{4.2}$$

$$a_{3(i)} = \left\{\left[\frac{Ps_{(depth)_{(i)}} * (a_2 - a_1)}{PpPs_{(depth)_{(i)}} * (a_1)} * 2\right] + 1\right\}^2 \tag{4.3}$$

$$"correct" V_P / V_{S(i)} = \sqrt{a_{3(i)} * \left[1 - (rp^2 - V_P^2)\right] + (rp^2 * V_P^2)} \tag{4.4}$$

where $Ps_{(depth)}$; picked Ps depth on constant CCP Ps stack, $PpPs_{(depth)}$; picked PpPs depth on constant CCP PpPs stack, V_P; P wave velocity (6.2 km/s), $V_P / V_S\,(const.)$; constant Vp/Vs (1.78), i; lateral distance of bin location along the profile.

"correct" Vp/Vs is calculated for each 10 km bin interval along CCP cross-sections (e.g. green line in Fig. 4.5.e). Then, the same CCP profiles with the same bin settings are plotted again utilizing "correct" Vp/Vs values and true depths are presented (e.g. Fig. 4.5.c). The advantages of this method are; mis-undulations are kept away as a result of linear interpolation and "correct" Vp/Vs is calculated for respectively obtained Ps and PpPs depths within the same bin and bin location.

3 E-W, 3 N-S and 2 NW-SE cross-sections are created in order to reveal detailed crustal and upper mantle image beneath the region.

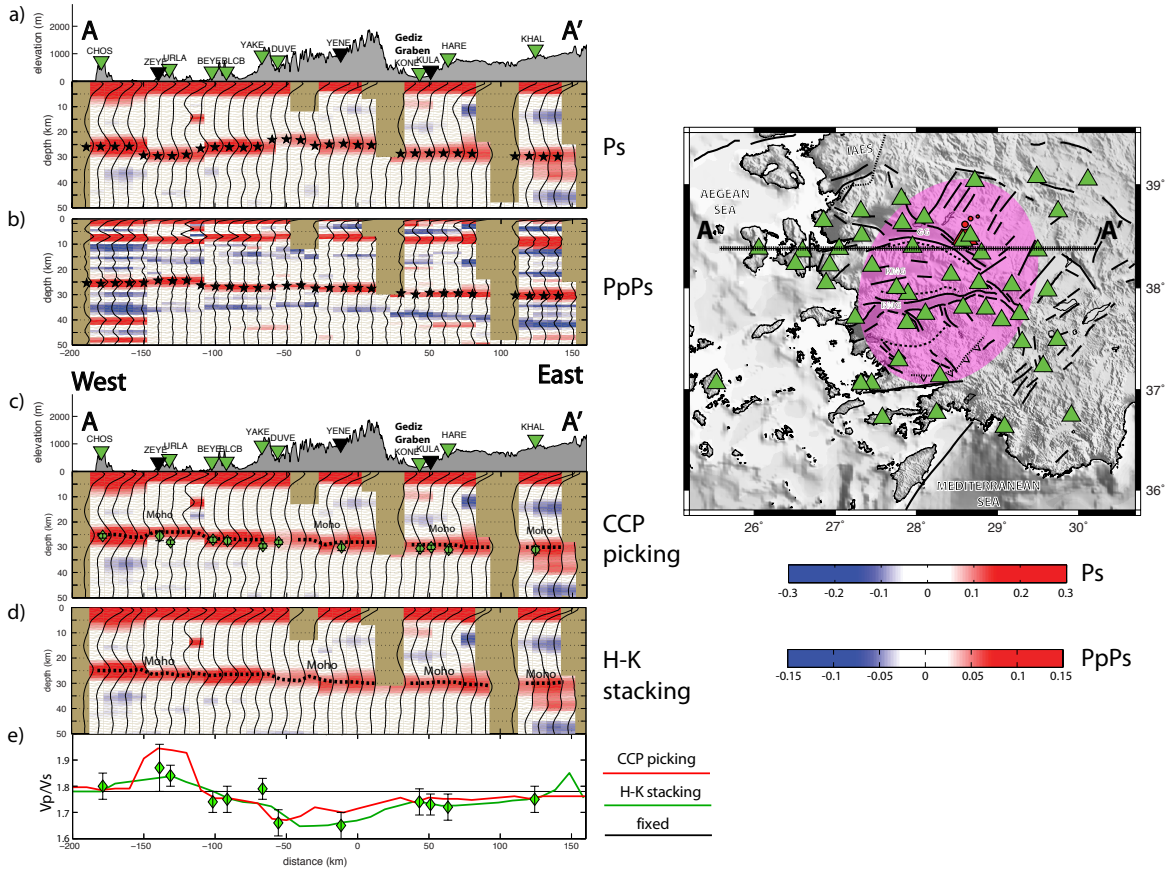

Figure 4.5. Calculation of correct Vp/Vs and true Moho depth are using CCP cross-sections (left hand side) with location of profile on topographic map (right hand side). Ps and PpPs phase CCP stacks for constant Vp/Vs (1.78) with observed and picked Moho (black-stars) discontinuity (a-b). c) Ps phase CCP stack for calculated correct Vp/Vs with H-κ solution depths and depth error bars (green diamonds and solid black error bar). d) Ps phase CCP stack for linearly interpolated Vp/Vs result of each station. e) Correct and interpolated Vp/Vs variation along the profile with solid green and red line respectively. Average constant Vp/Vs is showed solid black line. Vp/Vs values with error range are plotted with green diamonds and black error bar on it.

4.5.2.2. Results: West – East CCP Profiles (W-E)

West – East CCP stacks presents durable Moho beneath WA but upper and middle crust structure reveals distinct phase arrivals through laterally located geologic units and grabens. Profile A-A' (Fig. 4.6.b) presents direct P waves aligned well with the zero time in east (-30 to 150) and small offsets in west (-180 to -50). A narrow (~5 km wide) but

clear positive receiver function amplitude ~13 km depth exits with accompanying negative amplitude beneath at ~17 km depth in middle crust at -110 km distance which coincides with the western edge of Menderes Massif. A faded negative phase existence is located at ~13 km depth at 0 km distance before sampling GG. Positive phase amplitude is located at upper crust (~10 km) and negative amplitude at lower crust (~19 km), which appears within the GG. Passing GG to east, a sing of LVZ exists with clear negative amplitude. The top level of LVZ is located at upper crust (depth of ~10 km) and seems to dipping toward east down to middle crust (depth of ~15 km). Moho is well sampled along 350 km long profile indicating thinnest in the west (~25 km) and thickest in the east (~30 km). Although there is no upper mantle structure observed in west and center of the profile, a wide positive phase arrival at ~39 km depth with clear amplitude exists at eastern edge of profile. "correct" Vp/Vs has the highest value in the west which is ~1.80 to 1.85 and starts to decrease at western edge of the Menderes Massif. "correct" Vp/Vs is lowest at center of the Massif ~1.65, then begins to increase to eastern edge of the Massif and it reaches up to ~1.80 eastern end of profile.

Profile B-B' (Fig. 4.6.c) indicates a similar gently dipping Moho towards to east as showed in A-A'. Although the Moho has low amplitude at some places (e.g. -20 and -10 km distance) in B-B', it is traced well along the profile. Phase differences become clear above Moho after eastern edge of Kucuk Menderes Graben. LVZ between ~10 - ~15 km depths are located at 50 – 80 km and 130 – 150 km distance above 100 km wide, continuous lower crustal structure at ~20 km depth. An interesting feature about this lower crustal zone is that it seems east dipping beneath Menderes Massif but it becomes shallower just after the eastern end of the Massif. "correct" Vp/Vs is above the regional average in the west (~1.85), lowest in center (~1.70) and indicates marginal increase at 30 km distance to east where it goes up to ~1.95.

Profile C-C' (Fig. 4.6.d) signifies clear direct P wave off set at 0 to 70 km distance and dips toward east within this distances. The profile shows clear LVZ mostly located in the center of profile which begins at upper crustal depths (~10 km) and has maximum depth at lower crust (~20 km) within 100 km wide lateral distances. There are faded positive amplitudes at eastern end of profile but those are not clear as LVZ in the center. "correct" Vp/Vs is ~1.80 in the west. It seems to degrease towards the center but has

average value at ~1.78 and increases at east end up to 1.95.

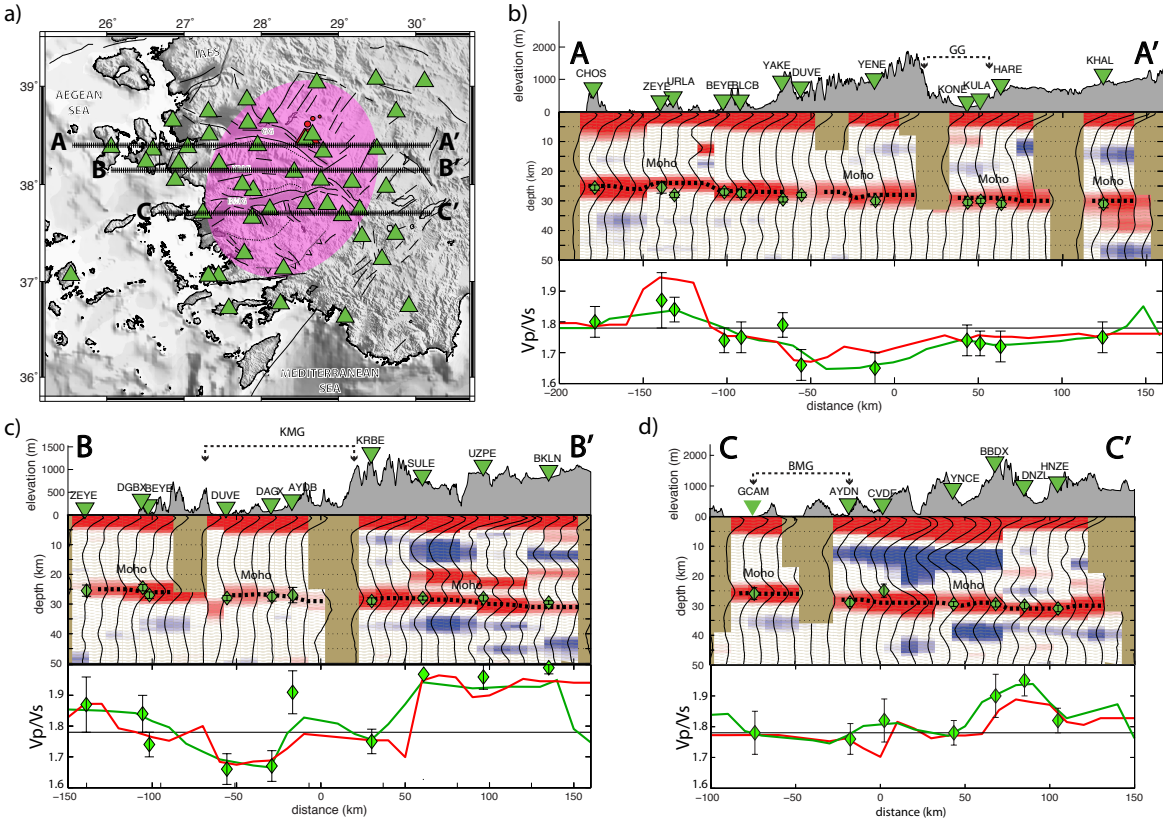

Figure 4.6. Representative West - East correct Vp/Vs Ps phase CCP stacks on north (A-A'), center (B-B') and south (C-C') of MM. Correct (solid green line), interpolated (solid red line) Vp/Vs and Vp/Vs results obtained from H-κ solutions with error range (green diamonds with black solid error bars) plotted bottom of each cross section (b-d).

4.5.2.3. Results: South – North CCP Profiles (S-N)

Profile D-D' (Fig. 4.7.a) is located at western edge of Menderes Massif. Direct P wave arrivals mach well with the zero time on the southern part but indicate offset, close to northern end of profile. Mid-crustal phases do not exist beneath the major graben systems, however, different polarity change is observed in depth of ~11 km at the distance between -100 to -50 km on the south. This polarity change can possibly be a sing of middle or upper crustal anisotropy where the negative sing of polarity turns to positive at directly beneath Gökova Graben. Another middle to lower crust negative phase is observed at depths of ~16 and 22 km which seems very beginning of LVZ at the northern end of profile. Moho is ~30

km depth at the southern end of the cross-section. Passing Gökova Graben to north, Moho depth decreases to ~25 km and almost stays stable with the same depth beneath Menderes Massif. Moho gets down to ~30 km depth again at the northern end of profile. “correct” Vp/Vs presents the similar characteristics with Moho change. It is ~1.80 (except -90 km distance) at the south and where the cross-section begins to sample Menderes Massif. “correct” Vp/Vs gradually decreases down to ~1.70 and then increases to 1.80 at the north where the profile finishes to sample the Massif.

Profile E-E’ (Fig. 4.7.c) is well-sampled major graben systems in Menderes Massif. LVZ is clearly imaged at different depths with top level begin from upper crust (depth of ~10 km) and gets down to lower crust (depth of ~20 km) along -80 to 90 km distance. Moho presents small undulations between the depths of ~25 to ~30 km range mostly flat shape along the profile. “correct” Vp/Vs is ~1.80 at south but it decreases down to ~1.70 beneath Menderes Massif except beneath northern edge of Buyuk Menderes graben where the “correct” Vp/Vs marginally increases up to ~1.90 then decreases to its lowest value ~1.62 beneath the Gediz Graben. “correct” Vp/Vs increases to ~1.80 after the northern edge of Gediz Graben.

Profile F-F’ (Fig. 4.7.d) is one of shortest cross-section selected in WA. Direct P arrivals present offset at the south but they align with the zero time at north. Clearly imaged LVZ is located at the distances between 20 to 80 km with its top level depth begin at upper crust (~8 km) and traced down to mid-crust (~18 km). 40 km wide lower crustal positive amplitudes are observed at the depths of ~20 km above flat shape Moho. Moho presents almost straight line without any topographic change at the depth of ~30 km. “correct” Vp/Vs has one of the highest values ranging between ~1.90 to ~1.97 close to northern edge of Buyuk Menderes Graben but after this, it varies between ~1.75 to ~1.80.

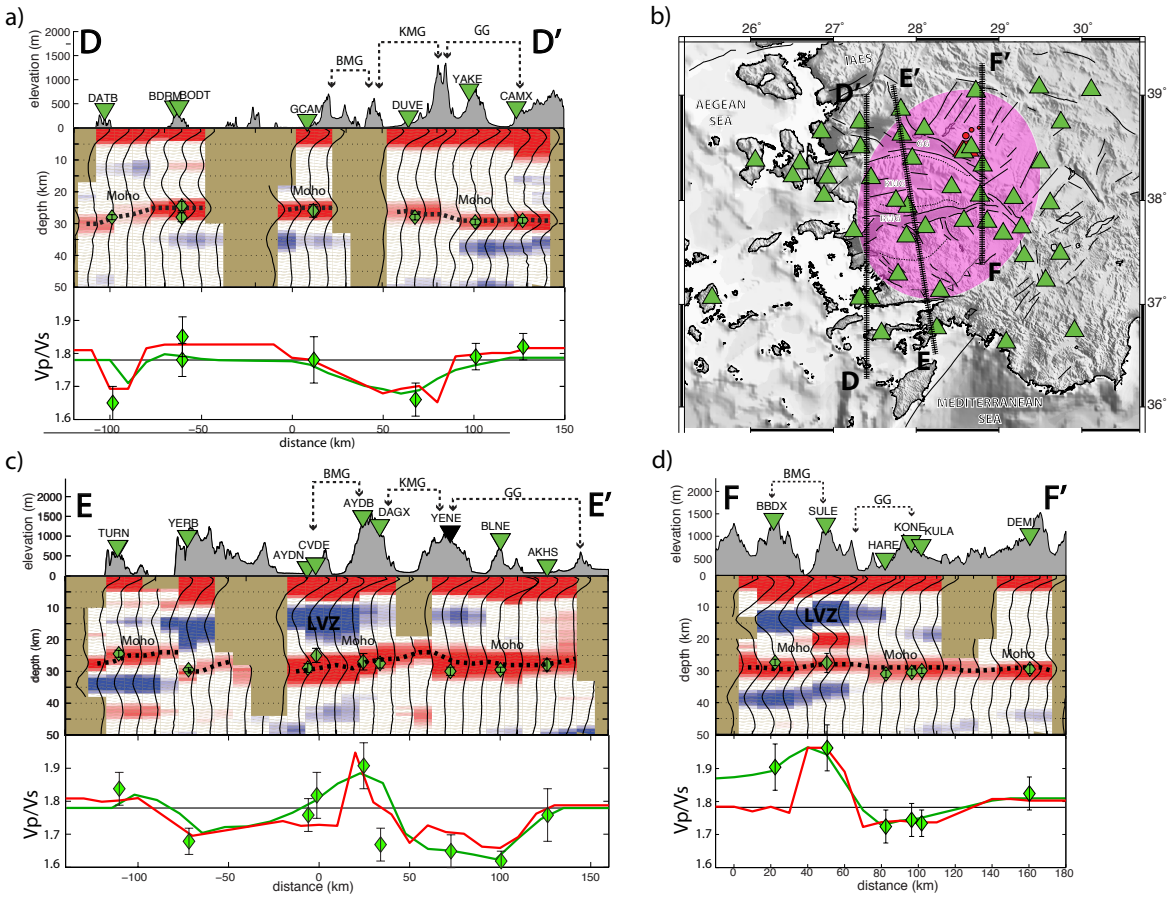

Figure 4.7. Representative South – North correct Vp/Vs Ps phase CCP stacks on west (D-D'), middle (E-E') and east (F-F') of MM. Correct (solid green line), interpolated (solid red line) Vp/Vs and Vp/Vs results obtained from H-κ solutions with error range (green diamonds with black solid error bars) plotted bottom of each cross section (a, c and d).

4.5.2.4. Results: SouthEast – NorthWest CCP Profiles (SE-NW)

Profile G-G' (Fig. 4.8.b) is the longest profile which samples FBFZ on SE corner and diagonally samples Buyuk Menderes Graben and Gediz Graben in the Menderes Massif along NW direction. LVZs appear at upper and mid crustal depths where they are picked at ~8 km as a top level of LVZs and degrease to ~15 km at -160 to -140 km, 30 to 60 km and 130 to 150 km lateral distances. A clear phase change from positive to negative is observed below the mid crustal depths (~16 km to ~20 km depths) beneath FBFZ. The negative phase turns to positive as soon as after NW edge of FBFZ continue laterally to ~50 km distance beneath the Menderes Massif which is assumed as a indication of lower crustal

feature. Moho is at the depth of ~35 km and it underlies below ~70 km wide and ~8 km thick of LVZ at SE corner and in FBFZ. A significant Moho feature is imaged at -60 km distance which indicates clear Moho step (~5 to ~8 km) close to NW edge of FBFZ where Moho is located at the depth of ~27 km. Moho is gently deeper (~30 km depth) at -20 km distance and it gets thinner (~27 km) further to NW end of the profile. "correct" Vp/Vs varies between ~1.75 to ~1.80 at SE corner and beneath FBFZ. It has maximum value (~1.90) between the FBFZ and Buyuk Menderes Graben then gradually decrease to lowest value ~1.70 beneath Gediz Graben. "correct" Vp/Vs presents gradual increase to end of NW corner after edge of Gediz Graben.

Profile H-H' (Fig. 4.8.c) samples the easternmost part of WA with partially including FBFZ. Upper crustal LVZs are imaged at depths of ~12 km along -140 to -120 km, -10 to 30 km and 40 to 60 km distances. Lower crustal positive phase is traced at ~20 km depth beneath FBFZ and 0 – 40 km distances. However, this phase changes its polarity to negative at the NW end of profile. Moho is located at ~35 km depth and gradually dipping to NW below 60 km wide LVZ beneath SE corner and up to NW end of FBFZ. It is clearly observed Moho step at -20 to -10 km distance again, which Moho levels up to ~31 km and continues to NW with perturbed between ~30 to ~32 km depths. "correct" Vp/Vs is quite stable (~1.80) at NW end of FBFZ and gradually increases to its maximum ~1.95 at 20 km distance. Then, it decreases gradually and stable at the value of ~1.78 up to end of NW corner.

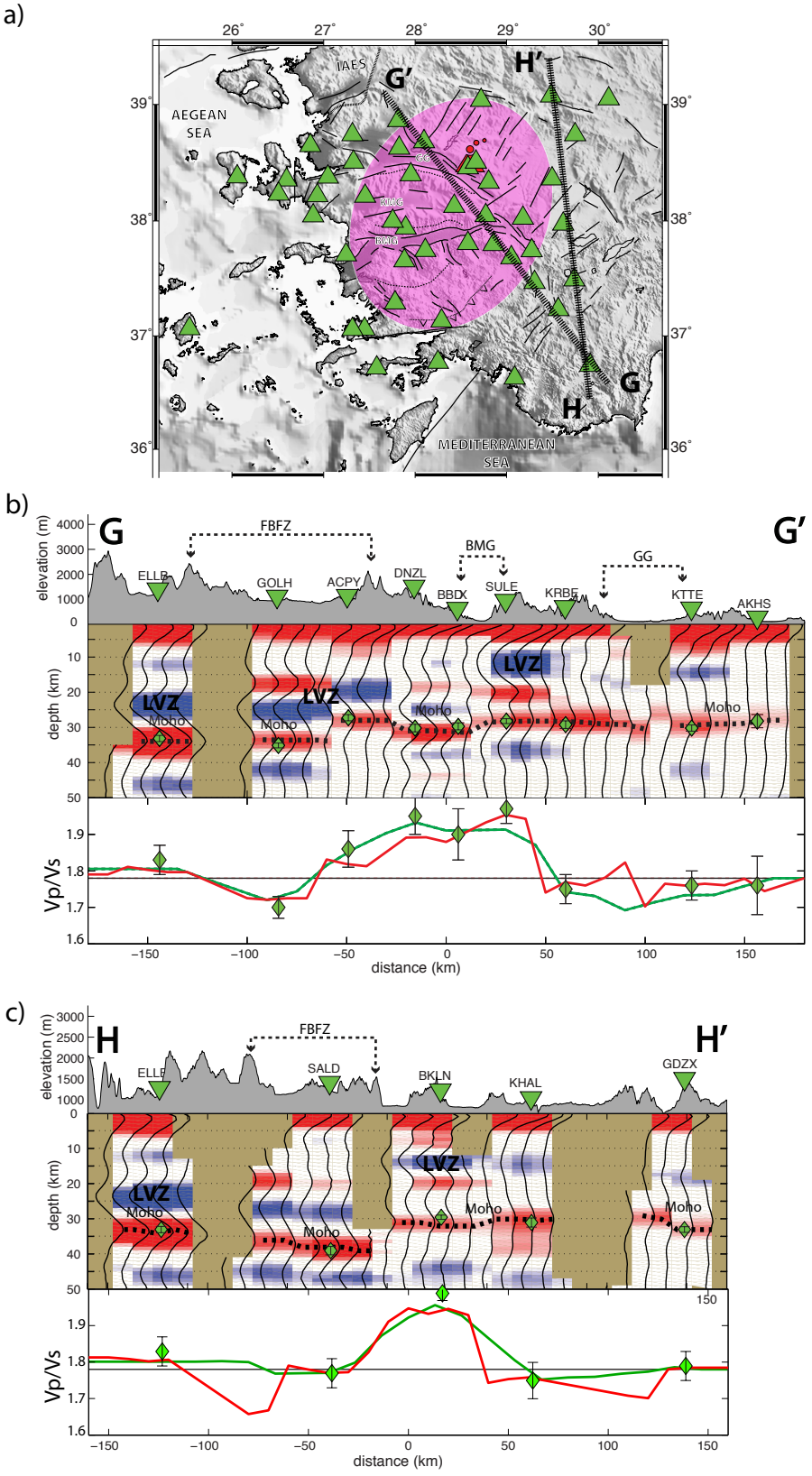

Figure 4.8. Representative SouthEast – NorthWest correct Vp/Vs Ps phase CCP stacks. G-G' and H-H' diagonally samples the FBFZ and MM (b and c). Correct (solid green line),

interpolated (solid red line) Vp/Vs and Vp/Vs results obtained from $H-\kappa$ solutions with error range (green diamonds with black solid error bars) plotted bottom of each cross section (b and c).

4.5.2.5. Results: Depth Slices of CCP to Map Low Velocity Zones beneath WA

Depth slices are created beneath entire WA with 2 km depth increment start from depth of 10 km and continue to 30 km. The top level of LVZs are imaged at 12 km depth Figure (4.9). The main sources of LVZs are located east and southeast edge of Menderes Massif. Those LVZs are also clear beneath the Buyuk Menderes Graben but they do not exist beneath MCC or quaternary volcanism (around KULA). Another small-scale low amplitude LVZs are located at north west of Menderes Massif and Gediz Graben. The LVZs is also well correlated with the thermal hotspots locations in WA.

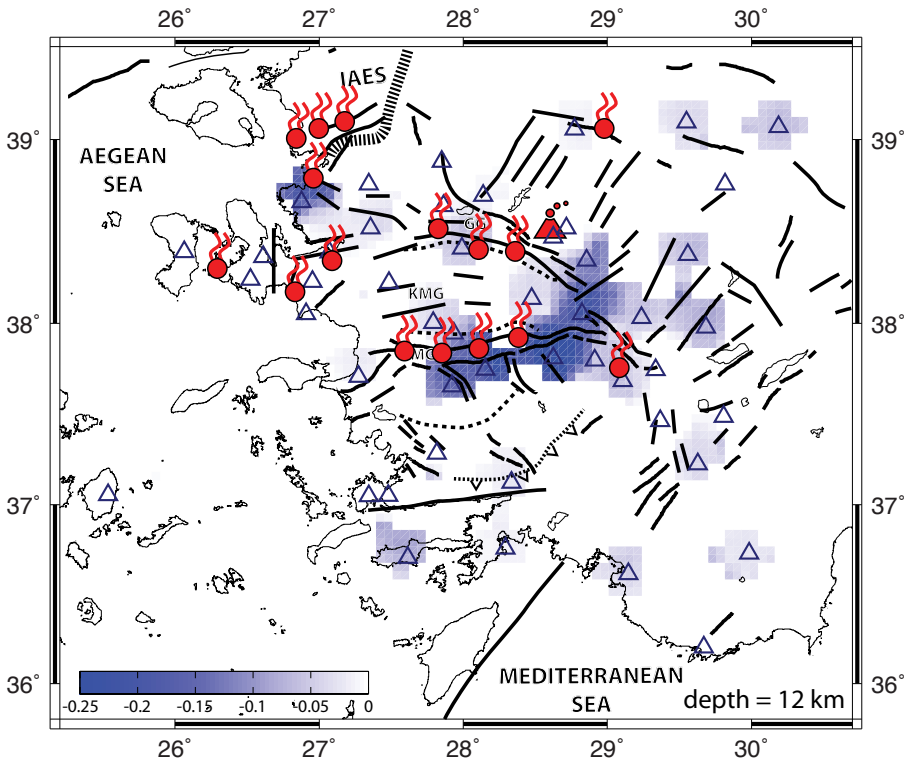

Figure 4.9. Low velocity zones (LVZ) at 12 km depth is showed beneath the grabens. Red circles with flames indicate major thermal hotspots within the region (Serpen et. al., 2008).

4.6. Discussion and Conclusion

The study area is known as a place of the active continental extension, which is a place of MCC, block rotation and rift development (Bozkurt and Mittwede, 2005; Koçyiğit, 2005). The P-RFs both H-κ and CCP cross-sections lead us to infer high resolved images of lateral changes along this extension regime, which is missing in other studies. The similar studies that has been done in the same region and surrounding areas before indicated that the average crustal thickness is between the ~27 km to ~30 km depth (Zhu et al., 2006; Karabulut et al., 2013). This result is supported by our CCP cross-sections, which can be sum up with ~28 km crustal thickness as an average.

The region can be defined as the smooth transition from thick to thin crust through east to west, respectively. Although the other researchers define this characteristic, it would be efficient to add that the crustal thickness has a possibility to present strong changes towards boundaries of WA. The crustal thickness varies between 33 - 35 km in the east and this crustal depth decreases down to 39 km in southeast because of the FBFZ. The center section is 29-32 km and the western part of the study region is 25 – 28 km (Fig. 4.5.a). The CCP profiles, also, support these characteristics. Vp/Vs does not present any dependence to orientation as Moho depth does (Fig. 4.5.b). However, high Vp/Vs values are localized at eastern boundary and northwest boundary of Menderes Massif (~1.90 – ~2.00). High Vp/Vs can possibly be a sign of a high heat flow, which provides support of partial melt presence in lower crust beneath these localized regions (Vanacore et al., 2013). This feature is, also, supported by higher heat flow level (300 mW/m^2) in WA than the world average of 110 mW/m^2 (İlkışık, 1995; Gürer et al., 2001). Other than the localized regions, Vp/Vs is low, especially, center section Menderes Massif where Vp/Vs are varying between ~1.65 to ~1.80.

Since WA is a well-known extensional region, calculating crustal stretching factor (b) can be useful to characterize the crust in terms of how much the crust effected by the extension force and specifically at which sections of crust extension affected most. McKenzie (1978) developed a simple model of lithosphere extension from analyzing geophysical and geological data for the Aegean region. He estimated that the Aegean lithosphere has been stretched by a factor of 2 since the late Miocene of 5 Myr ago.

However, the updated stretching factor calculations of Zhu et al., (2006) and Karabulut et al., (2013) present variations compare to McKenzie (1978). Their results show that the outside of MCC, in the Aegean region, the crust is stretched by factor of 1.1, this factor increases to 1.2 in Bornova Flysch Zone and 1.5 in Menderes Massif. The stretching factor is calculated by a factor of 1.4 in the Cycladic Massif and 1.9 in Rhodos Island. The stretching factor observation is supported by our result, which shows increase in stretching to south of study region as an expression crustal thinning compare to northern section.

CCP profiles indicate almost no Moho topography in E-W directions and small variations in N-S profiles. The flat Moho suggest that the lower crust is so weak that it can flow laterally on a short timescale to smooth the Moho topography induced by extension. The efficient lower crustal flow, also, supported by simplified model of McKenzie (2000). The simplified model of McKenzie claims a fluid layer over a half-space. According to his model, the lower crustal viscosity in the Aegean is at least 3 times larger than in the Basin and Range. A strong Aegean lower crust is consistent with GPS results that show most of the Aegean moves as a group of near-rigid blocks (McClusky et al., 2000; Nyst and Thatcher, 2004).

CCP results images LVZs, possibly include partial melt material, changing with dept, varying from upper crust (~10 km) to lower crustal depths (~20 km). They are mainly focused beneath graben formations and southeastern corner of region. The effective depth is found at ~12 km depth (Fig. 4.9) which is well correlated with major thermal hotspots (Serpen et. al., 2008) in the region. This effective depth can possibly be seen as a main heat source of thermal hotspots.

CCP cross-section Fig. (4.8) presents the most intrinsic features beneath the eastern boundary of Menderes Massif. Lower crust is observed at depth of ~20 km on cross-section, which is absent or very limited beneath the Menderes Massif, possibly due to lower crustal flow. Furthermore, a continuous Moho is observed at depth of ~30 km at the center of the profile, where the Vp/Vs is highest. The LVZ is supported by stable positive phases (~39 km close to center and depth of 35 km south end of profile) constantly route to south, making a ~8 km depth difference before the FBFZ and beneath the FBFZ. By taking into consideration of Moho difference, FBFZ can possibly depress the Moho and decreases

down to upper mantle depths in the mean of on shore continuation of STEP faulting of Hellenic subduction (Wortel and Spakman, 2000). FBFZ is supposed a combination of small scale fault zones from its surface observation and maximum depth of faulting limited in top ~20 km seismic zone before any evidence of images at upper mantle depths.

5. IMAGING CRUST AND UPPER MANTLE OF ISPARTA ANGLE FROM P AND S RECEVIER FUNCTION ANALYSIS

5.1. Introduction and Tectonic Settings

Isparta Angle (IA) presents complex regime between westward moving Central Anatolia (CA) and N-S extending Western Anatolia (WA) in southwestern Turkey. The region is shaped by two prominent plate boundaries, Hellenic (in the west) and Cyprus (in the east) arcs. These are created by convergence of African and Eurasian plates in offshore. The arcs are evolved from northward subduction of oceanic African lithosphere beneath Aegean and Anatolia. Hellenic arc (or Aegean Trench) extends from the Peloponnesos as a northwest corner to the island of Crete in the south. Paleomagnetic data suggests that Hellenic arc showed a rectilinear shape before mid-Miocene and since then it has formed as a southward arc (Kissel and Laj, 1988; Kissel et al., 1993). Seismic tomographic models indicate continuous (undetached), more than 1500 km long slab with high dip angle, reaching down to lower mantle depths beneath the Aegean (Bijwaard et al. 1998; Wortel and Spakman 2000; Piromallo and Morelli 2003). The steep dip angle of Hellenic slab is believed to create retreating nature of the slab and thus it is responsible of back-arc extension (arc parallel extension) of Aegean and WA.

Cyprus arc extends from south of Cyprus Island toward northwest to Anaximander seamount, which is located southwestern of IA. Subduction of Cyprus Slab does not clear south of Cyprus, which suggests that the subduction is stopped by the Eratosthenes seamount (Glover and Robertson, 1998). Other than this truncation, P wave tomographic images of Biryol et al., (2010) indicates that Cyprus slab steeply dips down to depths of 60-200 km beneath Anatolia. Cyprus slab begins to dipping toward northward with a angle of ~45^0 in the depths of 200-400 km then, the slab is flatten out, suggesting that it lies flat on the 660 km mantle transition zone.

The sharp cusp between the Hellenic and Cyprus trenches (Fig. 5.1) and the significant differences in the convergence velocities of the African lithosphere at these trenches are likely to have resulted in a lithospheric tear in the down going African plate

that allows the asthenospheric mantle to rise beneath SW Anatolia (Doglioni et al. 2002; Agostini et al. 2007; Dilek & Altunkaynak 2008). This assumption is analogous to lithospheric tearing at Subduction-Transform Edge Propagator (STEP) faults described by Govers &Wortel (2005)

The regional geodetic velocity field observations indicate that Arabia, Aegean/Peloponnesus and Anatolia rotate counter clockwise (CCW) rotation with respect to Eurasia (Reilinger et al., 2006). Specifically; for the Anatolia, GPS residual velocities present <2 mm /yr. internal deformation with ~20 mm/yr westward motion of CA that is accompanied by ~1500 km long dextral NAFZ. The westward motion turns to 10-15 mm/yr N-S extension in WA, which shapes E-W oriented graben formation by normal faulting with dominant E-W strike. GPS velocities increase up to ~30 mm/yr toward southwest to Hellenic arc. The increment in the velocities is thought to be pulling effect of down going African lithosphere where it creates the westward motion of CA and N-S extension of WA (McClusky et al., 2000). Within this tectonic mobility, kinematic models of Tiryakioğlu et al., (2013) present 10 mm/yr movement of IA respectively to Anatolia. S-SW movement along western limb is marked by FBFZ with increasing velocities toward SW. ~2-5 mm/yr S-SE movement along eastern limb of IA is bounded by AKSFZ. The relative motions of western and eastern limbs promote the extension in the inner part of IA and as whole counter clock-wise (CCW) rotation similar to Anatolia but superimposed on regional scale CCW rotation of Anatolia.

Menderes Massif presents a significant geologic unit located in surroundings of IA and it is placed in the northwest of IA. It is not going to be added further information about the Massif in terms of evaluation or source of rock units since it is explained in detail in Chapter 4 (section 4.2).

The Anatolide-Tauride block is defined by E-W oriented ophiolite belt with numerous tectonic slices at south of İzmir-Ankara-Erzincan Suture Zone (IAESZ). The mixed signs of numerous tectonic slices indicate the closure and destruction of Neotethys (Stampfli 2000). Taurides are consisted of Precambrian and Cambro–Ordovician to lower Cretaceous carbonate rocks intercalated with volcano-sedimentary and epiclastic rocks (Ricou et al. 1975; Demirtasli et al. 1984; Özgül 1984; Gürsu et al. 2004). These rocks are

tectonically overlained by Tethyan ophiolites along south-directed thrust sheets (Dilek et al. 1999a; Collins & Robertson 2003; Çelik & Chiaradia 2008; Elitok & Drüppel 2008). The importance of Taurides for the IA is that they assemble different geologic units between the edges of western Taurides (Lycian nappes) and central Tauride (ophiolitid belt of Anatolia-Tauride block). The western Taurides are composed of Lycian, Hoyran–Beyşehir–Hadim and Antalya allochthons. The central Taurides includes Anams-Akseki autochthons from the Latest Cretaceous to the Late Pliocene. Their origin related with Cretaceous oceanic crust which is derived from IAESZ and then, they have been moved to south as a result of tectonic uplift and erosion associated with exhumation of the Menderes core complex during the late Cenozoic (Collins & Robertson 2003; Ring & Layer 2003; Thomson & Ring 2006; Dilek and Altunkaynak 2007).

Fethiye Burdur Fault Zone (FBFZ) and Sultan Dağ Fault (SF) shape surface boundaries of IA on-shore. FBFZ is ~300 long and ~50 km wide NE-SW directed left-lateral transtensional boundary between the IA and extension dominated back-arc region of Hellenic arc in the west. FBFZ is, also, defined as a component of the NE directed Subduction Transform Edge Propagator (STEP) faulting on shore. STEP faulting is evaluated east of Hellenic trench which continues to NE into Plint-Strabo STEP faults and merges with Rodos basin off shore (Özbakır et al., 2013; Hall et al., 2014). Govers and Wortel (2005) suggest that the STEP faulting is related with the slab tear. However, it is mostly promoted that the difference in the convergence velocities of African lithosphere at Hellenic and Cyprus trenches are responsible of slab tear. SF is NW-SE directed transtensional boundary between the IA and CA in the east. The moment tensor solution of moderate size earthquakes (6.0 Sultandağ 2000 and 6.5 Çay 2002 earthquakes) states oblique-slip normal faulting along the deformation zone. The normal fault movements cut and down throw an older paleotectonic structure, called Sultandağ thrust (Taymaz and Tan 2001; Taymaz et al., 2002; Koçyigit and Özacar 2003).

IA and WA have been exposed to various type of magmatism that have been described difference in both magmatism source and exhumed deep material to surface (e.g. magmatism source related with subduction or asthenospheric mantle flow and exhumed material rich with calc-alkaline or alkaline). Surface rock and related landscape formation studies are revealed that magmatism and exhumation are sourced from

volcanism and they are completed during Cenezoic (Dilek and Altunkaynak 2009). The major eruption centers during the late Miocene-Pliocene to Quaternary are located in Kula (NW of IA), Afyon, Isparta-Gölcük, Kırka (N of IA). KULA magmatism is related with alkaline volcanism that is composed of basalts, basanites, and phonotephrites with potassic to ultrapotassic compositions at the surface (Richardson and Bunbury 1996; Seyitoğlu et al. 1997; Aldanmaz et al. 2000; Alici et al. 2002; Savasçin & Oyman 1998; Francalanci et al. 2000; Innocenti et al. 2005). Geochemical expression of this alkaline volcanism is associated with rapid upwelling of asthenosphere beneath western Anatolia (Gülen 1990; Toçkaer et al., 2005). Afyon, Isparta-Gölçük and Kırka volcanic fields are similar to KULA. Their geochemical expression show alkaline volcanism that is produced potassic-ultrapotassic rocks (tephriphonolite, trachyandesite, andesite) with olivine, plagioclase, clinopyroxene, biotite, amphibole and phlogopite phenocryst phases (Alici et al. 1998; Çoban & Flower 2006; Kumral et al. 2006). Afyon, Isparta-Gölçük and Kırka volcanic fields indicate subduction related magma contamination with low crustal contamination (Alici et al. 1998; Çoban & Flower 2006; Kumral et al. 2006). The ages of surface rocks indicate a younging pattern from pattern from N to S (from middle-late Miocene ~17 Ma to Pliocene ~4 Ma) on the volcanic fields. Migration of youthful exhumation to South is associated with propagation of the tear between Cyprus and Hellenic slabs (Savasçin & Oyman 1998; Dilek and Altunkaynak 2009).

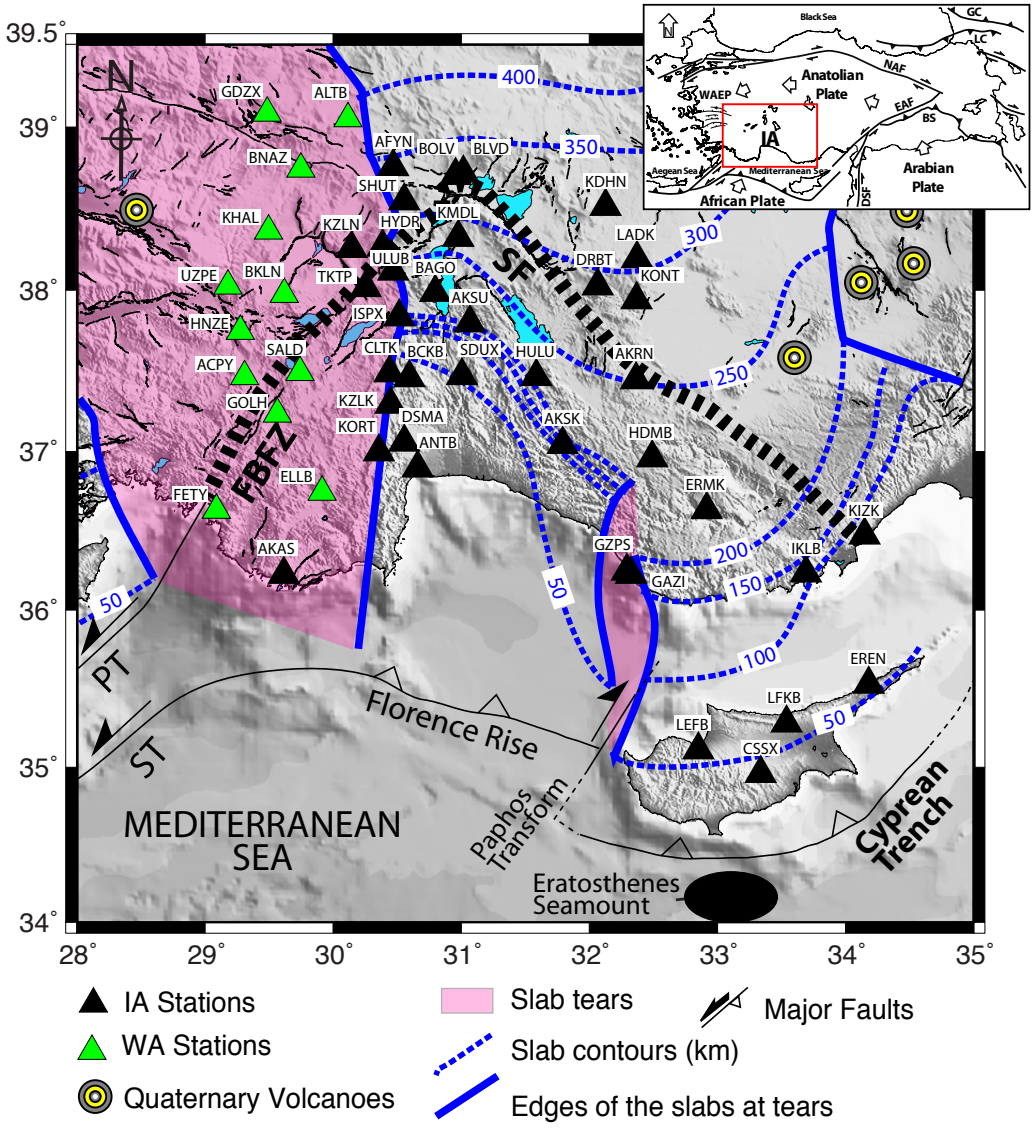

Figure 5.1. Station locations are plotted on the topography (elevation is ascending from dark to light color on off-shore and bathymetry is descending from light to dark color on shore) of both on Isparta Angle (IA, black triangles) and Western Anatolia stations (WA, light-green triangles plotted on suggested slab tears and contours (Biryol et al., 2011) in the region. IA and surrounding active faults have showed by thick-dashed black lines and solid red lines respectively (Barka & Relienger 1997; Bozkurt 2001; Emre et al., 2013). FBFZ, Fethiye-Burdur Fault Zone; SF, Sultandağ Fault; ST, Strabo Transform; PT, Pliny Transform.

5.2 Previous Geophysical Studies

IA and surrounding regions (e.g. WA or CA) are subjected to many geophysical studies from surface to upper mantle. Travel time tomographic images of Bijward et al., (1998), Piromallo and Morelli (2003) and Biryol et al., (2011) define the subducting Hellenic and Cyprus slabs beneath Aegean and Anatolia. Biryol et al., (2011) proposes a major slab tear between Hellenic and Cyprus slabs. According to his tear image, it is mostly located beneath WA and partially western limb of IA which is ~300 km wide and is evindenced by slow velocity perturbations. He, also, suggests a minor tear that is located at SE of IA where this minor tear is correlated with Paphos transform with intermediate depth seismicity.

Shear wave splitting study of Şapaş and Boztepe-Güney (2009) proposes that the fast polarization directions are mainly NE-SW direction ($560 \leq \phi \leq 2050$) and the delay time between the fast and slow components varies between 0.37 to 4.0 s depending on back-azimuth. The reason of this mantle complexity is explained by a laterally varying anisotropy. The variation in anisotropy is related with dipping axis of symmetry other than horizontal symmetry axis, different forms of symmetry other than hexagonal, the effect of incidence angle or multiple layers of anisotropic media with different symmetry axes. Thus, they propose two layer anisotropic model with a horizontal symmetry axis beneath ISP station that is confirmed by their forward model tests. The first layer of anisotropy occurs in the upper mantle $\phi u = 1500$ with 1.6 s delay time and the second one is due to the asthenospheric flow $\phi l = 400$ with 1.0 s delay time. However, shear-wave anisotropy results of Paul et al., (2014) states NE-SW oriented fast polarization directions beneath most of the Anatolia and northern Aegean Sea with highest and lowest delay time, 1.5 ± 0.4 s and 0.6 ± 0.4 s respectively. The fast polarization directions have steady in counterclockwise rotation of 10 per longitude from east Anatolia to northern Aegean. They indicate an exception in SW corner of Anatolia where IA is located as well as where the fast polarization directions are NW-SE with average delay time is 1.3 ± 0.4 s. They explain NE-SW fast polarization with large-scale mantle flow driven by the African swell and the swell combines with the regional scale flow driven by the suction from the Hellenic slab, a high-density anomaly, which is probably augmented by trench-normal flow due to slab rollback. Additionally, the NW-SE polarization orientation is explained by toroidal flow

through the slab window beneath southwestern Anatolia.

Regional Pn tomography of Al-Lazki et al., (2004) on Turkey and adjacent regions presents broad scale (~500 km) low Pn velocity zones (< 8 km/s) underlie the Anatolian plate and more specifically, smaller scale (~200 km) very low Pn velocities (< 7.8 km/s) are evidenced beneath IA and CA. The reason of low Pn velocity is interpreted as hot and unstable mantle lid zones. A recent Pn study of Kömeç and Karabulut (2011) presents location of two fast Pn velocities (> 8.2 km/s) beginning from the west of Cyprus and extends from the Paphos discontinuity to IA in the N–S direction with decreasing intensity. Further to west, a more pronounced high velocity zone (> 8.4 km/s) on the south of the Rhodes Island is observed. Additionally, low Pn velocity zones (< 7.8 km/s) are located between the Rodhos Islands and the Antalya Bay. High and low velocity anomalies are an indication of heterogeneous lithospheric structure, which is spatially correlated with Hellenic, Cyprus, slabs and suggested slab tear between those arcs Biryol et al., (2011).

Regional shear wave velocities for Turkey and surroundings are obtained by the inversion of fundamental mode Rayleigh wave (Salaün et al., 2012 and Delph et al., 2015). Southwestern Anatolia and IA have negative phase velocity perturbations for the periods up to 30 s and the shear velocity abruptly slow, down to 25 km (~3.15 km/s) in the western limb of the IA. The low shear wave characteristic continues for higher periods up to 150 s where the shear wave velocities (~4.2 km/s) are 4.5-5 percent lower comparably to ak135 global velocity model between the depths of 125 to 175 km. The reasons of these low velocities are interpreted as the introduction of aqueous fluids related to the under-plating of accretionary material from the under-thrusting of a buoyant, attenuated continental fragment similar to the Eratosthenes seamount or asthenospheric mantle material rising inside a vertical slab tear between Hellenic and Cyprus arcs. (Delph et al., 2015). Love wave group velocity maps in the period of 10–50 s are computed using a tomographic inversion method by Cambaz and Karabulut (2010). The existence of low group velocities is mapped beneath Antalya bay. They elongate toward IA where low velocities start to appear at 10 s and continue to be present at 40 s with increasing wavelengths. Menderes Massif and Sultandağ-Beyşehir Massif border low velocities in NW and E, respectively. The group velocities are comparably higher after these boundaries.

5.3. Receiver Function Data and Computation

The data is collected by the combination of closely spaced (~35 km) temporary and permanent seismic stations from networks that are located in the region. Temporary network is established in the scope of Isparta Angle Passive Network project which is a collaborative work of Bogaziçi University Kandilli Observatory and Earthquake Research Institute (BU-KOERI)/Department of Geophysics, University of Missouri – Columbia (MU) and Süleyman Demirel University (SDU)/Geophysical Engineering Department. The aim of the project is to study crust and upper mantle structures beneath IA. N-S and E-W 2D line-shaped temporary network is built up in two stages. The first stage is consisted of 7 Nanometrics Trillium 120 s. sensors with Taurus digitisers and 3 Guralp CMG-3T sensors with Reftek-130 digitisers which were run in the dates of August 2006 to August 2007 and the second one is included 7 Guralp CMG-6TD and 2 Guralp CMG-3TD instruments which were operated between March 2007 to November 2009. In addition to this temporary network, permanent stations operated by BU-KOERI/National Earthquake Monitoring Center, Disaster and Emergency Management Presidency of Turkey/Earthquake Research Department (DEMP/ERD) and IRIS/GEOFON network are incorporated with the data period beginning from August 2006 to January 2011 to make more dense sensor spacing on 2D profiles and sample entire IA and surroundings.

In this chapter, P and S receiver methods (see Section 2.1 and Section 2.2 for details) are applied to temporary and permanent networks in IA. The same procedure is followed in terms of P receiver function calculation and evaluation as stated in Chapter 4.

S receiver functions (S-RFs) have different criteria than P receiver functions. Soö teleseismic S waves are selected considering the limitations in Section (2.2). The limitations states that source points of teleseismic events are located at angular distances of 55^0 to 85^0 and their depths are < 300 km and with mb ≥ 5.5. By taking into these limitations, totally, 946 event are identified from the National Earthquake Information Center (NEIC) within the maximum period of available continuous data which is August 2006 to January 2011 (Fig. 2.4.c). Teleseismic S wave components are manually picked and windowed (Z, N-S and E-W) in 95 s time window which starts at 70 s before the onset of S phase and continue 25 s after. Component rotation is needed in order to enhance

converted wave energy (here in S-to-P) and minimizing S wave energy on P components. Thus, coordinate systems (Z, N-S and E-W) are rotated to ray based coordinate system (P, SV and SH) in which each wave type are presented on its own particle motion direction. Firstly, Z, R and T components are obtained by using theoretical back azimuth angle. Secondly, coordinate rotation is applied to Z and R using Kennet (1991) method that corrects free surface for assumed slowness and calculated azimuth values to obtain P (or L) and SV (or Q) components (see Section 2.3 for details).

S-RFs present 2D migrated depth images of discontinuities down to 200 km in IA. Regularized Kirchhoff migration method (e.g. Wison and Aster, 2005) (see Section 2.8.2) is used to create cross-section images. Originally the method migrate converted P-to-S and multiple phases (PpPs and PpSs+PsPs) into their origin where the conversion occurs (Dellingeret et al., 2000; Wilson and Aster, 2003). S-to-P conversion resolve mainly lithospheric-asthenospheric and partially Moho depths since S-RFs are recorded in low frequency. N-S, E-W and diagonal migrated profiles are created by using constant velocity down to 200 km where Vp = 6.2 km/s and Vs = 3.58 km/s with 10 km bin interval.

5.4 Results and Discussion

5.4.1. P Receiver Function Results and Discussion

5.4.1.1. $H - \kappa$ Stacking

H-κ solutions show that depth and Vp/Vs of crust quite varies in the IA and surrounding regions. There is no sign of dependency to any direction in terms of thinning or vice versa. To start with, the cusp of IA, where Sultan Dag fault and NE tip of FBFZ meet, ~35 to ~37 km crustal thickness and low Vp/Vs values ~1.70 to ~1.80 are observed. To continue with just south of IA cusp, respectively, shallow crust is calculated between ~32 to 34 km and ~1.85 to ~1.90 Vp/Vs are figured out. The unresolved stations (the black triangles) limit to resolve crustal thinning or thickening towards study center. The transition from strong extension is placed in the western limb of IA. This is indicated by the thinner to thicker crust from ~29 – 31 km to ~35 to 37 km and low to high Vp/Vs in IA comparably to extension dominated WA. Further to southwest, on FBFZ, the crust

thickness is ~39 km and; after 37^{o} latitude to south crust gets thinner specifically beneath the stations located close to coast. Low Vp/Vs presents east trend that vary between ~1.60 to ~1.80. The center-west of IA has a thick crust which is in a depth of ~38 – 40 km while the center-east of IA has a thin crust which is in depth ~28 – 34 km. To continue with the eastern limb, the crust gets thicker on south-east which has an ~41 to ~46 km depth. However, it is observed a clear separation of thinner crust and higher Vp/Vs beneath stations close to coast. Other than the IA, crustal thickness is quite different in east and west of Cyprus. The crustal values are ~35 – 37 km in the east, ~32 – 34 km beneath center and ~23 – 25 km beneath the west. The west of Cyprus presents high Vp/Vs values that are more than 1.85 (Fig. 5.4.a and 5.4.b).

Subduction phases are defined in a few stations except from crustal phases in P-RFs waveform. These phases can reveal depth and Vp/Vs of down going African slab in IA crust, which is well imaged teleseismic tomographic methods. One of these exceptional stations is located in the south of IA and the other two are located in Cyprus. The depth of subduction is calculated ~46 km with ~1.67 Vp/Vs south of IA and ~43 - ~45 km with high Vp/Vs ~1.90 or higher beneath Cyprus (Fig. 5.4.a and 5.4.b).

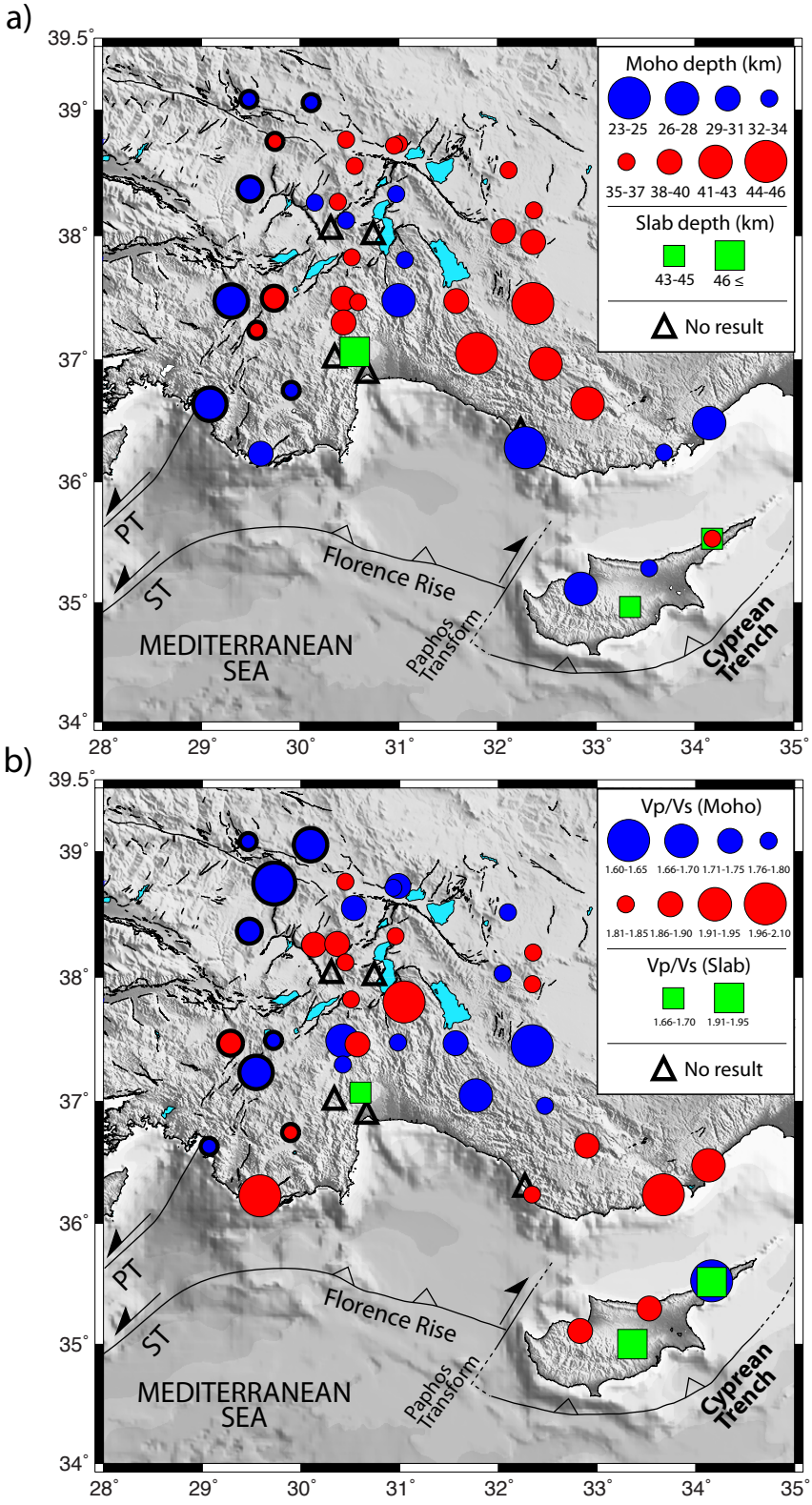

Figure 5.2. Moho depth and Vp/Vs change on topographic map of Isparta Angle (IA). Black-thick edged red and blue circles present the calculated solutions at WA study (Chapter 4, Fig. 4.4) Green squares shows the possible slab depth and related Vp/Vs at

those stations. Unfilled triangle presents station locations whose have no proper H-K results due to limited number of RFs and complex converted arrivals. a) Moho depth is defined with different size of circles; red means thicker and blue means thinner crust. b) Average crustal Vp/Vs is showed, low Vp/Vs are blue and higher Vp/Vs are red circles.

5.4.1.2. A-A' CCP Profile

The N-S CCP cross-section (Fig. 5.3.c) samples the center of IA. Moho topography is almost flat and its depth is around ~35 km depth beneath this cross-section. Moho phases begin from cusp of IA and continue to 140 km lateral distance to south. Moho phases are still observable down to south but they are in faded color close to southern end of cross-section. The faded Moho trend is an indication of loosing amplitudes of P to S conversion at the south of IA. The dominant phases are possibly resulted cause of African subducting slab, which are clearly observed at the depth of ~47 km in southern most ends. Mid-crustal depths (between ~10 to ~15 km), the phases begin with negative at the north and turns to positive at +80 km lateral distance continue south to +20 km lateral distance, and again turns to negative down to south until the end of profile. There is no sign of lower crustal structure in the north. However, a similar characteristic as mid-crustal depths is observed at ~25 km depth where negative phases begin at +50 km lateral distance and they turns to positive between 0 to -50 km (a possible lower crustal structure) lateral distance. These positive phases turn to negative until south end of profile after -50 km lateral distance. The property of flipping amplitudes from negative to positive or vice versa can be interpreted as a sign of possible strong anisotropic variations within upper and lower crust.

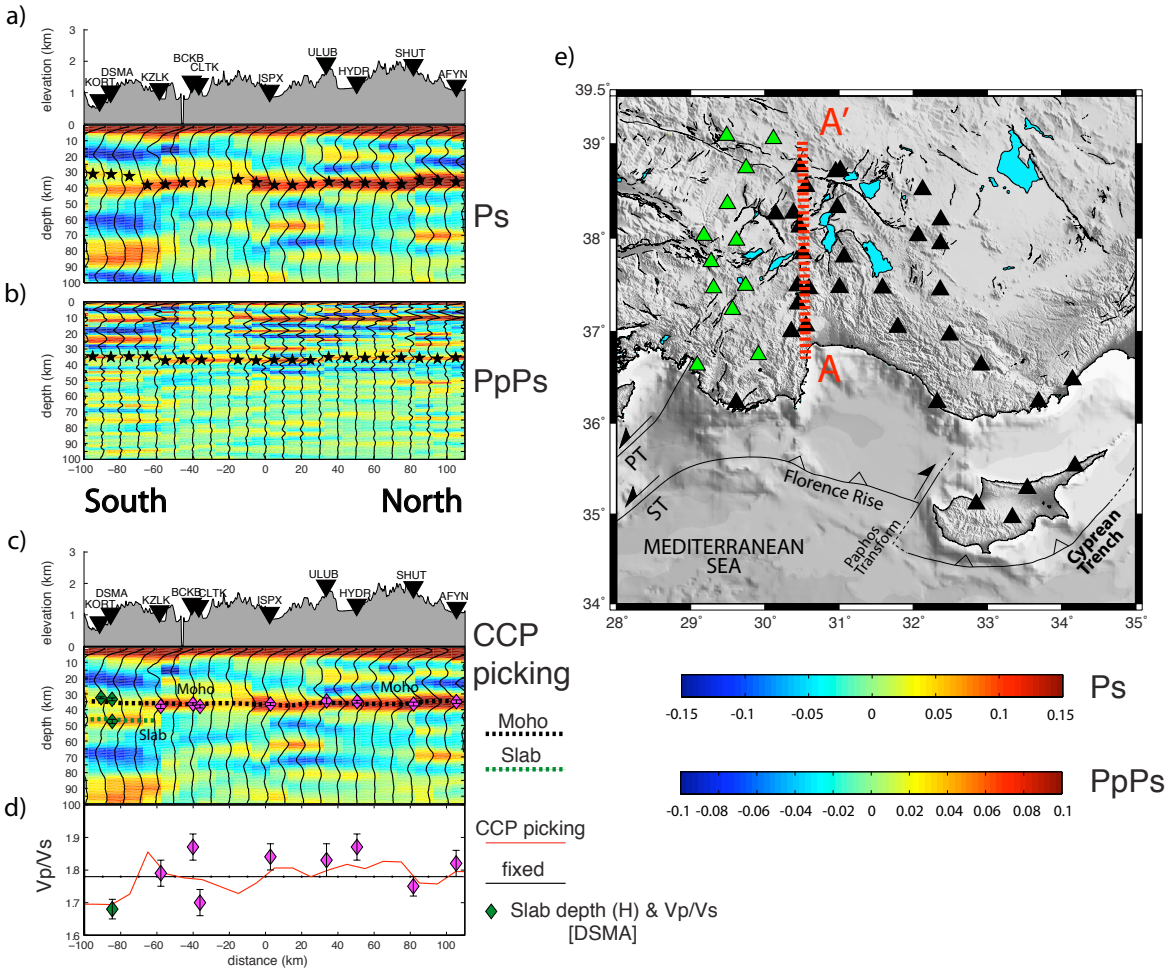

Figure 5.3. North-South oriented 10 km bin-interval and 20 km bin-size profile. Calculation of correct Vp/Vs and true Moho depth using CCP cross-sections is on the left hand-side and location of the profile on topographic map is on right hand-side. Ps and PpPs phase CCP stacks for constant Vp/Vs (1.78) with observed and picked Moho (black-stars) discontinuity (a-b). c) Ps phase CCP stack for calculated correct Vp/Vs with H-K solution depths and depth error bars (magenta diamonds for Moho, green diamonds for Slab with solid black error bar). Moho is presented with the black-thick dash line and Slab is showed by green-thick dash line. d) Correct Vp/Vs variation along the profile and average constant Vp/Vs are showed by solid red and black line respectively. Vp/Vs values with error range are plotted with magenta diamonds for Moho and green diamonds for Slab with black error bar on it.

5.4.1.3. B-B' CCP Profile

The E-W oriented CCP cross-section (Fig. 5.4.c) indicates Moho topography as passing through FBFZ in west (western limb of IA), center of IA and eastern limb of IA. Moho step is clearly observed at the distance -70 km in the west, where the Moho depth suddenly decreases down to ~40 km from ~30 km depth. To continue to center of IA, Moho is detected at ~35 km depth and it gets its shallowest value, ~30 km depth beneath SDUX station where the eastern limb of IA begins. The Moho gradually dips to east until the depth of ~40 km beneath the eastern limb. Mid and lower crustal contamination have tendency to anisotropic feature above the Moho. The anisotropic feature is observed at starting from west around depth of ~20 km. The negative signals (possibly a low velocity zone) turns to positive at eastern end of FBFZ, where the positive phases situate as lower crustal layer above the Moho. Another, important mid-crustal velocity contrast is observed at ~15 km depth that is started beneath the western part of the cross section. The positive amplitudes turn to negative ~-10 km lateral distance and increase their depth toward east down to ~20 km where clear negative amplitudes are located at +50 to +140 km lateral distance.

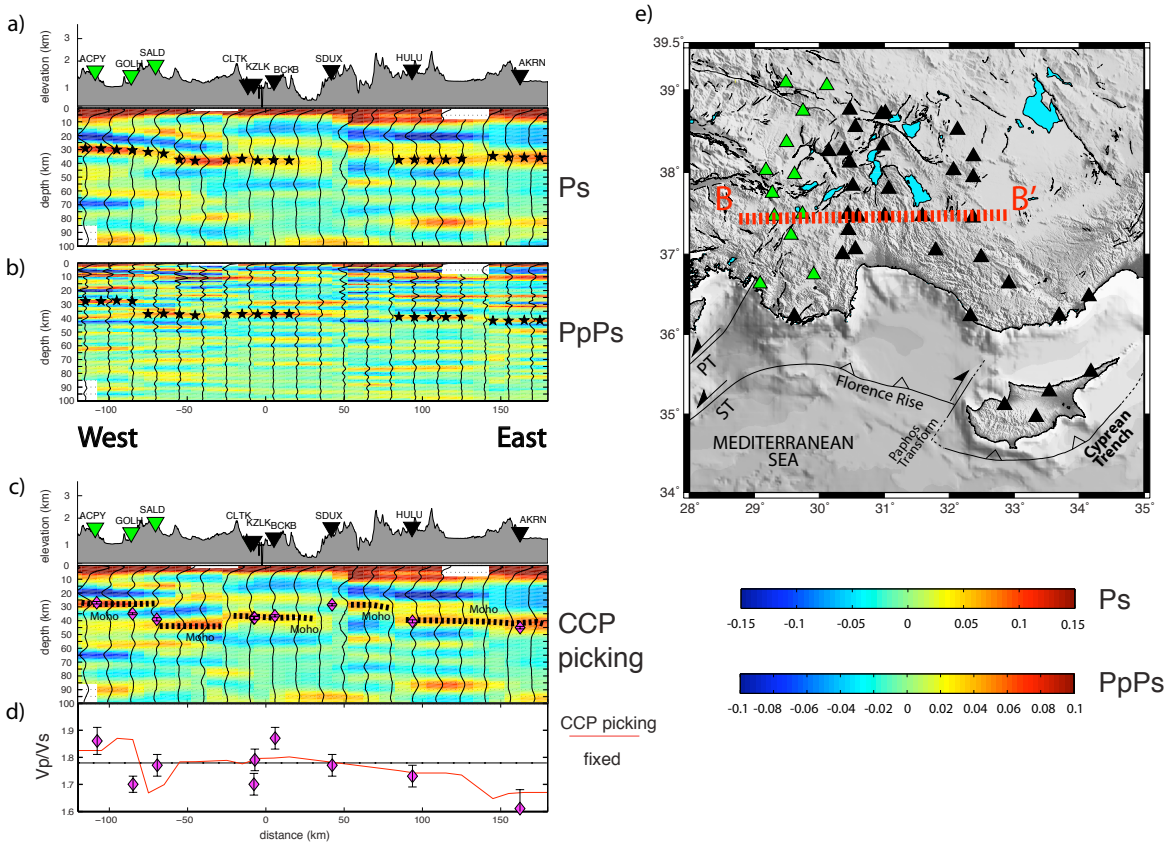

Figure 5.4. East-West oriented 15 km bin-interval and 30 km bin-size profile. Calculation of correct Vp/Vs and true Moho depth using CCP cross-sections is on the left hand-side and location of the profile on topographic map is on right hand-side. Ps and PpPs phase CCP stacks for constant Vp/Vs (1.78) with observed and picked Moho (black-stars) discontinuity (a-b). c) Ps phase CCP stack for calculated correct Vp/Vs with H-K solution depths and depth error bars (magenta diamonds for Moho, green diamonds for Slab with solid black error bar). Moho is presented with the black-thick dash line and Slab is showed by green-thick dash line. d) Correct Vp/Vs variation along the profile and average constant Vp/Vs are showed by solid red and black line respectively. Vp/Vs values with error range are plotted with magenta diamonds for Moho and green diamonds for Slab with black error bar on it.

5.4.1.4. C-C' CCP Profile

The NW-SE cross-section (Fig. 5.5.c) is the longest profile that begins from northwest corner of WA to NE tip of Cyprus Island. The profile presents flat shape Moho

which gently dips from ~30 km depth at NW down to ~40 km to SE around -180 km lateral distance. Then, Moho depth is elevated to ~35 km at SE end of on shore. Moho beneath Cyprus Island is ~32 km but the difference between eastern and western part of Cyprus is quite high as shown by H-κ results. Strong negative phases are observed at the depth of 45 km. The proposed subduction phases are identified at ~65 km depth. Other than the Moho, a limited range of upper crustal structures at ~10 km are defined beneath HULU, SDUX and AKSU station at center and BNAZ, GDZX station at NW tip of cross-section. Localized negative phases are defined at mid-crust in the NW and in the lower crust to in SE.

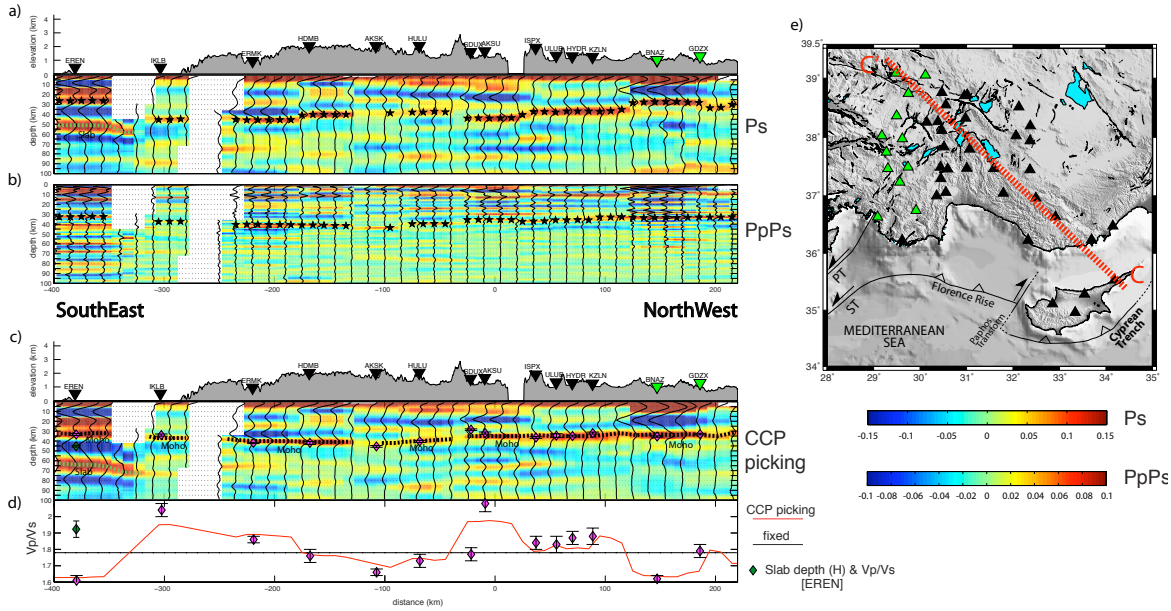

Figure 5.5. NorthWest-SouthEast oriented 15 km bin-interval and 30 km bin-size profile. Calculation of correct Vp/Vs and true Moho depth using CCP cross-sections is on the left hand-side and location of the profile on topographic map is on right hand-side. Ps and PpPs phase CCP stacks for constant Vp/Vs (1.78) with observed and picked Moho (black-stars) discontinuity (a-b). c) Ps phase CCP stack for calculated correct Vp/Vs with H-K solution depths and depth error bars (magenta diamonds for Moho, green diamonds for Slab with solid black error bar). Moho is presented with the black-thick dash line and Slab is showed by green-thick dash line. d) Correct Vp/Vs variation along the profile and average constant Vp/Vs are showed by solid red and black line respectively. Vp/Vs values with error range are plotted with magenta diamonds for Moho and green diamonds for Slab with black error

bar on it.

5.4.2. S Receiver Function Results and Discussion

5.4.2.1. A-A' Kirchhoff Profile

S-RFs cross-sections (Fig. 5.6 to 5.8) are created down to 200 km depth. So, primarily LAB and partially Moho phases are defined in that depth range. To start with Moho, S-RFs cross-sections show rough Moho that varies in the depths of ~30 km to ~40 km. The African slab related phases are visible at southern most end, Fig. (5.6). This rough Moho depth and slab related phases are well correlated with the actual results of Moho calculations from P-RFs (pink diamonds) but there is not enough resolution to evaluate any kind of thinning or thickening along the cross-section. Moho signals have low resolution in S-RFs cross-sections compare to P-RFs since S-RFs are relatively long period waveforms compare to P-RFs, thus, P-RFs are more effective to calculate Moho. However, the compatible depth of Moho signals that are calculated from S-RFs with true Moho depth which are calculated with P-RFs as an indication of producing high quality S-RFs in the process.

S-RFs cross-sections reveal a clear LAB boundary beneath entire region of IA. The N-S cross-section (Fig. 5.6) indicates a difference in LAB which starts at the depth of ~60 to ~90 km in the northern part. LAB is in a form of shallower beneath African Slab related phases at the south end of cross-section. LAB is imaged at depth of 50 km to 80 km at this end. There are no clear LAB phases between these two northern and southern ends.

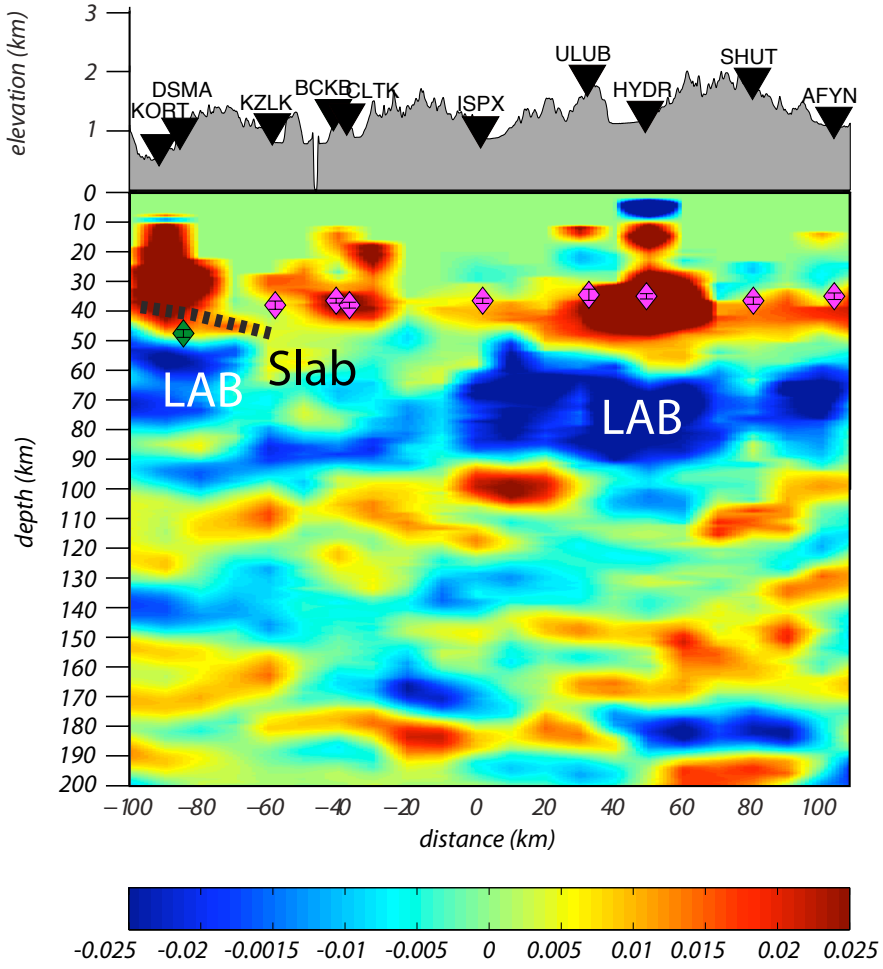

Figure 5.6. N-S S receiver function profile (see Fig. 5.3.e for location of profile). Diamonds presents Moho and Slab depths along the profile obtained from H-K solutions on the station (Pink diamonds for Moho, dark green for Slab).

5.4.2.2. B-B' Kirchhoff Profile

The E-W cross-section (Fig. 5.7) presents similar characteristic of LAB boundary in which the LAB zone is located at depths of ~55 to 80 km beneath the eastern section. There is a clear difference in LAB from east to west where the difference starts at FBFZ. At this point, a faded LAB phases continue to west at the depth of ~70 km but beneath these faded phases, there are strong positive arrivals at depth of ~85 km and negative arrivals at depth of ~100 km. It is clear that LAB is deeper at western section of the cross-section.

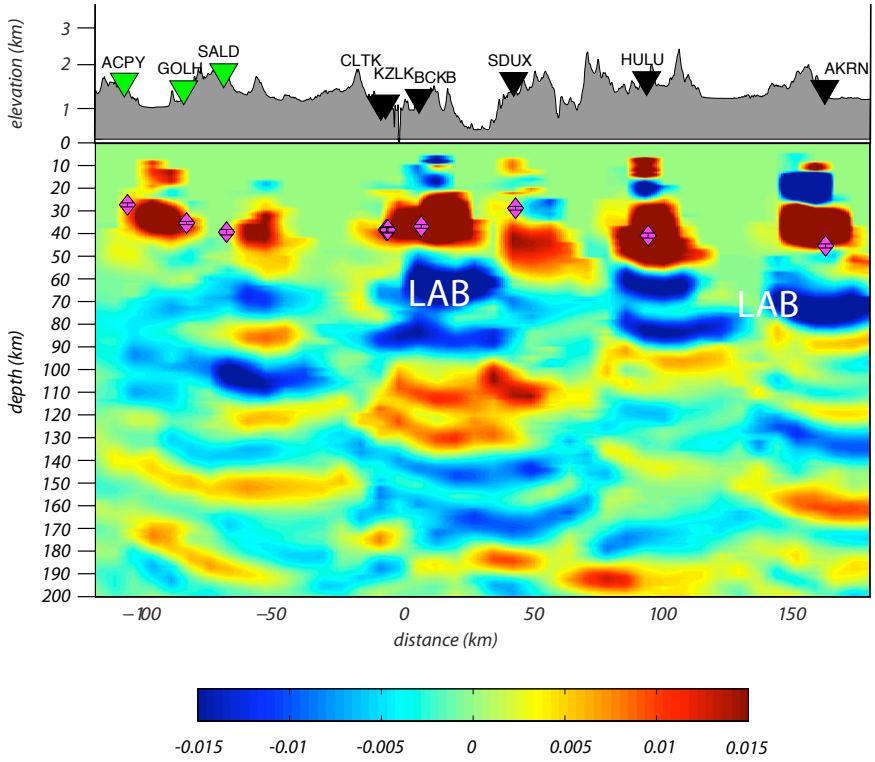

Figure 5.7. E-W S receiver function profile (see Fig. 5.4.e for location of profile). Pink diamonds presents Moho depths along the profile obtained from H-K solutions on the station.

5.4.2.3. C-C' Kirchhoff Profile

The NW-SE cross-section (Fig. 5.8) shows thick LAB location in depths of ~50 to 90 km beneath NW of profile. Other than that, LAB phases are not observed until the SW corner of cross-section. The LAB phases beneath Cyprus Island seem to appear at the depths of ~100 km to 120 km.

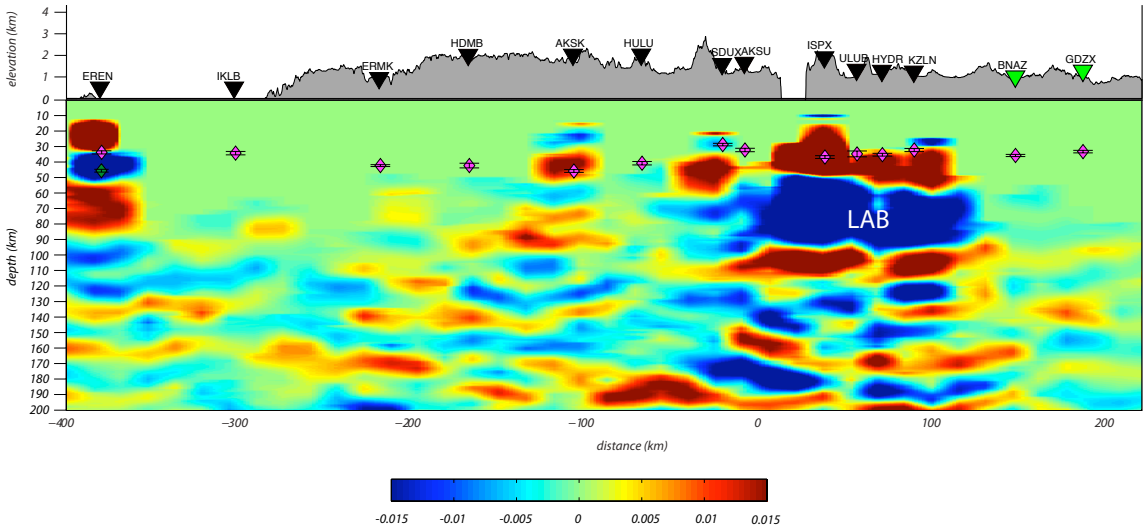

Figure 5.8. NW-SE S receiver function profile (see Fig. 5.5.e for location of profile). Diamonds presents Moho and Slab depths along the profile obtained from H-κ solutions on the station (Pink diamonds for Moho, dark green for Slab).

5.5. Conclusion

Overall, the H-κ and CCP profiles present Moho depth at ~35 km in the north of the region. Moho depth gets deeper to center and the eastern limb of IA. However, there is a clear observation of shallower Moho close to south at the end of IA on shore. The P receiver function study of Vanacore et al., (2013) provides similar results with our results in terms of Moho depth. However, their station sampling does not reveal localized differences as we do especially about Vp/Vs. Additionally, Pn study of Mutlu and Karabulut (2013) indicates ~40 km and/or thicker crustal thickness beneath IA which is not a compatible with our results that the depth of crust is calculated shallower than their results.

The previous studies on Anatolia and surroundings indicate a few number of S-RFs studies (e.g. Sodoudi et al., 2006; Angus et al., 2006). More recently, Kind et al., (2015) propose that LAB is in a flat shape lying between depths of 80 km 100 km. The depth values are supported by mainly body wave and surface wave tomography studies (e.g. Biryol et al., 2011; Bakirci et al., 2012; Salaun et al., 2012). S-RF cross-sections in this

chapter show that LAB is observed in similar depth range but upper boundary of LAB is imaged at shallower depth which is located at ~50 km depth. There are no continuous LAB phases that observed beneath IA. LAB indicates differences in continuation along N-S, E-W and NW-SE cross-sections. Kind et al., (2015) defines the Anatolian and African LAB in his profiles, however, we could not define this separation. The reason of this ambiguity can be related with cross-section dimension, frequency range in the deconvolution or teleseismic recording availability in the database.

6. CONLUSION

In this thesis, crustal structures of three different tectonic regions are revealed by using P and S receiver functions. Self-directed movements are dominated in regions where western section of North Anatolian Fault Zone (NAFZ) is a right lateral strike slip in East-West direction; Western Anatolia (WA) is an extension in North-South direction; Isparta Angle (IA) is a complex contamination of extension in its center and strike-slip dominated normal faults at its both East and West borders due to ongoing subduction of African slab along Hellenic and Cyprus arcs.

The western part of NAFZ is inspected by RFs where two main strands of NAFZ and accompanied small-scale faults are located. The main strands of NAFZ separate three different blocks from each other, which are named Istanbul-Zonguldak Zone, Armutlu-Almacik Zone and Sakarya Zone. Heterogeneous structure of these three different block and depth extend of northern and southern strands of NAFZ are revealed by methodologies that utilize P wave RFs. The RF waveforms are obtained from a temporary dense seismic network, DANA, whom station intervals are ~7 km. The network is grouped to six independent sub-sections, which are located in each three different blocks such as NW, NE, CW,CE, SW and SE. The aim of grouping is to increase signal to noise ratio of converted phases in each sub-section, especially, in groups close to main NAFZ strands in such a complex zones. Moho and Vp/Vs are calculated for the six sub-sections by $H-\kappa$ stacking. The results indicate an increment in crustal thickness from south to north, which is from 34-35 km to 37-39 km, respectively and crust is 1-2 km thicker in the eastern comparably to western subsection groups. Vp/Vs is constant ~1.70 for almost entire region except SE corner where Vp/Vs is 1.85. NA inversion algorithm is applied to all groups to reveal crustal and upper mantle seismic velocities. The region has <1.5 km thick low velocity with its Vs=1.8-2.3 km/s and Vp/Vs=1.72-196 layer at the surface underlain by a rapid transition to typical upper crust with its Vs=3.3-3.5 km/s and Vp/Vs=1.68-1.81 below depths of 2.2-5.9 km. Mid-crustal Vs =3.5-3.7 km/s and Vp/Vs=1.72-1.81 is observed which may extend to Moho depths in the NW, SW and SE groups. 10-13 thick high velocity lower crust is found in CW, CE and NE groups in which its Vs=3.9-4.2 km/s and Vp/Vs=1.67-1.74. Finally, 2 N-S and 3 E-W oriented CCP cross-sections are created

to image crustal and upper mantle discontinuities beneath three different blocks. The CCP cross-sections produce images that have lateral resolution less than 10 km. N-S cross-sections show that Moho is continuous ~34 beneath western groups, and it dips to south from ~32-33 km to ~37-38 km beneath eastern groups. Other than Moho, clear sub-Moho velocity discontinuities phases are observed at northern end of western groups. Sub-Moho positive and negative phases dip to northwards at depths of 45-50 and 50-55 km, respectively. The high resolved cross-sections indicate truncations in upper, mid crust, Moho and even upper mantle depts. These truncations are spatially correlated with northern and southern strands of NAFZ at the surface, which are followed by localized or distributed seismicity beneath NAFZ strands. A model for depth extends of northern and southern NAFZ strands is proposed, which is supported by crustal truncations and Moho depressions. The model suggests a dip variance of the northern and southern NAFZ strands from 90^{o} to 65^{o} beneath western and eastern groups of N-S cross-sections. The N-S cross-sections are located ~25 km away from each other. It is, also, possible to follow the northern strand down to at least 50 km while the southern strand does not seem depress Moho and reach sub-Moho depths as the northern strand does.

Upper, mid and lower crustal variations including locations of Low Velocity Zones (LVZ) and upper mantle velocity discontinuities are imaged by P wave RFs in WA. The metamorphic core complex (MMC) mostly covers WA and exhumation of MCC is believed to give initial shape of lower crust and Moho. P wave RFs are computed from sparsely distributed stations in which are run by national earthquake monitoring centers. $H-\kappa$ stacking results indicate that the crustal thickness can be grouped in three domains (eastern, center and west of MCC) with gradual decrease from east to west. The eastern of MCC presents 33-34 km Moho depth in the north and 36-39 km to south where Fethiye-Burdur Fault Zone (FBFZ) is crossed. The center of MCC shows 28-30 km Moho depth with an indication of thinning to from north to south. The western of MCC has 24-26 km Moho depth. The crustal thinning from east to west and north to south can be an indication of magnitude of N-S extension is higher in west and south. The overall Vp/Vs is low beneath MCC but there are localized high Vp/Vs zones that can be related with high heat flow and existence of partial melt in lower crust beneath those localized regions. N-S and E-W CCP cross-sections indicate compatible results with $H-\kappa$ stacking. The flat Moho and gradually thinning with its depth from east to west are presented by E-W cross-

sections. The gradual depth difference and flat Moho suggest a weak lower crust that moves laterally and smoothes Moho topography beneath MCC. It is proposed that N-S extension that is sourced from subducting African slab generates forces that activate lateral movement of weak lower crust. The presences of LVZs at upper to mid crustal depths are imaged along CCP cross-sections. Thermal hotspots at the surface, close to edges of Buyuk Menderes and Kucuk Menderes grabens, are correlated with these mid crust low velocity zones. Source of those thermal hotspots is related with mid crustal low velocity zones. Diagonal cross-sections are imaged ~5-8 km Moho difference at southeast coner of WA. The Moho difference is spatially correlated with FBFZ at the surface which stands as a transition zone between WA and Isparta Angle (IA).

P and S wave RFs are utilized to reveal crust, upper mantle and lithosphere asthenosphere boundary beneath IA. IA is Λ shaped region that is bordered by Hellenic and Cyprus arc on shore and FBFZ and Sultandağ Fault (SF) off shore. Moho depth and averaged Vp/Vs is calculated by $H-\kappa$ stacking. The results indicate that Moho depths and averaged Vp/Vs do not show gradual thickening or thinning to any orientation in IA. The complexity of IA present ~35-37 km crustal thickness with localized shallow depths at north. The center of region has 38-40 km Moho depth and it reaches to 44-46 km to southeastern corner of eastern limb. The western limb of IA, on the other hand, present crustal thickness between ~32-35 km. A common feature in IA is observed in its off shore margin where crust marginally shallow to ~23-28 km. The over all averaged Vp/Vs is 1.78 but Vp/Vs is respectively higher in the center and off shore margin of IA. Other than the Moho, sub-Moho phases are defined at 44 km beneath southern margin of IA and 43-46 km beneath Cyprus by both $H-\kappa$ stacking and CCP cross-sections. Sub-Moho phases are related to down going African slab beneath Anatolia. N-S cross-section indicates a stable Moho with almost no topography that can easily be traced from north to south. African slab related phases are imaged at southern end of N-S cross-section. Low amplitude Moho phases are observed at this part of profile. Diagonal cross-section is similarly show flat shape Moho and slab phases beneath its southeastern corner, beneath Cyprus. The flat shape Moho without topography can be related as an indication extension dominated inertial forces ın the crust of IA. The proposed inertial extension in IA is supported GPS models of Tiryakioğlu et al., (2013) which suggests the relative motions of western and eastern limbs to south-southwest and south- southeast, respectively, promote

the extension in the inner part of IA. The lithosphere-asthenosphere boundary is imaged by S wave RFs. Kirchhoff style migration is used in the same profile directions as P wave CCP cross-sections. LAB is imaged in all S wave cross-sections and it presents variation in its depth changing in 50 to 80 km depths.

In conclusion, we presented mainly, the usefulness and affectivity of receiver function method. If a proper station array designed or if there is enough sparsely distributed stations, it is possible to produce high resolved CCP cross-sections both in P and S RFs. A dense station distribution on all three regions helped us to create high resolved images from surface to upper mantle depths, where the new small-scale variations are revealed. These crustal and upper mantle features have not been highly resolved before beneath the study regions. Taking into all of these features in our current knowledge, we believe the produced images and their related results will help to create further sophisticated models for understanding on evaluation of the regions.

REFERENCES

Agostini, S., Doglioni, C., Innocenti, F., Manetti, P., Tonarini, S. and Savaşçın M. Y. 2007, "The transition from subduction-related to intraplate Neogene magmatism in the Western Anatolia and Aegean area". *Geological Society of America Special Paper*, 418, 1–16.

Aldanmaz, E., Pearce, J. A., Thirwall, M. F. and Mitchell, J., 2000, "Petrogenetic evolution of late Cenozoic, post-collision volcanism in western Anatolia, Turkey". *Journal of Volcanology & Geothermal Research*, 102, 67–95.

Alıcı, P., Temel, A., Gourgaud, A., Kieffer, G. and Gündoğdu, M. N., 1998, "Petrology and geochemistry of potassic rocks in the Gölcük area (Isparta, SW Turkey): genesis of enriched alkaline magmas". *Journal of Volcanology and Geothermal Research*, 85, 423–446.

Alıcı, P., Temel, A. and Gourgaud, A. 2002, "Pb-Nd-Sr isotope and trace element geochemistry of Quaternary extension-related alkaline volcanism: a case study of Kula region (western Anatolia, Turkey)". *Journal of Volcanology & Geothermal Research*, 115, 487–510.

Al-Lazki, A., Seber,D., Sandvol, E., T¨urkelli,N.,Mohamad, R.&Barazangi, M., 2003, "Tomographic Pn velocity and anisotropy structure beneath the Anatolian plateau (eastern Turkey) and surrounding regions". *Geophys. Res. Lett.,* 30, doi:10.1029/2003GL017391

Altuncu Poyraz, S., Teoman, U., Kahraman, M., Türkelli, N., Rost, S., Houseman, G., Thompson, D., Cornwell, D., Mutlu, A. K., Cambaz, D., Utkucu, M., Gülen, L., accepted 2015, "New constraints on micro-seismicity and stress state in the western part of the North Anatolian Fault Zone: Observations from a dense seismic array". *Tectonophysics***,** TECTO10106R2.

Ammon, C.J., G.E. Randall, and G. Zandt, 1990, “On the non-uniqueness of receiver function inversions”, *J. Geophys. Res.,* 95, 15,303–15,318.

Ammon, C.J., 1991, “The isolation of Receiver Effects from Teleseismic P Waveforms”, *Bull. Seism. Soc. Am*., 81, 2504-2510.

Angus, D.A., Wilson, C.D., Sandvol, E., Ni, F.J., 2006. “Lithospheric structure of the Arabian and Eurasian collision zone in eastern Turkey from *S*-wave receiver functions”. *Geophys. J. Int.,*166, 1335–1346.

Bakirci, T., Yoshizawa, K., and Özer, M. F., 2012, “Three-dimensional S wave structure of the upper mantle beneath Turkey from surface wave tomography”. *Geophys. J. Int.*, 190, 1058–1076.

Barka, A. & Gülen L., 1988, “New Constraints on Age and Total Offset of the North Anatolian Fault Zone: Implications for Tectonics of The Eastern Mediterranean Region”. *METU Journal of Pure and Applied Sciences*, 21, 1-3, 39-63.

Barka, A., 1992, “The North Anatolian fault zone”. *Ann. Tectonicae,* 6, 164–195.

Barka, A. A., 1996, “Slip distribution along the North Anatolian fault associated with the large earthquakes of the period 1939 to 1967”. *Bull. Seism. Soc. Am.* 86, 1238–1254.

Barka, A.A. and Reilinger, R., 1997, “Active tectonics of the Mediterranean region: deduced from GPS, neotectonic and seismicity data”. *Annali di Geophis.*, XI, 587–610.

Barka, A., 1999, “The 17 August 1999 Izmit earthquake”. *Science* 285, 1858–1859.

Barka, A., S. Akyuz, E. Altunel, G. Sunal, Z. Cakir, A. Dikbas, B. Yerli, R. Armijo, B. Meyer, J. B. Chabalier, T. Rockwell, J. Dolan, R. Hartleb, T. Dawson, S. Christofferson, A. Tucker, T. Fumal, R. Langridge H. Stenner, W. Lettis, W. Page, and J. Bachhuber, 2002, “The surface rupture and slip distribution of the 17 August 1999 Izmit earthquake (M 7.4), North Anatolian fault”. *Bull. Seism. Soc. Am.* 92, 43–

60.

Bath, M. and Stefannson, R., 1966. “S-P conversion at the base of the crust”. *Ann. Geofis.*, 19, 119-130.

Bekler, T., & Gokler, C., 2008, “Insight into the Crustal Structure of the Eastern Marmara Region, NW Turkey”. *Pure and Applied Geophysics*, 165, 295.

Biryol, C.B., Beck, S., Zandt, G., Ozacar, A.A., 2011, “Segmented African lithosphere beneath the Anatolian region inferred from teleseismic P-wave tomography”. *Geophys. J. Int.* 184, 1037–1057.

Bijwaard H, Spakman W, Engdahl ER, 1998, “Closing the gap between global and regional mantle tomography”. *J Geophys Res* 103:30055–30078. doi:10.1029/98JB02467

Bock, G. & Kind, R., 1991, “A global study of *S*-to-*P* and P-to-S conversions from the upper mantle transition zone”. *Geophys. J. Int.,* 107, 117–129.

Bostock, M. G., and Sacchi, M.D., 1997, “Deconvolution of teleseismic recordings for mantle structure”. *Geophys. J. Int.* 129, 143–152.

Bozkurt, E., Oberhänsli, R., 2001, “Menderes Masif (Western Turkey): structural, metamorphic and magmatic evolution – a synthesis”. *International Journal of Earth Sciences*, 89, 679-708.

Bozkurt, E., Sözbilir, H., 2004, “Tectonic evolution of the Gediz Graben: field evidence for an episodic, two-stage extension in western Turke”. *Geological Magazine* 141, 63-79.

Bozkurt, E., Mittwede, K.S., 2005, “Introduction: Evolution of continental extensional tectonics of western Turkey”. *Geodinamica Acta* 18/3-4, 153-165.

Bürgmann, R., and G. Dresen, 2008, “Rheology of the lower crust and upper mantle: Evidence from rock mechanics, geodesy and field observations”. *Ann. Rev. Earth*

Plan. Sci., 36, doi:10.1146/annurev.earth.36.031207.124326, 531-567.

Cambaz, M.D. and Karabulut, H., 2010, "Love-wave group velocity maps of Turkey and surrounding Regions". *Geophys. J. Int,* 181, 502–520.

Cassidy, J. F., 1992, "Numerical experiments in broadband receiver function analysis", *Bull. Seismol. Soc. Am.,* 82, 1453– 1474.

Celik, O.F., Delaloye, M.F., 2003, "Origin of metamorphic soles and their post kinematic mafic dyke swarms in the Antalya and Lycian ophiplites, SW Turkey". *Geological Journal*, 38, 235-256.

Chen, F., Siebel, W., Satir, M., Terzioğlu, N. & Saka, K., 2002, "Geochronology of the Karadere basement (NW Turkey) and implications for the geological evolution of the İstanbul Zone". *International Journal Earth Sciences,* 91, 469-481.

Collins, A. & Robertson, A. H. F., 2003, "Kinematic evidence for Late Mesozoic – Miocene emplacement of the Lycian Allochthon over the Western Anatolide Belt, SW Turkey". *Geological Journal*, 38, 295–310.

Cornwell, DG., Maguire, PKH., England, RW. & Stuart, GW., 2010, "Imaging detailed crustal structure and magmatic intrusion across the Ethiopian Rift using a dense linear broadband array". *Geochemistry, Geophysics, Geosystems*, vol 11, no. 1, Q0AB03.

Çoban, H. & Flower, M. F. J., 2006, "Mineral phase compositions in silica-undersaturated 'leucite' lamproites from the Bucak area, Isparta, SW Turkey". *Lithos*, 89, 275–299.

Davis, J.P. & Henson, I.H., 1993, "User's guide to Xgbm: An X-windows system to compute Gaussian beam synthetic seismograms, *Report TGAL-93–02, Teledyne Geotech Alexandria Laboratories*.

Dean, W.T., Monod, O., Rickards, R.B., Demir, O. & Bultynck, P., 2000, "Lower Palaeozoic stratigraphy and palaeontology, Karadere-Zirze area, Pontus Mountains,

northern Turkey". *Geological Magazine*, 137, 555-582.

De Graciansky, P.C., 1972, "Reserches gèologiques dans le Taurus Lycien occidental, Thèse, University de Paris-Sud". *Orsay*, 570.

Dellinger, J. A., Gray, S.H., Murphy, G. E. and Etgen, J.T., 2000, "Efficient 2.5-D true-amplitude migration". *Geophysics*, 65(3), 943–950.

Delpth, R.J., Biryol, C.B., Beck, L.S., Zandt, G., 2015, "Shear wave velocity structure of the Anatolian Plate: anomalously slow crust in southwestern Turkey". *Geophy. J. Int*. 202, 261-276.

DeMets, C., Gordon, R.G., Argus, D.F. and Stein, S., 1994, "Effects of recent revisions to the geomagnetic reversal time scale on estimates of current plate motions". *Geophy. Res. Lett.*, 21, 2191-2194.

Demirtasli, E., Turhan, N., Bilgin, A. Z. and Selim, M., 1984, "Geology of the Bolkar Mountains". *In: Tekeli, O. & Goncuoglu, M. C. (eds) Geology of the Taurus Belt. Proceedings of the International Symposium*, Ankara, 125–141.

Dewey, J.F. & Şengör, A.M.C., 1979, "Aegean and surrounding regions: complex multiple and continuum tectonics in a convergent zone". *Geological Society of America Bulletin* 90, 84–92.

Dilek, Y., Thy, P., Hacker, B. and Ggrundvig, S., 1999a, "Structure and petrology of Tauride ophiolites and mafic dike intrusions (Turkey): Implications for the Neo-Tethyan ocean". *Bulletin of the Geological Society of America*, 111, 1192–1216.

Dilek, Y. and Altunkaynak, S., 2007, "Cenozoic crustal evolution and mantle dynamics of post-collisional magmatism in western Anatolia". *International Geology Review*, 49, 431–453.

Dilek, Y. and Altunkaynak., 2009, "Geochemical and temporal evolution of Cenozoic

magmatism in western Turkey: mantle response to collision, slab break-off, and lithospheric tearing in an orogenic belt". *Geological Society, London, Special Publications*, 311, 213-233. doi:10.1144/SP311.8.

Doglioni, C., Agostini, S., Crespi, M., Innocenti, F., Manetti, P., Riguzzi, F. and Savaşcın¸ IN, Y. 2002, "On the extension in western Anatolia and the Aegean Sea". *Journal of the Virtual Explorer*, 8, 169–183.

Dueker, K.G. & Sheehan, A.F. 1997, "Mantle discontinuity structure from mid point stacks of converted P to S waves across the Yellowstone hotspot track". *Journal of Geophysical Research*, Vol. 102, No. B4, Pages 8313-8327.

Dueker, K. G. & Sheehan, A. F. 1998, "Mantle discontinuity structure beneath the Colorado Rock Mountains and High Plains". *Journal of Geophysical Research,* 103, 7153-71169.

Duquet, B., Marfurt, K. and Dellinger, J.A., 2000, "Kirchhoff modeling, inversion for reflectivity, and subsurface illumination". *Geophysics*, 65, 1195– 1209.

Dziewonski, A. and Romanowiez, B., 2007, "Treatise on Geophysics". 1, 222-223

Elitok, Ö. and Drüppel, K., 2008, "Geochemistry and tectonic significance of metamorphic sole rocks beneath the Beysehir-Hoyran ophiolite (SW Turkey)". *Lithos*, 100, 322–353.

Emre, Ö., Duman, T.Y., Duman, fi., Özalp, S., 2012, "Türkiye diri fay haritası (yenilenmiş)". *Maden Tetkik ve Arama Yayınları*, Ankara.

Farber, S. & Müller, G., 1980, "Sp phases from the transition zone between the upper and lower mantle", *Bull. seism. Soc. Am.,* 70, 487–508.

Farra, V. & Vinnik, L., 2000, "Upper mantle stratification by P and S receiver functions". *Geophys. J. Int.,* 141, 699–712.

Feigl, K. L., F. Sarti, H. Vadon, S. McClusky, S. Ergintav, P. Durand, R. Burgmann, A. Rigo, D. Massonnet, and R. Reilinger,2002, "Estimating slip distribution for the Izmit mainshock from coseismic GPS, ERS-1, RADARSAT and SPOT measurements". *Bull. Seismol. Soc. Am.*, 92(1), 138– 160.

Fichtner, A., Saygin, E., Taymaz, T., Cupillard, P., Capdevillee, Y., Trampert, J., 2013, "The deep structure of the North Anatolian Fault Zone". *Earth Planet. Sci. Lett.* 373, 109–117.

Francalanci, L., Innocenti, F., Manetti, P. and Savaşçın, M. Y., 2000, "Neogene alkaline volcanism of the Afyon-Isparta area, Turkey: petrogenesis and geodynamic implications". *Mineralogy & Petrology*, 70, 285–312.

Glover, C., Robertson, A., 1998, "Neotectonic intersection of the Aegean and Cyprus tectonic arcs: extensional and strike-slip faulting in the Isparta Angle, SW Turkey". *Tectonophysics* 298, 103 – 132.

Govers, R. and Wortel, M.J.R., 2005, "Lithosphere tearing at STEP faults: Response to edges of subduction zones". *Earth and Planetary Science Letters.* 236, 505-523.

Görür, N., Şengör, A.M.C., Sakınç, M., Tüysüz, O., Akkök, R., Yiğitbaş, E., Oktay, F. Y., Barka, A.A., Sarıca, N., Ecevitoğlu, B., Demirbağ, E., Ersoy, S., Algan, O., Güneysu, C. & Akyol, A., 1995, "Rift formation in the Gökova region, southwest Anatolia: implications for the opening of the Aegean Sea". *Geological Magazine* 132, 637–50.

Görür, N., Monod, O., Okay, A.I., Şengör, A.M.C., Tüysüz, O., Yiğitbaş, E., Sakinç, M. & Akkök, R., 1997, "Palaeogeographic and tectonic position of the Carboniferous rocks of the western Pontides (Turkey) in the frame of the Variscan belt". *Bulletin Societe Géologique de France* 168, 197-205.

Gurrola, H., Baker, F.G. and Minster, B.J., 1995, "Simultaneous timedomain deconvolution with application to the computer of receiver functions". *Geophys. J. Int.* 120, 537–543.

Gülen , L., 1990, “Isotopic characterization of Aegean magmatism and geodynamic evolution of the Aegean subduction”. International Earth Science Colloquium on the Aegean Region, Proceedings 2, 143–167.

Gürsu, S., Goncuoglu, M. C. and Bayhan, H., 2004, “Geology and geochemistry of the Pre-early Cambrian rocks in the Sandikli area: implications for the Pan- African evolution of NW Gondwanaland”. *Gondwana Research,* 7, 923–935.

Innocenti, F., Agotini, S., Di Vincenzo, G., Doglioni, C., Manetti, P., Savaşçin, M.Y., Tonarini, S., 2005, “Neogene and Quaternary volcanism in Western Anatolia: Magma sources and geodynamic evolution”. *Marine Geology,* 221, 397-421.

Jolivet, L., et al., 2012, “Aegean tectonics: Strain localization, slab tearing and trench retreat”. *Tectonophysics*, doi:10.1016/j.tecto.2012.06.011

Julia, J., and J. Mejia, 2004, “Thickness and Vp/Vs ratio variation in the Iberian crust”, *Geophys. J. Int.,* 156, 59– 72.

Hall, J., Aksu., A.E., Elitez, I., Yaltırak, C., Çiftçi, G., 2014, “The Fethiye–Burdur Fault Zone: A component of upper plate extension of the subduction transform edge propagator fault linking Hellenic and Cyprus Arcs, Eastern Mediterranean”. *Tectonophysics,* 635, 80-99.

Handy, M.R., Hirth, G., Bürgmann, R., 2007, “Continental fault structure and rheology from the frictional-to-viscous transition downward. In: Handy, M.R., Hirth, G., Hovius, N. (Eds.), Tectonic Faults: Agents of Change on a Dynamic Earth”. *MIT Press, Cambridge,* MA, pp. 139–181.

Hearn, E. H., S. McClusky, S. Ergintav, and R. E. Reilinger, 2009, “Izmit earthquake postseismic deformation and dynamics of the North Anatolian Fault Zone”. *J. Geophys. Res.*, 114, B08405, doi:10.1029/2008JB006026.

Helffrich, G., 2006, “Extended-time multitaper frequency domain cross-correlation receiver-function estimation”. *Bull. Seism. Soc. Am.* 96 (1), 344–347. doi:10.1785/0120050098.

Henstock, T.J., Levander, A. and Hole, J.A., 1997, “Deformation in the lower crust of the San Andreas fault system in northern California”. *Science*, 278, 650–653.

Karabulut, H., Paul, A., Ergün, A.T., Hatzfeld, D., Childs, M.D. And Aktar M., 2013, “Long-wavelength undulations of the seismic Moho beneath the strongly stretched Western Anatolia”. *Geophys. J. Int.*, doi: 10.1093/gji/ggt100.

Karahan, A., Berckhemer, H. & Baier,B., 2001, “Crustal structure at the western end of the North Anatolian Fault Zone from deep seismic sounding”. *Annali di Geofisica,* 44, 49–68.

Kenner, S.J. and Segall, P., 2003, “Lower crustal structure in northern California: Implications from strain-rate variations following the 1906 San Francisco earthquake”. *J. Geophys. Res.*, 108. doi:10.1029/2001JB000189.

Kennett, B. L. N. and E. R. Engdahl, 1991, “Travel times for global earthquake location and phase identification”. *Geophys. J. Int.*, 105, 429-465.

Kind, R., Eken, T., Tilmann, F., Sodoudi, F., Taymaz, T., Bulut, F., Yuan, X., Can, B. and Schneider, F., 2015, “Thickness of the lithosphere beneath Turkey and surroundings from S-receiver functions”. Solid Earth, 6, 971-984.

Kissel, C., Laj, C, 1988, “Tertiary geodynamical evalution of the Aegean arc: a paleomagnetic reconstruction”. *Tectonophysics*, 146, 183-201.

Kissel, C., Averbuch, O., de Lamotte, DF., Monod O., Allerton, S., 1993, “First paleomagnetic evidence for a post-Eocene clockwise rotation of the Western Taurides thrust belt east of the Isparta reentrant (Southwestern Turkey)”. *Eart. Planet. Sci. Lett.*, 117, 1-14.

Koçyiğit, A. and Özacar, A., A., 2003, "Extensional Neotectonic Regime through the NE Edge of the Outer Isparta Angle, SW Turkey: New Field and Seismic Data". *Turkish J. Earth Sci*., 12, 67-90.

Komec Mutlu A., Karabulut, H, 2011, "Anisotropic Pn Travel Time Tomography of Turkey and Adjacent Regions". *Geophy. J. Int.*, 187, 1743-1758.

Kumar, P., Yuan, X., Kind, R. and Kosarev, G., 2005a, "The lithosphere–asthenosphere boundary in the Tien Shan-Karakoram Region from S receiver functions—evidence for continental subduction". *Geophys. Res. Lett.,* 32, L07305, doi:10.1029/2004GL022291.

Kumar, P. *et al.*, 2005b, "The lithosphere–asthenosphere boundary in the north west Atlantic region". *Earth planet. Sci. Lett.,* 236, 249–257.

Kumar, P., Yuan, X., Kind, R. & Ni, J., 2005c, "Imaging the colliding Indian and Asian continental lithospheres beneath Tibet". *J. geophys. Res.,* submitted.

Kumar, P., Kind, R., Priestley, K. & Dahl-Jensen, T., 2005d, "Crustal structures of Iceland and Greenland from receiver function studies". *J. geophys. Res.,* submitted.

Kumral, M., Çoban, H., Gedikoğlu, A. and Kılınç, A., 2006, "Petrology and geochemistry of augite trachytes and porphyritic trachytes from the Gölcük volcanic region, SW Turkey: A case study". *Journal of Asian Earth Sciences*, 27, 707–716.

Koulakov, I., Bindi, D., Parolai, S., Grosser, H., Milkereit, C., 2010, "Distribution of seismic velocities and attenuation in the crust beneath the North Anatolian Fault (Turkey) from local earthquake tomography". *Bull. Seismol. Soc. Am.* 100, 207–224.

Langston, C.A., 1979, "Structure under Mount Rainier,Washington, inferred from teleseismic body waves", *J. Geophys. Res.,* 84, 4749–4762.

Lay, T. and Wallace, T.C., 1995, "Modern Global Seismology". *Volume 58 of International*

Geophysics series. Academic Press.

Le Pichon, X. & Angelier, J. 1979, "The Aegean arc and trench system: a key to the neotectonic evolution of the eastern Mediterranean area". *Tectonophysics*, 60, 1–42.

Levin, V., and J. Park (1997a). Crustal anisotropy beneath the Ural mtns oredeep from teleseismic receiver functions, *Geophys. Res. Lett.* 24, 283–1286.

Li, X., Kind, R., Yuan, X., W¨olbern, I. & Hanka, W., 2004, "Rejuvenation of the lithosphere by the Hawaiian plume". *Nature,* 427, 827–829.

Ligorria, J. P., and C. J. Ammon, 1999, "Iterative deconvolution and receiver function estimation", *Bull. Seismol. Soc. Am.*, 89, 1395–1400.

Ligorria, J.P., 2000, "An investigation of the mantle crust transition beneath North Amerial and Poisson's ratio of the North Ameriacan crust". *PhD, Thesis, p. 261, Saint Louis Univ., Saint Louis.*

McClusky, S., S. Balassanian, A. Barka, C. Demir, S. Ergintav, I. Georgiev, O. Gurkan, M. Hamburger, K. Hurst, H. Kahle, K. Kastens, G. Kekelidze, R. King, V. Kotzev, O. Lenk, S. Mahmoud, A. Mishin, M., Nadariya, A. Ouzounis, D. Paradissis, Y. Peter, M. Prilepin, R. Reilinger, I. Sanli, H. Seeger, A. Tealeb, M. N. Toksoz, and G. Veis, 2000, "Global positioning system constraints on plate kinematics and dynamics in the eastern Mediterranean and Caucasus". *J. Geophys. Res*. 105, no. 3, 5695–5719.

McClusky, S., Reilinger, R., Mahmoud, S., Ben Sari, D. & Tealeb, A., 2003, "GPS constraints on Africa (Nubia) and Arabia plate motions". *Geophys. J. Int.*, 155, 126-138.

McKenzie, D. P., 1978, "Active tectonics of the Alpine-Himalayan belt: the Aegean Sea and surrounding regions". *Geophysical Journal of Royal Astronomical Society*, 55, 217–54.

Menke, W., 1989, "Geophysical data anlalysis: discreate inverse theory, rev. edn". *Academic Press, San Diego*.

Meulenkamp, J.E., Wortel, W.J.R., Van Wamel, W.A., Spakman, W. & Hoogerduyn Stratıng, E., 1988, "On the Hellenic subduction zone and geodynamic evolution of Crete in the late Middle Miocene". *Tectonophysics,* 146, 203–15.

Nemeth, T., C. Wu, and Schuster, G.T., 1999, "Least-squares migration of incomplete reflection data". *Geophysics*, 64, 208– 221.

Okay, A.İ., 1989, "Geology of the Menderes Massif and the Lycian Nappes south of Denizli, western Taurides". *Mineral Res.Expl. Bull*., 109, 37-51.

Okay, A.I., Şengör, A.M.C.& Görür, N., 1994, "Kinematic history of the opening of the Black Sea and its effect on the surrounding regions". *Geology,* 22, 267-270.

Okay, A.I., Satir, M., Maluski, H., Siyako, M., Monie, P., Metzger, R. & Akyüz, S., 1996, "Paleo- and Neo-Tethyan events in northwest Turkey: Geological and geochronological constraints". *In: A. Yin & M. Harrison (eds.), Tectonics of Asia, Cambridge University Press*, 420-441.

Okay, A.I., Tüysüz, O., 1999, "Tethyan sutures of northern Turkey". *Geol. Soc. London (Spec. Publ.)* 156, 475–515.

Okay, A.İ. and Altıner, D., 2007, "A Condensed Mesozoic Succession North of İzmir: A Fragment of the Anatolide-Tauride Platform in the Bornova Flysch Zone". *Turkish J. Earth Sci.*, 16, 257–279.

Okay, A. I., 2008, "Geology of Turkey: A Synopsis". *Anschnitt* 21, 19-42.

Özbakır, A.D., Şengör, A.M.C.,Wortel, M.J.R., Govers, R., 2013, "The Pliny–Strabo trench region: a large shear zone resulting fromslab tearing". *Earth Planet. Sci. Lett.* 375, 188–195.

Özgül, N., 1984, “Stratigraphy and tectonic evolution of the Central Taurides”. *In: Tekeli, O. & Goncuoglu, M. C. (eds) Geology of the Taurus Belt. Proceedings of the International Symposium on the Geology of the Taurus Belt, 1983, Ankara – Turkey*, Mineral Research and Exploration Institute of Turkey, Ankara, 77–90.

Park, J., Lindberg, C. R., and Vernon III, F.L., 1987, “Multitaper spectral analysis of high-frequency seismograms”. *J. Geophys. Res.* 92, 12,675–12,684.

Park, J., and Levin, V., 2000, “Receiver functions from multiple-taper spectral correlation estimates”. *Bull. Seism. Soc. Am.* 90, 1507–1520.

Parker, R.L., 1994, “Geophyiscal Inverse Theory”. *Princeton Univ. Press, Princeton*.

Paul, A., Karabulut, H., Komec-Mutlu, A., Salaün, G., 2014, “A comprehensive and densely sampled map of shear-wave azimuthal anisotropy in the Aegean–Anatolia region”. *Earth. Pla. Sci. Let*. 389, 11-22.

Pe-Piper, G., Piper, D.J.W., 2006, “Unique features of the Cenozoic igneous rocks of Greece. In: Dilek, Y., Pavlides, S. (Eds.), Postcollisional Tectonics and Magmatism in the Mediterranean Region and Asia”. *Geological Society of America Special Paper. Geological Society of America*, pp. 259–282 http://dx.doi.org/10.1130/2006.2409(14).

Pe-Piper, G., Piper, D.J.W., 2007, “Neogene back-arc volcanism of the Aegean: new in-sights into the relationship between magmatism and tectonics. In: Beccaluva, L., Bianchini, G. (Eds.), Cenozoic Volcanism in the Mediterranean Area”. *Geological Society of America Special Paper. Geological Society of America*, pp. 17–31. http://dx.doi.org/10.1130/2007.2418(02).

Pickett, E.A. & Robertson, A.H.F., 1996, “Formation of the Late Paleozoic-Early Mesozoic Karakaya Complex and related ophiolites in NW Turkey by Paleotethyan subduction accretion”. *Journal of the Geological Society London*, 153, 995-1009.

Phinney, R. A., 1964, “Structure of earths crust from spectral behavior of long-period body waves”, *J. Geophys. Res.,* 69, 2997-3017.

Piromallo C, Morelli A., 2003, “P wave tomography of the mantle under the Alpine-Mediterranean area”. *J Geophys Res* 108:2065. doi:2010.2129/2002JB001757

Platt, J.P., Behr, W.M., 2011, “Deep structure of lithospheric fault zones”. *Geophys. Res. Lett*. 38(24).

Pollitz, F.F, Wicks, C. Thatcher, W., 2001, “Mantle flow beneath a continental strike-slip fault: Postseismic deformation after the 1999 Hector Mine Earthquake”. *Science*, 293, 1814-1818.

Press, W. H., Teukolsky, S.A., Vetterling, W.T., and Flannery, B.P., 1992, “Numerical Recipes”. Second Ed., *Cambridge University Press, Cambridge, United Kingdom, xxvi _ 963.*

Reilinger R.E., McClusky S.C., Oral M.B., King W. & Toksöz M.N., 1997, “Global Positioning System measurements of present-day crustal movements in the Arabia–Africa-Eurasia plate collision zone”. *J. geophy. Res.*, 102, 9983–9999.

Reilinger, R., McClusky, S., Vernant, P., Lawrence, S., Ergintav, S., Cakmak, R., Ozener, H., Kadirov, F., Guliev, I., Stepanyan, R., Nadariya, M., Hahubia, G., Mahmoud, S., Sakr, K., ArRajehi, A., Paradissis, D., Al-Aydrus, A., Prilepin, M., Guseva, T., Evren, E., Dmitrotsa, A., Filikov, S.V., Gomez, F., Al-Ghazzi, R., Karam, G., 2006, “GPS constraints on continental deformation in the Africa- Arabia-Eurasia continental collision zone and implications for the dynamics of plate interactions”. *J. Geophys. Res*. 111, B05411, doi:10.1029/2005JB004051.

Ricou LE, Argyriadis I, Marcoux J., 1975, “L’axe calcaire du Taurus, un alignement de fenetres arabo-africaines sous des nappes radiolaritiques, ophiolitiques et me´tamorphiques”. *Bulletin de la Societe Geologique de France* 17: 1024–1043.

Richardson-Bunbury, J. M., 1996, "The Kula volcanic field, western Turkey: the development of a Holocene alkali basalt province and the adjacent normal-faulting graben". *Geological Magazine*, 133, 275–283.

Rimmelé, G., Oberhänsli, R., Candan, O., Goffé, B., and Jolivet, L., 2006, "The wide distribution of HP-LT rocks in the Lycian Belt (Western Turkey): implications for accretionary wedge geometry". *Geological Society, London, Special Publications,* 260, 447-466.

Ring, U., and Layer, P.W., 2003, "High-pressure metamorphism in the Aegean, eastern Mediterranean: Underplating and exhumation from the Late Cretaceous until the Miocene to Recent above the retreating Hellenic subduction zone". *Tectonics*, v. 22, p. 6-1–6-23, doi: 10.1029/2001TC001350.

Robertson, A.H.F., Ustaömer, T., 2004, "Tectonic evolution of the Intra-Pontide suture zone in the Armutlu Peninsula, NW Turkey". *Tectonophysics*, 381, 1–4, 175-209.

Salaün, G., Pedersen, H.A., Paul, A., Farra, V., Karabulut, H., Hatzfeld, D., Papazachos, C., Childs, D.M., Pequegnat, C., 2012, "The SIMBAAD Team, 2012. High-resolution surface wave tomography beneath the Aegean-Anatolia region: constraints on upper-mantle structure". *Geophys. J. Int*. 190, 406–420.

Sambridge, M., 1999, "Geophysical inversion with a Neighbourhood algorithm, I, Searching a parameter space". *Geophys. J. Int.*, 138, 479–494.

Sarı, B., 2009, "Planktonic foraminiferal biostratigraphy of the Coniacian-Maastrichtian sequences of the Bey Dağları Autochthon, western Taurides, Turkey: thin-section zonation". *Cretaceous Research*, 30, 1103-1132.

Saunders, P., Priestly, K. & Taymaz, T., 1998, "Variations on the crustal structure beneath Western Turkey". *J. Geophys. Int.*, 13, 373-389.

Savaşçın, M. Y. and Oyman, T., 1998, "Tectonomagmatic evolution of alkaline volcanics at

the Kirka-Afyon-Isparta structural trend, SW Turkey". *Turkish Journal of Earth Sciences*, 7, 201–214.

Searcy, C. K., Christensen, D.H. and Zandt, G., 1996, "Velocity structure beneath College Station Alaska from receiver functions". *Bull. Seism. Soc. Am.* 86, 232–241.

Seyitoğlu, G. & Scott, B., 1991, "Late Cenozoic crustal extension and basin formation in west Turkey". *Geol. Mag.*, 128, 155–166.

Seyitoğlu, G., Scott, B.C. & Rundle, C.C., 1992, "Timing of Cenozoic extensional tectonics in west Turkey". *J. Geol. Soc., Lond.*, 149, 533–538.

Seyitoğlu, G., Anderson, D., Nowell, G. and Scott, B., 1997, "The evolution from Miocene potassic to Quaternary sodic magmatism in western Turkey: implications for enrichment processes in the lithospheric mantle". *Journal of Volcanology and Geothermal Research*, 76, 127–147.

Schulte-Pelkum, V. And Y. Ben-Zion, 2012, "Apparent vertical Moho offsets under continental strike-slip faults from lithology contrasts in the seismogenic crust". *Bull. Seis. Soc. Am*. 102, 2757-2763, doi: 10.1785/0120120139, 2012.

Sodoudi, F., R. Kind, D. Hatzfeld, K. Priestley, W. Hanka, K. Wylegalla, G. Stavrakakis, A. Vafidis, H.-P. Harjes, and M. Bohnhoff 2006, "Lithospheric structure of the Aegean obtained from P and S receiver functions". *J. Geophys. Res.*, 111, B12307, doi:10.1029/2005JB003932.

Stein, R.S., Barka, A.A., Dieterich, J.H., 1997, "Progressive failure on the North Anatolian Fault since 1939 by earthquake stress triggering". *Geophys. J. Int*. 128, 594–604.

Stampfli G.M., 2000, "Tethyan Oceans", *From: Bozkurt E., Winchester, J. A. and Piper, J. D.A., (eds) Tectonic and Magmatism in Turkey and the Surrounding Area. Geological Society, London, Special Publications*, Vol.173, pp. 1-23.

Şapaş, A. and Boztepe-Güney, A., 2009. "Shear wave splitting in the Isparta Angle, southwestern Turkey: anisotropic complexity in the mantle". *J. Earth Syst. Sci.,* 118, 71–80.

Şengör, A.M.C. 1979, "The North Anatolian Transform Fault: its age, offset and tectonic significance". *Journal of the Geological Society, London* 136, 269–82.

Şengör, A.M.C. & Yilmaz, Y., 1981, "Tethyan evolution of Turkey, a plate tectonic approach". *Tectonophysics*, 75, 181-241.

Şengör, A.M.C., Görür, N. & Saroğlu, F., 1985, "Strike-slip faulting and related basin formation in zones of tectonic escape: Turkey as a case study, in Strike-slip Faulting and Basin Formation". *Soc. Econ. Paleont. Miner. Spec. Publ.* pp. 227–264, Vol. 37.

Şengör, A.M.C. 1987. Cross-faults and differential stretching of hanging walls in regions of low-angle normal faulting: examples from western Turkey. In: Coward, M. P., Dewey, F. & Hancock, P. L. (eds), Continental Extensional Tectonics. Geological Society, London, Special Publications 28, 575–89.

Tank SB, Honkura Y, Ogawa Y, Matsushima M, Oshiman N, Tuncer MK, Celik C, Tolak E, Isikara AM, 2005, "Magnetotelluric imaging of the fault rupture area of the 1999 Izmit (Turkey) earthquake". *Phys. Earth. Planet. Int.*, 150, 213–225.

Tarantola, A., 1987, "Inverse Problem T heory". *Elsevier, Amsterdam*.

Taymaz, T. and Tan, O., 2001. "Source parameters of June 6, 2000 Orta-Çankırı (Mw=6.0) and December 15, 2000 Sultandağ-Akşehir (Mw=6.0) earthquakes obtained from inversion of teleseismic P and SH-body-waveforms". *Symposia on Seismotectonics of the North-Western Anatolia-Aegean and Recent Turkish Earthquakes*, İstanbul, Extended Abstracts, 96-107.

Taymaz, T., Tan, O., .Özalaybey, S. and Karabulut, H., 2002., "Source characteristics of February 3, 2002 .ay-Sultandağ Earthquake (Mw=6.5) sequence in SW-Turkey: a

synthesis of Seismological Observations of Body-Waveforms, Strong Motions, and Aftershock Seismicity Survey Data". *1st International Symposium of İstanbul Technical University the Faculty of Mines on Earth Sciences and Engineering,* İstanbul-Turkey, Abstracts, p. 60.

Taymaz, T., Yılmaz, Y. & Dilek, Y., 2007a, "The Geodynamics of the Aegean and Anatolia: Introduction, in The Geodynamics of the Aegean and Anatolia". *J. Geol. Soc., London, Special Publications,* pp. 1–16, Vol. 29.

Tezel, T., Shibutani, T. and Kaypak, B., 2010, "Crustal structure variation on western Turkey inferred from the receiver function analysis". *Tectonophysics*, 492, 240-252.

Toçkaer, M., Agostini, S. and Savaşçın, M.Y., 2005, "Geotectonic Setting and Origin of the Youngest Kula Volcanics (Western Anatolia), with a New Emplacement Model". Turkish J. Earth Sci., 14, 145–166.

Thomson, D. J., 1982, "Spectrum estimation and harmonic analysis". *IEEE Proc.* 70, 1055–1096.

Thomson, S.N., Stöckhert, B. & Brix, M.R., 1998, "Thermochronology of the high-pressure metamorphic rocks of Crete, Greece: implications for the speed of tectonic processes". *Geology*, 26, 259–62.

Thomson, S. N. and Ring, U., 2006., "Thermochronologic evaluation of postcollision extension in the Anatolide orogen, western Turkey". *Tectonics*, 25, TC3005, doi: 10.1029/2005TC001833.

Tiryakioğlu, I., Floyd, M., Erdoğan, S., Gülal, E., Ergintav, S., McClusky, S., Reilinger, R., 2013, "GPS Constraints on Active Deformation in the Isparta Angle Region of SW Turkey". *Geophys. J. Int.* 195, 1455–1463.

Ustaömer P.A., Mundil, R. & Renne, P.R., 2005, "U/Pb and Pb/Pb zircon ages for arc-related intrusions of the Bolu Massif (W Pontides, NW Turkey): evidence for Late

Precambrian (Cadomian) age". *Terra Nova,* 17, 215-223.

Vanacore, E., Taymaz, T., Saygin, E., 2013, "Moho structure of the Anatolian plate from receiver function analysis". *Geophys. J. Int.* 193, http://dx.doi.org/10.1093/ gji/ggs107.

Weber, M., 1988, "Computation of body-wave seismograms in absorbing 2-D media using the Gaussian beam method: comparison with exact methods". *Geophys. J.,* 92, 9–24.

Wilson, D., Aster, R., and the RISTRA Group, 2003, "Imaging crust and upper mantle seismic structure in the southwestern United States using teleseismic receiver functions". *Leading Edge*, 22, 232–237.

Wilson C.K., Jones C.H., Molnar P., Sheehan A.F., Boyd O.S., 2004, "Distributed deformation in the lower crust and upper mantle beneath a continental strike-slip fault zone: Marlborough fault system, South Island, New Zealand". *Geology,* 32, 837–840.

Wilson, D., and Aster, R., 2005, "Seismic imaging of the crust and upper mantle using regularized joint receiver functions, frequency–wave number filtering, and multimode Kirchhoff migration". *J. Geophys. Res.*, 110, B05305.

Wilson, D.C., Angus, D.A., Ni, J. & Grand, S., 2006, "Constraints on the interpretation of S-to-P receiver functions". *Geophys. J. Int.,* 165, 969–980.

Wittlinger, G., Vergne, J., Tapponnier, P., Farra, V., Poupinet, G., Jiang, M., Su, H., Herquel, G., Paul, A., 2004, "Teleseismic imaging of subducting lithosphere and Moho offsets beneath western Tibet". *Earth Planet. Sci. Lett*., 221, 117-130.

Wortel, R., W. Spakman, 2000, "Subduction and slab detachment in the Mediterranean-Carpathian region". *Science* 290, 1910–1917.

Wright TJ; Elliott JR; Wang H; Ryder I., 2013, "Earthquake cycle deformation and the Moho: Implications for the rheology of continental lithosphere". *Tectonophysics*, 609, pp.504-523. doi: 10.1016/j.tecto.2013.07.029.

Yamasaki T; Wright TJ; Houseman GA (2014), "Weak ductile shear zone beneath a major strike-slip fault: inferences from earthquake cycle model constrained by geodetic observations of the western North Anatolian Fault Zone". *Journal of Geophysical Research: Solid Earth*, 119, pp.3678-3699. doi: 10.1002/2013JB010347.

Yılmaz, Ö., 1987, "Investigation in Geophysics: Seismic Data Processing". *Society of Exploration Geophysicists.*

Yiğitbaş, E., Kerrich, R., Yilmaz, Y., Elmas, A. & Xie, Q.L., 2004, "Characteristics and geochemistry of Precambrian ophiolites and related volcanics from the İstanbul-Zonguldak Unit, Northwestern Anatolia, Turkey: following the missing chain of the Precambrian South European Suture zone to the east". *Precambrian Research,* 132, 179206.

Yolsal-Çevikbilen, S., Biryol, C.B., Beck, S., Zandt, G., Taymaz, T., Adiyaman, H.E., Özacar, H.E., 201, "3-D crustal structure along the North Anatolian Fault Zone in north-central Anatolia revealed by local earthquake tomography". *Geophys. J. Int.* 188, 819–849.

Yuan, X., Kind, R., Li, X., and Wang, R., 2006, "The S receiver functions; synthetics and data example". *Geophys. J. Int.*, 165, 555–564, doi:10.1111/j.1365 246X.2006.02885.x, 2006.

Zandt, G., and C.J. Ammon, 1995, "Continental crust composition constrained by measurements of crustal Poisson's ratio", Nature, 374, 152-154.

Zhu, L., 1993, "Estimation of crustal thickness and Vp/Vs ratio beneath the Tibetan Plateau from teleseismic converted waves (abstract.)", Eos Trans. AGU, 74(16), Spring Meet. Suppl., 202.

Zhu, L. & Kanamori, H. 2000, "Moho depth variation in southern California from teleseismic receiver functions". *Journal of Geophysical Research,* 105, 2969 – 2980.

Zhu, L., B.J. Mitchell, N. Akyol, I. Cemen, and K. Kekovali, 2006, "Crustal thickness variations in the Aegean region and implications for the extension of continental crust", J. Geophys. Res., 111, B01301, doi: 10.1029/2005JB003770.

Zor E., Sandvol E., Gürbüz C., Türkelli N., Seber D., Barazangi M., 2003, "The crustal structure of the east Anatolian plateau (Turkey) from receiver functions". *Geophys. Res. Lett.*, 30 (24), 8044, doi:10.1029/2003GL018192.